NUCLEAR STRUCTURE OF QUASARS
AT 329 MEGAHERTZ

Thesis by

Richard Stanley Simon

In Partial Fulfillment of the Requirements
for the Degree of
Doctor of Philosophy

California Institute of Technology
Pasadena, California

1983

(Submitted November 4, 1982)

To Trinka,

Jennifer, Desiree, and David

Acknowledgements

This thesis would have been literally impossible for me to do had it not been for the assistance and help given me by many people. It was Tony Readhead, my thesis advisor, who first introduced me to low-frequency VLBI, and made many useful suggestions to me regarding my work. I shall always be grateful for his advice, assistance, and encouragement.

Marshall Cohen guided my first efforts in VLBI. His patient explanations and lessons in VLBI data reduction first sparked my interest in the subject, and gave me the knowledge I needed to begin to understand what VLBI was capable of doing.

In the progress of my studies it was necessary for a considerable amount of equipment to be built. Alan Moffet generously built four of the receivers I eventually used, and guided my efforts in the constructon and testing of the feeds used at three stations. Without his time and effort this thesis could not have been done. A number of other people gave me indispensable assistance in this construction program, including John Harrimann, Chuck Spencer, and the staff at OVRO.

Harry Hardebeck gave me considerable assistance with all phases of the observations for this thesis; it was his efforts which insured the success of the observations at OVRO. Bob Mutel at Iowa deserves a special thanks from me: he volunteered to have NLRO participate in the main observations of this thesis, and built all of the necessary equipment. I am in debt to both "Sir" Steve Unwin and Tim Pearson for their aid in my efforts at data reduction and understanding. Peter Wilkinson at Jodrell Bank, besides acting as a willing collaborator in much of this work, allowed me to include unpublished maps of his in this thesis, for which I am grateful.

Many other people have helped me in numerous ways. They include George Dvorak, Martin Ewing, Colin Masson, Jay Johovich, Craig Walker, Helen Knudsen, and the many people associated with the operations of the US VLB Network. My apologies, and thanks, to those whom I have neglected to name for their help.

Finally, it has been a great pleasure to work in the bowels of the Henry M. Robinson Laboratory for Astrophysics in association with the many students lurking there. The lower levels of Robinson have a certain aura which I doubt is reproduced anywhere else. I have greatly enjoyed interacting with my fellow students, including but certainly not limited to Don Schneider, Jeff Pier, Roger Linfield, Keith Horne, Abi Saha, Graham Berriman, John Hoessel, Alex Filippenko, and Howard Yee. Being a graduate student in Astronomy at Caltech has been a unique experience in my life, to say the least, and I am glad I was able to do it in the company of so many "interesting" people.

Summary

In the four chapters in this thesis are presented studies of compact quasars using Very Long Baseline Interferometry at 329 MHz.

The first chapter presents hybrid maps of two quasars, 3C147 and 3C286, made at 329 MHz from VLBI observations taken in 1975 with a three station interferometer. The observations presented in the first chapter were used to make the first detailed maps of compact radio structure at this frequency. Both objects consist of an unresolved core; an extended, asymmetric jet; and an even larger, completely resolved halo. For 3C147 it is possible to decompose the spectrum into individual component spectra; at 329 MHz the core of 3C147 is found to be strongly self-absorbed. For both sources the spectral index decreases monotonically from core to jet to halo.

The second chapter presents further observations of quasars at 329 MHz. These observations were taken with a seven-station interferometer and were used to produce high dynamic range maps of the quasars 3C48, 3C147, 3C309.1, 3C380, and 3C454.3. These maps, made with the most extensive low-frequency VLBI observations to date, are the first reliable, high dynamic range maps at this frequency, and reveal extremely complex source structure in four of these sources. All five of the objects are seen to have asymmetric structure that can be interpreted in the "core-jet" picture of compact extragalactic radio sources. The jets observed in these objects are not straight, but bent; three of these quasars have bends in their structure greater than 90° on scales of 1 - 10 kpc.

Chapter three deals with the analysis of the two maps of 3C147 presented in chapters 1 and 2. Comparison of those maps reveals that the core of 3C147 is a low-frequency variable radio source which has brightened by a factor of two in six years. In combination with X-ray observations, this is used to demonstrate that bulk relativistic motion is taking place within the core, and leads to the prediction that 3C147 is a member of the class of "superluminal" radio sources. It is also found that the inclination to the line of sight of the underlying bulk relativistic motion is less than 10°.

A self-consistent picture of 3C147 as a low-frequency variable is thus developed which is consistent with the available observations, yet does not require an extreme value of the total energy: the total energy of the core of 3C147 is found to be $\sim 10^{54}$ ergs. Together with NRAO 140 there are now two extragalactic low-frequency variable radio sources in which bulk relativistic motion has been demonstrated. Thus it may well be that bulk relativistic motion is responsible for the required time-scales in most, if not all, low-frequency variables.

In chapter four, the observations presented in chapter two of 3C48, 3C147, 3C309.1, 3C380, and 3C454.3 are analyzed using standard synchrotron emission theory in order to discover the physical conditions occurring in these objects. For 3C48, the suggestion in chapter 2 of this source as a "core-jet" source is seen to be reasonable, with fields, energy density, and pressure all decreasing with increasing distance from the supposed core. For 3C48, the suggestion in chapter 2 of this source as a "core-jet" source is seen to be reasonable, with fields, energy density, and pressure all decreasing with increasing distance from the supposed core. The pressure in the jet in 3C48 is extremely large, implying that the jet cannot be confined by external gas pressure, unless the surrounding medium has extreme values of the temperature and density. In the case of 3C147 (which was analyzed extensively in chapter 3), the halfwidth of the observed jet implies that collimation of the jet is occurring; the jet in 3C147 is definitely not a "free" jet. For 3C309.1, the 329 MHz observations give an upper limit to the turnover frequency for synchrotron self-absorption significantly lower than that available up to now; this limit, in combination with *Einstein* X-ray observations of 3C309.1, implies that bulk relativistic motion is occurring within the core of 3C309.1. Thus, the core of 3C309.1 may be very similar to the core of 3C147, and is a candidate for being both a superluminal source and a low-frequency variable. For 3C380 and 3C454.3, the limited spectral information available allows broad limits to be put on their properties.

Table of Contents

Appendices

Introduction

This thesis presents studies of quasars using observations at 329 MHz, an observing frequency substantially lower than any used until now for the detailed mapping of the cores of quasars. The observational results, presented in chapters 1 and 2, yield maps of quasars on the arcsecond scale with 20 milliarcsecond resolution, an angular scale previously inaccessible. For comparison, the highest resolution available to the VLA is about 80 milliarcseconds (at 90 times the frequency!), while VLBI maps up to now have had little information about structure beyond the ~ 0.2 arcsecond scale. Some of the implications of these observations are presented in chapters 3 and 4. The observations allow conclusions to be drawn about both the inner, most compact cores of these quasars, as well as the larger, kpc-scale structures that are observed.

This thesis may be considered part of the observational effort at Caltech to understand the compact cores of radio-loud quasars. The primary focus in the VLBI group here at Caltech has been the use of VLBI to produce reliable high-resolution maps of the cores of compact objects, in order to derive physical limits on the processes and conditions occurring in compact extra-galactic radio sources. One continuing program has been the monitoring of "superluminal" radio sources, objects whose radio structure changes with an apparent speed greater than c. My contributions to these studies of the superluminal objects are included in several papers (Cohen *et al.*, 1979; Cohen *et al.*, 1981; Cohen *et al.*, 1983; Pearson *et al.*, 1981a; Pearson *et al.*, 1981b; Unwin *et al.*, 1983a; Unwin *et al.*, 1983b; Walker *et al.*, 1982).

In addition to the above work, I have made contributions to the Caltech VLBI data reduction software. Two of these programs are described in appendices to this thesis.

The chapters of this thesis are intended to be submitted for publication to journals; as a result there is some slight repetition between them, particularly in the reference lists. Chapter 1 has already appeared in print (Simon *et al.*, 1980); chapter 3 has been submitted to *Nature*.

References

1. "VLBI Maps of 3C 273 and 3C 345 at 2.3 GHz". Cohen, M.H., Unwin, S.C., Lind, K.R., Moffet, A.T., Simon, R.S., Wilkinson, P.N., Booth, R.S., Nicolson, G.D., Niell, A.E., and Young, L.E. 1983 (in preparation).

2. "Superluminal Variations in 3C120, 3C273, and 3C345". Cohen, M.H., Pearson, T.J., Readhead, A.C.S., Seielstad, G.A., Simon, R.S. and Walker, R.C. 1979, Ap.J. 231, 293.

3. "Milliarcsecond Structure of 3C345". Cohen M.H., Unwin, S.C., Simon, R.S., Seielstad, G.A., Pearson, T.J., Linfield, R.P., and Walker, R.C. 1981, Ap.J. 247, 774.

4. "Superluminal Expansion of 3C273". Pearson, T.J., Unwin, S.C., Cohen, M.H., Linfield, R.P., Readhead, A.C.S., Seielstad, G.A., Simon, R.S., and Walker, R.C. 1981a, in Extragalactic Radio Sources, ed. D.S. Heeschen and C.M. Wade (Proceedings of I.A.U. Symposium #97, 3-7 August 1981).

5. "Superluminal Expansion of Quasar 3C273". Pearson, T.J., Unwin, S.C., Cohen, M.H., Linfield, R.P., Readhead, A.C.S., Seielstad, G.A., Simon, R.S., and Walker, R.C. 1981b, Nature 290, 365.

6. "Very Long Baseline Interferometry Observations of 3C147 and 3C286 at 329 Megahertz". Simon, R.S., Readhead, A.C.S., Moffet, A.T., Wilkinson, P.N., and Anderson, B. 1980, Ap.J., 236, 707.

7. "Superluminal Motion in the Quasar 3C345". Unwin, S.C., Cohen, M.H., Pearson, T.J., Seielstad, G.A., Simon, R.S., Linfield, R.P., and Walker, R.C. 1983a, Ap.J. (submitted).

8. "Curvature in the Jet of 3C345". Unwin, S.C., Cohen, M.H., Pearson, T.J., Seielstad, G.A., Simon, R.S., Linfield, R.P., and Walker, R.C. 1983b, (in preparation).

9. "Rapid Structural Variations in 3C120". Walker, R.C., Seielstad, G.A., Simon, R.S., Unwin, S.C., Cohen, M.H., Pearson, T.J., and Linfield, R.P. 1982, Ap.J., 257, 56.

CHAPTER 1

Very Long Baseline Interferometry Observations

of 3C 147 and 3C 286 at 329 Megahertz

Reprinted from: The Astrophysical Journal, 236, p. 707 (1980).

Authors: R.S. Simon, A.C.S. Readhead, A.T. Moffet,
P.N. Wilkinson, and B. Anderson

THE ASTROPHYSICAL JOURNAL, 236:707-713, 1980 March 15

VERY LONG BASELINE INTERFEROMETRY OBSERVATIONS OF 3C 147 AND 3C 286 AT 329 MEGAHERTZ

R. S. SIMON, A. C. S. READHEAD, AND A. T. MOFFET
Owens Valley Radio Observatory, California Institute of Technology
AND
P. N. WILKINSON AND B. ANDERSON
Nuffield Radio Astronomy Observatory, University of Manchester
Received 1979 August 24; accepted 1979 October 1

ABSTRACT

We present hybrid maps of two quasars, 3C 147 and 3C 286, made at 329 MHz from VLBI observations. Both objects consist of an unresolved core; an extended, asymmetric jet; and an even larger, completely resolved, halo. For 3C 147 it is possible to decompose the spectrum into individual component spectra; at 329 MHz the core of 3C 147 is found to be strongly self-absorbed. For both sources, the spectral index decreases monotonically from core to jet to halo.

Subject headings: interferometry — quasars — radio sources: general — radio sources: spectra

I. INTRODUCTION

The observations described in this paper form part of a systematic program whose object is studying a representative sample of compact (< 1″) extragalactic radio sources over a wide range of frequencies. A number of objects have been observed at 609 MHz (Wilkinson *et al.* 1977; Wilkinson *et al.* 1979), at 1671 MHz (Readhead and Wilkinson 1980; Pearson, Readhead, and Wilkinson 1980), and at 5011 MHz and 10,651 MHz (Readhead *et al.* 1979). We present here observations at 329 MHz of 3C 147 ($z = 0.545$) and 3C 286 ($z = 0.846$). This is the lowest frequency at which extensive VLBI observations have been made, and these are the first detailed determinations of source structure of compact objects below 600 MHz. These two objects have complex structures; and low-frequency, high-resolution observations are needed to determine the spectral indices of different components within them. The hybrid mapping procedure (Readhead and Wilkinson 1978) has been used, and although the network consisted of only three telescopes we are confident that the maps presented here are substantially correct.

II. OBSERVATIONS

The observations were made in 1975 March, using left-circular polarization at 329 MHz. The details of the stations and antenna characteristics are given in Table 1. The data were recorded with standard NRAO MKII terminals with a bandwidth of 2 MHz (Clark 1973). The videotapes for 3C 286 were correlated on the NRAO processor, and those for 3C 147 on the CIT/JPL processor. Neither processor had three-station capability at the time of processing, and thus three passes were required. Owing to the poor quality of videotape which was used at Jodrell Bank, approximately 5 hours of data on 3C 147 could not be used. A notable difference was observed in the coherence of observations made at day and at night. The poorer quality of the daytime observations was attributable to the effect of ionospheric electron density irregularities which caused phase fluctuations on time scales $\gtrsim 10$ s. At OVRO there was considerable man-made interference at nearby frequencies. This was alleviated by a special filter and judicious choice of observing frequency.

III. THE HYBRID MAPS OF 3C 147 AND 3C 286

The hybrid mapping technique has been described in detail by Readhead and Wilkinson (1978). In general, this has been found to work with simple sources observed with four or more telescopes. With only three telescopes the hybrid map is not as reliable and should be interpreted with caution. In the present case the use of the hybrid mapping technique on data limited to only three stations is justified for the following reasons:

1. These objects have been mapped previously at both 609 MHz and 1671 MHz, and these maps show the same features as the present hybrid maps; i.e., there are no *new* components in the 329 MHz maps. Therefore, we believe that the 329 MHz maps are substantially correct.
2. In both cases the solutions converged rapidly to a map which gave an excellent fit to the amplitudes and closure phases. The maps changed very little in subsequent iterations.
3. For both sources substantially better fits were obtained by hybrid mapping than by model fitting.

In the case of 3C 147, we first tried to fit the data to a model consisting of a set of elliptical Gaussian functions with no constraints except the amplitude data. We found two models for which the fits to the amplitude data were good, but the closure phase data

TABLE 1

INTERFEROMETER ELEMENTS

Location	Diameter (m)	System Noise (K)	Sensitivity (K Jy^{-1})
Jodrell Bank Observatory...	76	188	0.84
NRAO Green Bank.........	43	330	0.20
Owens Valley Radio Observatory.......	40	200	0.176

did not fit at all, indicating that the models were completely wrong. We therefore decided to use our knowledge of the source structure from other observations (Wilkinson *et al.* 1977; Readhead and Wilkinson 1980) in order to fit the 327 MHz data. We tested the 13-component model of G. H. Purcell (Wilkinson *et al.* 1977), by plotting the visibility amplitudes we would have observed on the present three baselines. All of the observed maxima and minima were correctly reproduced by this model. However, the amplitudes were different, indicating that there are significant differences in spectral index in some of the components. We then varied the parameters of the model, and rapidly converged on a new nine-component model which gave a moderately good fit to both the amplitude and closure phase data. In our experience the closure phase is a powerful discriminant between different models which fit the amplitude data equally well, and we were therefore confident that the model was substantially correct. In principle we could have continued model fitting until we achieved an excellent fit to the data. However, we have found that the hybrid mapping procedure converges rapidly if one has a fairly good starting model, and we therefore decided to use this procedure. On the first iteration a significant improvement in the fit was obtained. Subsequent iterations did not significantly change either the fit or the structure of the source.

In the case of 3C 286 we obtained a fairly good fit to both the amplitude and closure phase data from an independent starting model, i.e., without using observations at other frequencies. The first iteration of hybrid mapping produced a very good fit, and in subsequent iterations there were no significant variations.

a) *3C 147*

The 329 MHz hybrid map of 3C 147 is shown in Figure 1*a*, and the fits of the delta functions which constitute this map are shown in Figure 1*b*. In Figure 1*a* we also show the hybrid maps of 3C 147 at 609 MHz (Wilkinson *et al.* 1977) and at 1671 MHz (Readhead and Wilkinson 1980), convolved with the 329 MHz beam. It is clear that the gross structure of the source is the same at all three frequencies: it consists of a bright core, A, and a long, narrow, asymmetric jet containing two knots (B and C). We stress that the details of the 329 MHz map are not as reliable as those of the 609 MHz and 1671 MHz maps. In particular, the exact shapes of knots B and C are not well determined. However, the overall shape, the positions, and the relative strengths of the features must be substantially correct in order to give the good fit of Figure 1*b*.

The most striking difference among the maps shown in Figure 1*a* is the relative strength of the core (A)

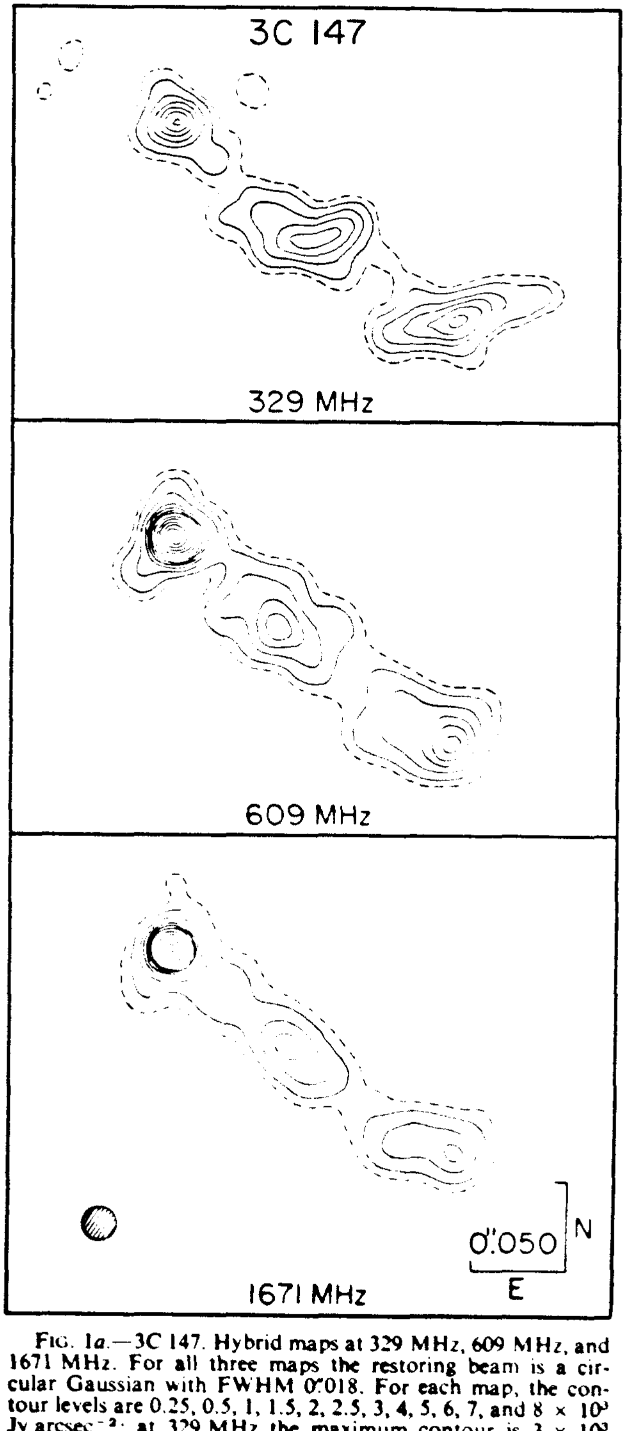

FIG. 1*a*.—3C 147. Hybrid maps at 329 MHz, 609 MHz, and 1671 MHz. For all three maps the restoring beam is a circular Gaussian with FWHM $0\farcs018$. For each map, the contour levels are 0.25, 0.5, 1, 1.5, 2, 2.5, 3, 4, 5, 6, 7, and 8×10^3 Jy arcsec^{-2}; at 329 MHz the maximum contour is 3×10^3 Jy arcsec^{-2}, and at 1671 MHz the maximum contour is 7×10^3 Jy arcsec^{-2}.

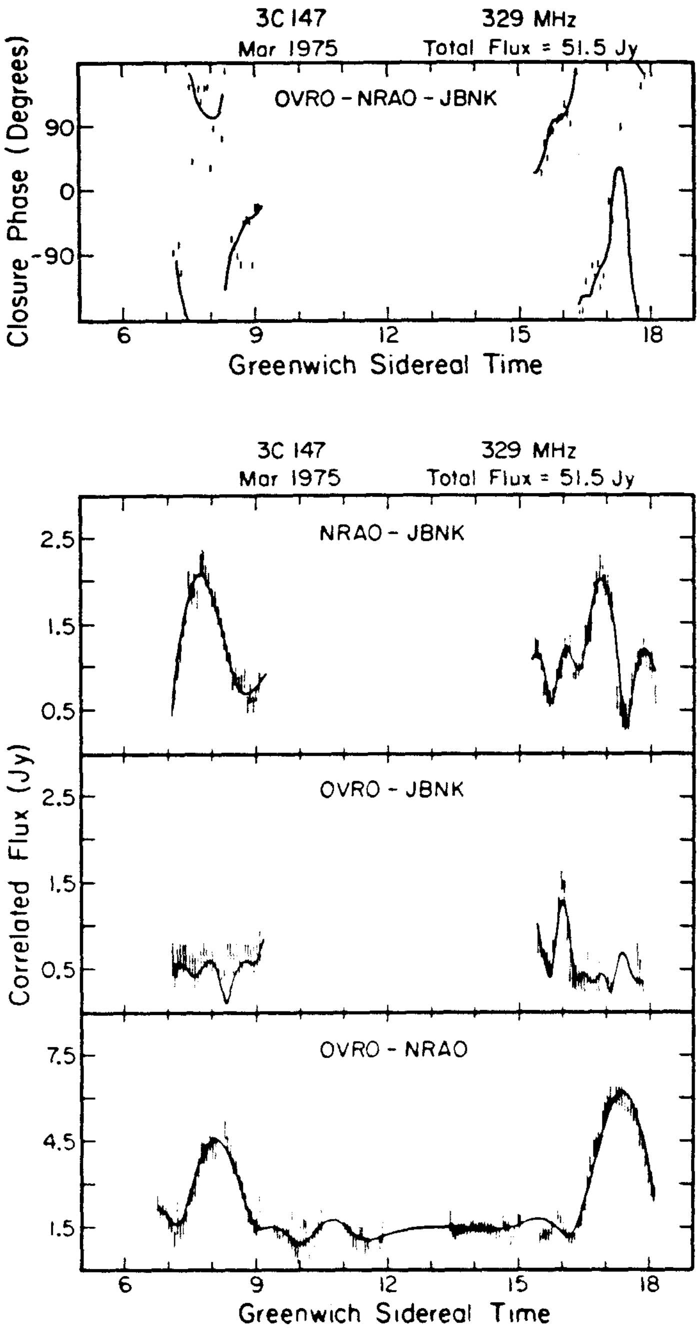

FIG. 1*b*.—3C 147. Fringe amplitude and closure phase data used to produce the 329 MHz map. The solid curves are predicted from the array of point sources which are the basis for the 329 MHz map in Fig. 1*a*.

at different frequencies. At 609 MHz and at 1671 MHz the brightness temperature of the core is much greater than that of the knots (B and C), whereas at 329 MHz they are comparable. Thus the core has a flatter spectrum than the extended features in the jet. A similar effect is found in 3C 286 (see below), and the same behavior has also been seen in 3C 120, 3C 273, and 3C 345 (Readhead *et al.* 1979).

3C 147 also has a halo component of angular size ~0".5 as measured by interplanetary scintillation at 81.5 MHz (Readhead and Hewish 1974), which must be the same component seen by Donaldson and Smith (1971). This component is completely resolved on all baselines at all three frequencies. In Table 2 we show the lower limit which can be placed on the size of the halo from the observations at 329 MHz. Observations of 3C 147 with the Cambridge 5 km telescope (Ryle, private communication), and on the VLA (Readhead

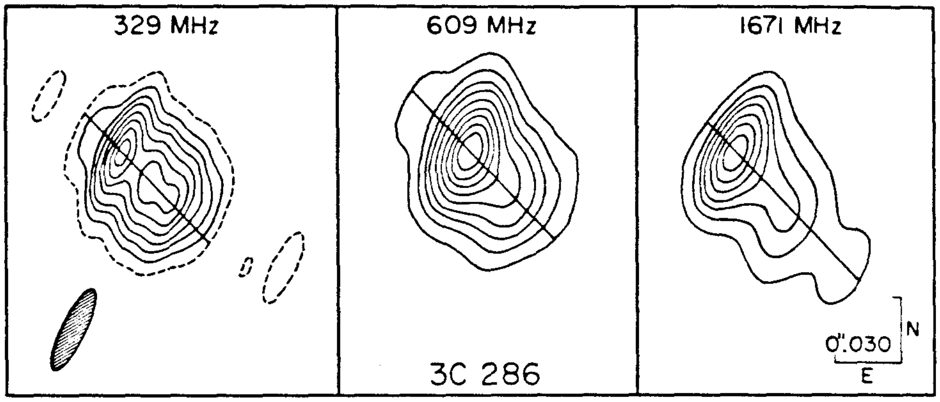

FIG. 2*a*.—3C 286. Hybrid maps at 329 MHz, 609 MHz, and 1671 MHz. For all three maps, the restoring beam is an elliptical Gaussian with FWHM 0".0125 × 0".0425, P.A. = −26°. For each map, the contours are 0.75, 1.5, 2.25, 3, 4, 5, 6, 7, and 8 × 10^3 Jy arcsec^{-2}; at 329 MHz the maximum contour is 7 × 10^3 Jy arcsec^{-2}, and at 1671 MHz the maximum contour is 6 × 10^3 Jy arcsec^{-2}. On each map the straight line has P.A. = 47°.

et al. 1980) place upper limits of $\lesssim 0''.7$ on the size of this component.

b) *3C 286*

In Figure 2*a* we show the present 329 MHz hybrid map together with maps at 609 MHz (Wilkinson *et al.* 1979) and 1671 MHz (Pearson, Readhead, and Wilkinson 1980), convolved with the 329 MHz beam. The fits of the delta functions to the data are shown in Figure 2*b*. As in 3C 147, we see that the gross structure is the same at all three frequencies. The source is unresolved in P.A. = 133° and extended in P.A. = 47°. At 329 MHz approximately 15% of the source lies in an extended region of low surface brightness, which was completely resolved on our shortest baseline, and therefore has angular size $>0''.1$. Previous observations of this component have been discussed in detail by Wilkinson *et al.* (1979). In Figure 3 we show sections through the maps along P.A. = 47° at the three frequencies. The calibration error in each case is believed to be less than about 5%. It is clear that again the object consists of a flat spectrum core and an asymmetric extended structure having a steeper spectrum.

TABLE 2

LIMITS ON THE SIZE OF THE HALO COMPONENT OF 3C 147

Frequency (MHz)	Angular Size (arcsec)	Method	Reference
81.5......	0.4	IPS	Readhead and Hewish 1974
151.5......	0.3	IPS	Duffett-Smith and Readhead 1976
329.......	>0.10	VLBI	present work
2,695.......	~0.5	LBI	Donaldson and Smith 1971
4,885.......	< 0.6	Synthesis	Readhead *et al.* 1980
15,035.......	< 0.5	Synthesis	Readhead *et al.* 1980
15,035.......	< 0.7	Synthesis	Ryle, private communication

IV. ANALYSIS OF THE SPECTRA OF 3C 147 AND 3C 286

The hybrid maps shown in Figures 1*a* and 2*a* provide an excellent basis for analyzing the contributions of different components to the spectra of 3C 147 and 3C 286.

a) *3C 147*

In Figure 4 we show the total spectrum of 3C 147 (Wilkinson *et al.* 1977), to which we have added the 31 and 86 GHz points of Kellermann and Pauliny-Toth (1971), and the spectra of the three major emitting regions within the source, viz. the "halo," the core (A), and the jet (which includes knots B and C). The points on this plot are derived from the present observations, from VLBI observations at 408, 609, and 1671 MHz (Legg *et al.* 1977; Wilkinson *et al.* 1977; Readhead and Wilkinson 1980), from long-baseline interferometry observations at 2695 MHz (from the re-analysis by Fort 1970 of the data of Donaldson and Smith 1971) and from recent observations on the VLA at 4888 and 15,035 MHz (Readhead *et al.* 1980).

The present observations show clearly that the spectrum of the core turns over below 1 GHz. Likewise the jet and halo show maxima in flux density at successively lower frequencies. Scott and Readhead (1977) have shown that synchrotron self-absorption is probably responsible for the turnover in the halo spectrum, and that the halo is near equipartition. Since the lower surface brightness regions have maxima at lower frequencies, it is reasonable to attribute all three low-frequency cutoffs in Figure 4 to synchrotron self-absorption (Wilkinson *et al.* 1977). For the remainder of this discussion we will assume that this is indeed the case. We now discuss the regions separately.

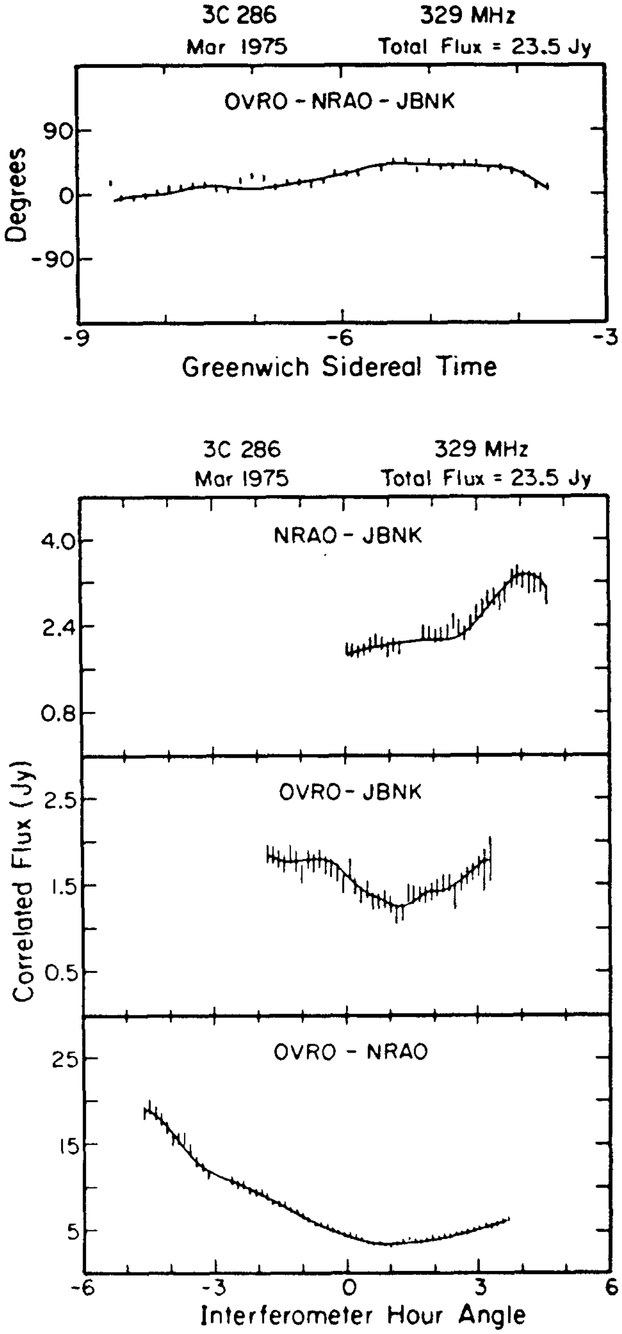

FIG. 2*b*.—3C 286. Fringe amplitude and closure phase data.

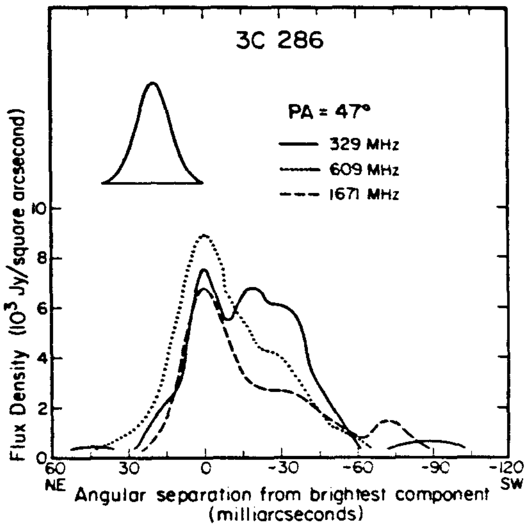

FIG. 3.—Sections of 3C 286 along the lines of Fig. 2*a*. The inset shows the restoring beam along the same position angle.

i) *The Core*

The spectrum of the core is well determined since this component is a distinct compact region which stands out strongly in all of the maps. The peak in the spectrum is at 900 ± 100 MHz, and the high-frequency spectral index is $\alpha = -0.49 \pm 0.1$ (where $S_\nu \propto \nu^\alpha$). Readhead and Wilkinson (1980) have shown that the core itself consists of a double source embedded in a 9 milliarcsec "halo." Thus it is likely that these different regions within the core have different spectral indices. The equipartition angular size of the core (Scott and Readhead 1977) is 9 ± 2 milliarcsec; thus the particle energy must be greater than the magnetic field energy (Wilkinson *et al.* 1977).

ii) *The Jet*

The spectrum presented here is consistent with that of Wilkinson *et al.* (1977). The present data confirm that the peak occurs at 550 ± 150 MHz, and there is some evidence that the spectrum steepens above 5 GHz. This might be attributable to synchrotron losses, but further observations are needed to confirm this effect.

iii) *The Halo*

The spectrum is consistent with that of Wilkinson *et al.* (1977). The spectrum ($\alpha = -1.35 \pm 0.1$) is steeper than that of the core or the jet. This could be due to the complex structures of the core and jet, i.e., it is likely that they contain a number of small features which become self-absorbed between 1 and 10 GHz, and hence make the spectra flatter. Alternatively, the electron injection spectrum could be different in the three regions, or synchrotron losses might account for the steeper spectra in the larger, presumably older, features.

b) *3C 286*

The angular resolution of the present observations enables us to decompose the source into three components: a core, a jetlike extension, and a halo. The spectral indices of these components are not as well determined as for 3C 147 but the same trend is seen, in which the more extended components have steeper spectra. In 3C 286 we find $\alpha_{\mathrm{core}} = -0.29 \pm 0.15$; $\alpha_{\mathrm{jet}} = -0.55 \pm 0.1$, and $\alpha_{\mathrm{halo}} \lesssim -0.8$, for 329 MHz $< \nu <$ 1671 MHz.

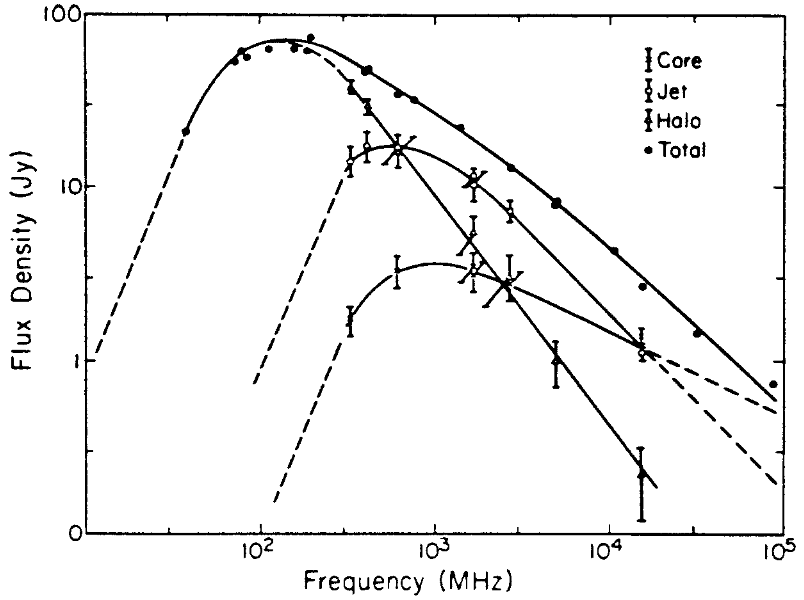

FIG. 4.—Total spectrum and individual component spectra for 3C 147. At 329, 609, and 15,035 MHz core and jet fluxes were determined directly from hybrid mapping and/or model fitting; the halo flux was then determined by subtracting the sum of core and jet fluxes from the total flux. At 408 MHz, the model of Legg *et al.* (1977) (based on 1 baseline of VLBI data) was assumed to give a good representation of the flux of the sum of core plus jet, so that subtraction gave the halo flux, and an interpolated value of the core flux determined the jet flux. At 1671 MHz, there are two independent VLBI observations that have been used. First, core and jet fluxes were directly determined from model fitting by Legg *et al.* (1977) to 1 baseline of VLBI data; the halo was then determined by subtraction. Second, hybrid mapping by Readhead and Wilkinson (1980) gave a reliable core flux; subtraction of the sum of that core flux plus an interpolated halo flux from the total gave another value of the jet flux. The 4885 MHz halo flux is taken from the VLA hybrid map of Readhead, Napier, and Bignell (1980).

V. CONCLUSION

The morphologies of the two sources, 3C 147 and 3C 286, are similar, as are the variations of spectral indices within the sources. Both objects consists of a compact (~0″01), flat spectrum core, an extended asymmetric jet, and a steep spectrum halo (>0″1) which is located within 1″ of the core and jet. Similar morphology has been seen in a number of other sources (Readhead *et al.* 1979; Wilkinson *et al.* 1979), and a brief discussion of the statistics has been given by Pearson, Readhead, and Wilkinson (1980). The possible significance of this morphology has been discussed by Readhead *et al.* (1979) and by Scheuer and Readhead (1979).

The present observations demonstrate the feasibility of hybrid mapping at 329 MHz and enable us to make good estimates of the spectral indices of individual components. They show that it is necessary to make further observations on a wider range of baselines, especially shorter ones, in order to determine the structures of the more extended features in 3C 147 and 3C 286.

We thank G. H. Purcell for his advice and assistance with the observations, Professor Sir Martin Ryle for allowing us to use data prior to publication, and K. I. Kellermann for valuable comments. Two of us (A. C. S. R. and P. N. W.) gratefully acknowledge support of the Weir Research Fellowship for part of the period during which this work was carried out. Research at OVRO is carried out under NSF grant AST 7700247. The NRAO is operated by Associated Universities, Inc., under contract with the NSF.

REFERENCES

Clark, B. G. 1973, *Proc. IEEE*, **61**, 1242.
Donaldson, W., and Smith, H. 1971, *M.N.R.A.S.*, **151**, 253.
Duffett-Smith, P. J., and Readhead, A. C. S. 1976, *M.N.R.A.S.*, **174**, 7.
Fort, D. N. 1970, Ph.D. thesis, University of Manchester.
Kellermann, K. I., and Pauliny-Toth, I. I. K. 1971, *Ap. Letters*, **8**, 153.
Legg, T. H., Fort, D. N., Broten, N. W., Galt, J. A., Anderson, B., and Yen, J. L. 1977, private communication.
Pearson, T. J., Readhead, A. C. S., and Wilkinson, P. N. 1980, *Ap. J.*, **236**, in press.
Readhead, A. C. S., and Hewish, A. 1974, *Mem. R.A.S.*, **78**, 1.
Readhead, A. C. S., Napier, P. F., and Bignell, R. C. 1980, *Ap. J.* (*Letters*), submitted.
Readhead, A. C. S., Pearson, T. J., Cohen, M. H., Ewing, M. S., and Moffet, A. T. 1979, *Ap. J.*, **231**, 299.
Readhead, A. C. S., and Wilkinson, P. N. 1978, *Ap. J.*, **223**, 25.

Readhead, A. C. S., and Wilkinson, P. N. 1980, *Ap. J.*, **235**, 11.
Scheuer, P. A. G., and Readhead, A. C. S. 1979, *Nature*, **277**, 182.
Scott, M. A., and Readhead, A. C. S. 1977, *M.N.R.A.S.*, **180**, 539.
Wilkinson, P. N., Readhead, A. C. S., Anderson, B., and Purcell, G. H. 1979, *Ap. J.*, **232**, 365.
Wilkinson, P. N., Readhead, A. C. S., Purcell, G. H., and Anderson, B. 1977, *Nature*, **269**, 764.

B. ANDERSON and P. N. WILKINSON: Nuffield Radio Astronomy Observatory, Jodrell Bank, Macclesfield, Cheshire SK11 9DL, England

A. T. MOFFET, A. C. S. READHEAD, and R. S. SIMON: Owens Valley Radio Observatory, California Institute of Technology, Pasadena, CA 91125

CHAPTER 2

High Resolution Maps of Five Quasars

at 329 MHz

Summary

Five quasars (3C48, 3C147, 3C309.1, 3C380, and 3C454.3) have been mapped with high resolution using Very Long Baseline Interferometry at a frequency of 329 MHz. These maps, made with the most extensive low-frequency VLBI observations to date, are the first reliable, high dynamic range maps at this frequency, and reveal extremely complex source structure in four of these sources. All five of the objects are seen to have asymmetric structure that can be interpreted in the "core-jet" picture of compact extragalactic radio sources. The jets observed in these objects are not straight, but bent; three of these quasars have bends in their structure greater than 90^o on scales of 1 - 10 kpc.

Subject Headings: interferometry - quasars - radio sources: general

Introduction

In any effort to gain further insight into the physical phenomena occurring in compact, radio-loud quasars, observations are needed over a wide range of wavelengths and resolutions. Up to now, little information has been available on the structural characteristics of quasars in the angular range of 0.02 to 0.2 arcseconds. This range of angular scale falls between that accessible to the largest connected-link radio interferometers and that accessible to Very Long Baseline Interferometry (VLBI) at centimeter wavelengths. In an effort to bridge this gap, we have undertaken extensive VLBI observations at a frequency of 329 MHz, which corresponds to a wavelength almost twice as long as any used for previous VLBI maps.

A number of interesting phenomena in extra-galactic radio sources can be observed easily only at meter wavelengths. Chief among these is the phenomenon of low-frequency variability; as will be seen in chapter 3, long-wavelength observations can play an important role in constraining the kinematics and radiation mechanisms occurring in a low-frequency variable source. A second phenomenon that typically occurs in the meter-wavelength range is the turnover of the radio spectrum for compact radio sources. Observations at 329 MHz, in combination with observations at higher wavelengths, are essential to differentiate between the contribution to the radio spectrum from the most compact cores of the radio sources and from the more extended arcsecond structure.

In this chapter we describe the observations and data analysis, and present the observational results and maps, from a VLBI experiment at 329 MHz. Detailed interpretation will be mostly reserved for chapters 3 and 4 of this thesis.

There are four major sections in this chapter. In the first we describe how the the quasars observed were selected. In section II we discuss the observations and calibration in detail, since this is the first time that a large number of stations have participated in a VLBI experiment at 329 MHz in which accurate calibration was attempted. We also briefly discuss the effects of the ionosphere on these observations. Contained in the next section is an explanation of the mapping technique used, and a detailed description of the map of each object observed. Finally, in section IV we compare the maps of the five sources and attempt to draw some conclusions about the structure seen in these compact quasars at this observing frequency.

I. Source Selection

In the present study, we have undertaken VLBI observations of five quasars (see table I) at 329 MHz, as a start toward a representative sample of compact quasars. The selection of these sources was based on a number of factors, including practical observational constraints; therefore, while these quasars may be representive of compact quasars, they do not form a complete sample. All of these quasars satisfy the following selection criteria:

(1) Known compact structure. In the past, several low-frequency surveys have been conducted using either VLBI or interplanetary scintillation to measure approximate angular diameters of many sources, to find those which have substantial compact structure (Broderick and Condon, 1975; Broten *et al.*, 1969; Clark *et al.*, 1975; Cohen *et al.*, 1967a; Galt, *et al.*, 1977; Harris and Hardebeck, 1969; Readhead and Hewish, 1974). As a result, it is possible to select a number of compact radio sources known to have milliarcsecond (mas) structure. In addition, a number sources had been mapped with VLBI at 609 MHz (Wilkinson *et al.*, 1977; Wilkinson *et al.*, 1979), indicating which sources have structure on an angular scale appropriate for 329 MHz observations. Thus, the source list we used may be biased towards sources with complex structure.

(2) Overall radio spectrum turns over in the ~ 0.1 to ~ 1.0 GHz range. This is a further constraint on the angular size, assuming a low-frequency cutoff due to synchrotron self-absorbtion (Scott and Readhead, 1977).

(3) Declination greater than 10°. This is primarily a practical consideration, based on the limitations of interferometric mapping; the beam shape degrades rapidly at low declinations.

(4) Galactic latitude greater than 10°. Below this latitude, interstellar scattering may significantly blur source structure.

(5) High flux density. Each of these sources is included in the complete sample of Jenkins _et al._, (1977) of 166 extragalactic 3CR radio sources brighter than 10.0 Jy at 178 MHz. Requirements (3), (4), and (5) are the same as the selection criteria used for that complete sample.

(6) Optical identification. Each of these objects has been identified as a quasar, and has a measured redshift (Smith _et al._, 1976, and references therein).

Finally, 3C454.3 was selected on the basis of its being one of the most active known low-frequency variable radio sources (Hunstead, 1972; Condon _et al._, 1979; Fanti, _et al._, 1981; Fisher and Erickson, 1980; Spangler and Cotton, 1981), in addition to satisfying the above requirements.

II. The Observations

The observations for this work were taken during a 54-hour VLBI experiment from 1800 UT on 30 January 1981 to 2400 UT on 1 February, 1981. A seven station interferometer (see table II) was used at a center frequency of 329.1 MHz. With the exception of 3C454.3, each source was observed for about 12 hours, in order to maximize the UV sampling for each map; table I lists the equivalent number of baseline-hours observed on each source. Fortunately, there were no major problems at any station lasting more than a few hours, so the observations of each source are very extensive. In Figure 1 are presented diagrams of the sampling for each source in the transform ("UV") plane. It is the fourier transform of this sampling which determines the beam pattern for each source and is also one of the factors which influences the map dynamic range.

The observations were recorded at each telescope on magnetic tape in standard Mark II format (Clark, 1973), with an effective recording bandwidth of 1.8 MHz. The choice of the exact recording frequency was fortunate, since two of the stations (JBNK and IOWA) experienced potentially disabling RF interference just outside the passband (coincidently, the interference at JBNK was 0.5 MHz above the passband, while that at IOWA was just below). After the experiment, the tapes were processed in three passes on the 5-station California Institute of Technology / Jet Propulsion Laboratory VLBI Correlator in Pasadena.

After correlation of the data it was necessary to edit the data, removing spurious and degraded data points from each source. There were several potential causes of such degradation.

First, severe problems were encountered due to loss of coherence in the fringe phases. The maximum usable coherent integration for each source was set by the timescale for phase variations due to electron density fluctuations in the ionosphere and, in the case of 3C454.3, perhaps interplanetary scintillation. Because these observations were taken near the maximum in solar activity in 1981, the ionosphere was in a relatively disturbed state, and coherence times were typically on the order of 30 to 60 seconds. This contrasts with observations made at this frequency in 1975 (Simon _et al._, 1980 (chapter 1 of this thesis)), for which the coherence time was on the order of four minutes. Furthermore, the coherence time was not constant throughout the experiment, but varied strongly with position on the sky and weakly with time of day. For example, in the case of 3C309.1, while the typical coherence time was ~ 30 seconds, near the start of observations on 3C309.1 the coherence time was less than 15 seconds. This rendered the source undetectable at first on most baselines. However, by the end of the tracks on 3C309.1 the coherence time had improved to greater than 30 seconds on all baselines, and was as much as 60 seconds on a few baselines. For the other sources, coherence times seemed to vary by up to a factor of two, with a weak day-night effect: coherence times were slightly longer when it was nighttime at both stations on a baseline. Another effect that was observed was that the coherence time was a weak function of the length of baseline up to about 10^3 km in length, with the shortest baselines having the longest coherence time. This suggests a scale size of hundreds of kilometers for disturbances in the ionosphere that affect VLBI observations at meter wavelengths. This length scale is much longer, however, than the roughly 2 - 10 km scale size observed in the ionosphere by Hewish (1952), and is much more comparable to the scale sizes observed in the interplanetary medium (Readhead, Kemp, and Hewish, 1978). It is possible that the interplanetary medium played a role in determining the coherence times on all the sources.

In the case of 3C454.3, the observed coherence times were qualitatively different from those observed for th other sources, with coherence times as short as as 6 seconds. The observations of this source were taken in three periods spread over the 54 hour experiment, but the extremely short coherence time was not observed to vary as a function of time, and only weakly as a function of baseline. One possibility is that interplanetary scintillation was the dominant cause of the lack of coherence; 3C454.3 was ~ 35 degrees away from the sun at the time of observation. Since the strength of interplanetary scintillation peaks near that solar elongation (Readhead, Kemp, and Hewish, 1978) with timescales of seconds (Cohen <u>et al</u>., 1967b; Milne, 1976), this is a reasonable hypothesis. The only reason observations of this source were successful is that the source is only slightly resolved with little structure, so that the fringe visibility was large on all baselines; the poor sensitivity offered by 6-second integrations was still sufficent to detect 3C454.3 on all baselines.

For the purposes of this work, the exact causes of these effects on coherence times are unimportant; their primary impact is to force adjustments in the coherent integration times. To minimize the effects of coherence losses, we were forced to use relatively short integration times. In Table I is listed the typical coherent integration time used for each source.

With the coherent integration time chosen near the maximum coherence time, occasional data points still suffered significant reduction in fringe amplitude, and possibly a rotation of the fringe phase, due to brief losses of coherence on individual baselines. Since such changes would affect both the observed amplitude and phase in a baseline-dependent way, closure phases and closure amplitudes are also substantially affected. It was therefore necessary to delete any data points which were suspected of suffering from incoherence, in order to preserve the closure relationships (the various techniques for mapping with closure data (Readhead and Wilkinson, 1978; Cornwell and Wilkinson, 1981; Readhead _et al_., 1981) are unable to correct for baseline-dependent errors. Each source had up to a few percent of its data deleted for this reason.

A second problem which occurred during these observations was RF interference. Typically, a burst of interference will affect all data to a particular station for a brief period of time. The resulting increase in system temperature causes a reduction in fringe amplitude, and would reduce the reliability of the final calibration. To the extent possible, anomalously low fringe amplitudes and their associated phases were simply deleted from the data sets prior to calibration.

After editing, the data were incoherently averaged to either three minutes (3C380), four minutes (3C48, 3C147, and 3C309.1), or six minutes (3C454.3), and then calibrated using the procedure of Cohen (1973). Due to large inconsistencies (up to 30%) in the reported antenna temperatures among the stations, and very unstable system temperature measurements, it was not possible to produce a final calibration for the entire experiment from the calibration data for each individual station alone. As a result, the final calibration for each source was not derived until the maps were generated.

The primary errors remaining in the calibration for these observations are baseline dependent effects. These occur for several reasons, listed below in approximate order of importance:

(1) Incomplete removal of data affected by partial coherence. This was probably the dominant source of error in these observations.

(2) Positive bias in the correlated flux density on weak baselines. Noise in the measured fringe amplitudes biases the observed amplitudes positively. While this effect is significant below a signal-to-noise ratio of about 10, it is possible to correct for this empirically down to an SNR of about 3 (see appendix B). After correction, however, there is probably still a residual error of a few percent on the weakest baselines.

(3) Non-identical antenna polarizations at each station, resulting in an effective aperture for each station that is a slight function of baseline.

(4) Varying bandpass shapes recorded at each station.

(5) Baseline dependent errors in the correlator. These are estimated to be small, however, and were probably insignificant. The estimated errors from the correlator are $\lesssim$ 1%, based on repeatability tests on standard tapes (S.C. Unwin, private communication).

With the exception of the baseline NRAO-FDVS, the cumulative baseline-dependent amplitude errors are about 3-4%. Errors (3) and (4) were probably not important for any of these maps except possibly the map of 3C380, since errors from those causes would have had similar effects on all sources throughout the experiment: Since the map of 3C380 has the lowest noise level of the five maps, it sets the upper limit for the effects of those two sources of error. In the case of the baseline NRAO-FDVS, large gain errors occurred for unknown causes, which became apparent only when mapping began. On all five sources, that baseline was the only one for which a satisfactory fit of the map to the data could not be produced. Therefore, except for 3C309.1, all of the data for that baseline were deleted from the data set for each source prior to making the final maps. In the case of 3C309.1, the miscalibration of NRAO-FDVS was apparently not as severe (see the fit of the data to that baseline in figure 4b); deletion of that baseline would not affect the observed structure significantly, if at all.

The final maps produced from these data have a dynamic range which is limited by these errors to about 50:1 or less, depending on exactly which errors occurred for each source. Table III includes an estimate of the dynamic range for each map which is based only on the amplitude of the negative features appearing in the map.

III. The Maps

After initial calibration, each source was mapped using the iterative mapping procedure of Cornwell and Wilkinson (1981) to improve the calibration of the visibility amplitudes and, in effect, derive the phases from the closure phases. This improvement of the amplitude calibration was successful because of the relatively large number of stations (for VLBI) involved in this experiment. The system temperatures and telescope gains listed in table I include the results of this final calibration step.

In order to preserve as much of the original information as possible, so that the final map fit the initial calibration of the data set as closely as possible, the following procedure was used for mapping:

(1) A crude model consisting of two or three gaussian components was guessed at from the data, and then fitted approximately to the data. These rough models predicted the gross features of the observed visibilities (approximate locations of amplitude minima in the UV plane, approximate changes in the closure phases), but were certainly inadequate as representations of the fine details of source structure. In the case of 3C454.3, an initial model consisting of a point source was used, due to the small amount of structure in the visibility data. In the cases of 3C309.1 and 3C380 it was essential to begin mapping with a two-component model which reflected the wide double-structure seen in these sources.

(2) This model was then used to solve for the station-dependent phase errors using the Caltech algorithm AMPHI, which is based on the CORTEL algorithm (Cornwell and Wilkinson, 1981). On subsequent iterations, the most recent map was used for the AMPHI input model, and, in addition to finding a phase solution for each time interval in the data, an option was used to find a single gain-correction factor for each telescope for the entire observing interval. This latter correction was essential to produce the maps, due to the poor agreement among the stations for antenna gain calibration. Note that this gain solution was made relative to the original calibrated data, so that the original calibration was preserved as closely as possible.

(3) The output from AMPHI was then convolved and gridded into the UV plane and fourier-inverted to produce the so-called "dirty" map. This map was then CLEANed using either the Hogbom (1974) clean technique, in the cases of 3C147 and 3C380, or the Clark (1980) array-processor cleaning algorithm, in the cases of 3C48, 3C309.1, and 3C454.3. The delta functions from the output of CLEAN then formed the input model for the next iteration.

The above procedure was repeated until the agreement of the output map to the visibility data ceased to improve. It should be noted that of these five sources, only one (3C454.3, the most compact) was very straightforward to map. The others all have a substantial amount of extended structure, so that even the short baselines showed complicated structure. For example, the outer component of 3C309.1 is more than 50 beam diameters away from the core. In the case of 3C48, an additional step was added to the above procedure to speed convergence towards the final map: after each clean iteration, several gaussian components were added to the output map and the parameters of these gaussians were fitted (in a least-squares sense) to the visibility data. This extra step (see Appendix A) helped compensate for the failure of CLEAN to find low-level extended structure, and significantly improved the fit of the map to the data. For 3C147 and 3C380, adequate maps were produced by starting with the final CLEAN map and then fitting the parameters of two (3C147) or three (3C380) gaussian components plus the CLEAN map to the data.

This extra step greatly improved the fit of the map to the data on the short baselines, and gave an indication of the location of faint extended structure.

In the discussion which follows, we have assumed a Hubble constant of $H_0 = 60$ km s^{-1} Mpc^{-1} and $q_0 = 0.5$ in order to translate angular measurements into distances. For each object, Table III lists the parameters of the clean beam used, the scale at the object in pc/mas, the observed peak brightness, and the approximate dynamic range of the final map. We now discuss the map of each source in order of complexity.

A. 3C454.3

This quasar was the the farthest south of those observed and was observed for only part of the possible time, due to scheduling constraints. As a result, it had the poorest UV-coverage and the largest sidelobes in its dirty beam of any of these sources. In spite of this, a high-quality map (shown in figure 2a, with the fit to the data of the delta functions which compose this map shown in figure 2b) with a dynamic range of ~ 25:1 was produced from these observations. This was possible because of the extreme compactness of the structure in 3C454.3, which is still ~ 30% unresolved even on the longest baselines. The restoring beam used in figure 2a is an elliptical gaussian whose axes have FWHM that are equal to those of the "dirty beam" (the dirty beam is the calculated response of the interferometer to a point source, and depends on the UV-coverage).

The map reveals that 3C454.3, at the resolution we used, is a barely resolved, asymmetric blob with an extension to the northwest. To parameterize this source we fit to the data a rough model consisting of two gaussian components. A model this simple was not entirely satisfactory. It suggested, however, that the brightest component had a flux of about 5.5 Jy and a diameter less than 20 mas, while the second component was about 10 mas away in PA $\sim 60^{\circ} \pm 10^{\circ}$, elongated along PA 45°, and with a flux of ~ 4.5 Jy.

There is weak evidence in the observed visibilities for extended structure (of the sort seen in the other sources). For example, on the baseline NRAO-HSTK there seems to be some slight residual beating in the amplitude data that is not fitted by the map, but there is too little information to determine even an approximate location for such structure. At the time of these observations, we note that 3C454.3 was in the midst of a flux density outburst, and was about 1 - 2 Jy brighter than either 5 months before or 10 months later (Payne _et_ _al_., 1982) at both 318 and 430 MHz. Since the increased emission was most likely occurring only in the core of the object, the increase in brightness could have helped to mask any larger scale structure in this map. As discussed above, the dynamic range on a map is set mainly by the calibration errors in the data, so that increasing the peak brightness also increases the apparent noise level on the map.

B. 3C380

The complete map of this source is presented in figure 3a, and the fit of the delta functions which compose this map to the data is shown in figure 3b. The apparent dynamic range on this map is very high, due to the relatively simple structure in the dominant components of this source and its comparatively high flux density. There is, however, some structure on the shortest baselines that is not well represented by the map, indicating the existence of weak, extended structure.

The basic structure of 3C380 at this frequency is a wide, 0.72 arcsecond double. Each component is partially resolved, but only the bright, southeastern component contains a substantial amount of unresolved structure. The SE component is observed with VLBI at higher frequencies (Phillips and Shaffer, 1983; Readhead and Wilkinson, 1980; Pearson and Readhead, 1981), since Readhead and Wilkinson detect a weak component whose position angle and separation from the bright component is about the same as that seen for the NW component in this map. We therefore identify the SE component as the central core of 3C380. The position angle of the NW component, relative to the SE one, is -50°, the same to within the errors as that seen in the 1671 MHz map of Readhead and Wilkinson.

To show the structure in the core more clearly, in figure 3c is plotted a small area centered on the core, with the same contour levels as in figure 3a. On its northwestern side, the core is elongated in approximately the position angle defined by the northeastern component, and is nearly unresolved in width. Southeast from the peak in the core component there is a slight bend, so that the position angle of elongation changes from ~ 130° to ~ 110° before it fades into the noise. This bend in the core is real. In contrast, the northeastern component is resolved in both dimensions, although the edge towards the core is only slightly so.

There is significant extended structure in 3C380 which is only seen on the shortest baselines in this experiment. In figure 3d is the map of 3C380 convolved with an 80 mas beam in order to show this faint structure; for comparison, in figure 3e is a 5 GHz map (P.N. Wilkinson, private communication) made with the Multi-Element Radio-Linked Interferometer (MERLIN) (Davies et al., 1980) with the same angular resolution. There is clearly a third component of the source to the northwest, and also an additional region of weak emission about 0.45 arcseconds north of the core.

C. 3C309.1

Due to the large range in both angular scale and brightness encountered in this source, the map has been presented in three separate figures. In figure 4a is shown an overall map of the source convolved with the nominal beam consisting of a circular gaussian of 20 mas FWHM; figure 4b shows the fit of the delta functions which make up this map to the data. Associated with the brightest component in figure 4a are short, concentric arcs of positive and negative noise, probably caused by calibration errors in the data and more or less centered on the brightest component. About 0.95 arcseconds to the east, however, is an extended feature which is real, as shown by the strong beating on the short baselines. The beating, which is especially prominent on the baselines HSTK-NRAO and OVRO-HCRK, corresponds exactly to that caused by a double with the separation and relative position angle of the bright core and weak eastern component.

In order to show the relationship of two components more clearly we have convolved them with a circular beam of 80 mas diameter in figure 4c. In figure 4d is shown an enlarged map centered on the brightest component of 3C309.1, in order to show its detailed structure.

The bright, western component of 3C309.1 has an elongated, curved structure whose dominant position angle varies smoothly from -10^{o} at the northern end to about -50^{o} at the southern. There is weak emission on this map about 0.1 arcseconds to the east of this component which, if related to the brightest component, would imply that the dominant postion angle bends sharply through an additional 90 degrees. That this may be the case is shown by figure 4e, a preliminary map of 3C309.1 with 80 mas resolution made with MERLIN at a frequency of 5 GHz. Taken together, these maps imply that 3C309.1 has a jet-like structure which undergoes a smooth, continuous change in position angle of $\sim 130^{o}$. This curvature is also apparent in the 0.03-arcsecond resolution map of 3C309.1 made by Kus et al. (1981) at 1666 MHz.

The faint, eastern component in 3C309.1 is tightly constrained in position relative to the dominant western component, but does not have a well defined surface brightness or angular size, owing to the small number of baselines which detected it. Based on the amplitude of the beating observed on the short baselines, the flux density of the compact structure in the eastern component is about 2 Jy.

D. 3C147:

This was the strongest of the five sources observed, and yielded the map shown in figure 5a. The fit of the delta functions which compose the map are shown in figure 5b. The only serious difficulty encountered in mapping 3C147 was the existence of extended structure that was only weakly detected on the shortest baselines. In spite of that, the dynamic range for the map of 3C147 is ~ 30:1.

The inner structure of 3C147 consists of an unresolved core at the northest end of the source and a jet of ~ 0.2 arcsecond (1.2 kpc) length extending to the southwest. While emission in the jet occurs along its entire length, two knots of emission are prominent. At this frequency the jet is relatively smooth, as compared to its appearance in other, higher-frequency VLBI maps (Readhead and Wilkinson, 1980; Wilkinson _et_ _al_., 1977). A feature seen in this map and not seen in other maps of 3C147 due to either insuffecent sensitivity (Wilkinson _et_ _al_.) or too much resolution (Readhead and Wilkinson) is the bend which occurs near the southwestern end of the jet. The total change in the position angle of the jet before it fades to invisibility is about 100 degrees.

Associated with 3C147 is a substantial amount of emission which is only detected on the shortest baselines. It is impossible to fit the data on the shortest baseline, OVRO-HCRK, without including this emission in the map. In figure 5c is the map of 3C147 convolved with an 80 mas restoring beam to show more clearly the approximate location of the extended emission. There are regions both to the north and to the southwest which show this extended structure, although the exact shape and location of these regions is not well defined. The reality of these large components is confirmed by maps at higher frequencies, both at 15 GHz (Readhead _et al._, 1980) and at 5 GHz (see figure 5d, a preliminary map produced by P.N. Wilkinson with the MERLIN array which has the same resolution and angular scale as figure 5c).

_E. 3C48_:

This source was the most difficult of the 5 sources observed to map, for several reasons. First, HSTK began observing 3C48 late, so that the UV-coverage for this map was somewhat reduced as compared to the other sources (see figure 1). Second, this source is relatively far south, so the resulting beam shape is worse, making it more difficult to map extended structure. Finally, and most important, 3C48 is the most complex of these 5 sources, without a single dominant component at this frequency. It has the most complicated structure ever mapped with VLBI; only 3C84 (Readhead _et al._, 1983) is of comparable complexity. As a result of these factors, the final, full resolution map of 3C48 has a dynamic range of only ~ 10:1.

The map of 3C48 is presented in figure 6a, and the fit of the map to the data is shown in figure 6b. The contour levels have been selected to reflect the reliability of the map, with linear 10% intervals between the contour levels.

There are a number of striking features on the map of 3C48 that deserve some comment. The map reveals that 3C48 has several knots and bends, so that its structure defies simple classification. It is certain, however, that the structure we see in 3C48 is not an artifact of the mapping technique; the complexity of 3C48 is clearly implied by the structure seen in the visibility and closure phase observations.

The source may be divided into four major regions, three of which contain substantial substructure. In figure 6c we have redrawn the contour map and included labels for the various regions. The division of the source in this way is for convenience, and may or may not be physically significant. In the discussion which follows, we have used the redshift of 3C48 ($z = 0.367$) to translate the observed angular scale to physical distances; the conversion used is 1 mas = 5.1pc.

Region 1: This region consists of a bright, compact component and a short, jet-like feature. The compact component is extended only along position angle (PA) -30°, and is unresolved perpendicular to that PA. This southernmost component blends into the short jet-like feature, with a sharp bend of about 75° in the dominant

PA between the compact component and the jet-like feature.

Region 2: This region contains another bright, compact component which is only slightly resolved. Extending from the bright, compact peak are three features, in position angles ~ 140, ~ -35, and ~ -135 degrees. The feature at PA 140 does not maintain a constant position angle, but rather bends through about 30 degrees until it almost joins with a feature in region 1. The extension of the compact peak in PA -135 is the most prominent, and, after a bend, merges into the jet of region 1.

Region 3: This region consists of three or four components partially blended together. The central and southwestern components are each extended in PA ~ -30^{o}, so that they form an odd structure whose components are extended in a direction more or less perpendicular to their separation. The most northerly component is extended also, but along a PA nearly perpendicular to that seen in the other components in region 3. This gives this region an overall backwards-S shape.

Region 4: The moderately weak feature seen in this region is real, based on two arguments. First, it is the brightest feature on the map outside of the main source (regions 1, 2, and 3), with a peak brightness just over 25% of the overall peak. There are no other features with this brightness anywhere else on the map. Second, if the map is convolved with an 80 mas FWHM restoring beam (figure 6d) the feature seen on the map in region 4 is nearly identical with a feature on the 1 cm, 80 mas resolution VLA map (figure 6e; R.A. Perley, private communication). There is insufficent dynamic range in this map to determine reliably the connection of this structure with the main source, although it is apparently connected to region 3.

Outside of the four regions of figure 6a there is some low-level emission which does not show up well in the map owing to the small number of sufficently short baselines in the UV plane. In figure 6d, the map of 3C48 has been convolved with an 80 mas beam, so that the faint, extended, arcsecond-scale structure which seems to exist in this source can be seen. The most probable location of this emission is to the SE of the main source, at a distance of ~ 0.4 arcseconds, as suggested by model fitting, but this is uncertain; there may also be emission ~ 0.3 seconds to the SW of region 1. It is not clear how this extended emission is related to the rest of the source. We note that the map of 3C48 accounts for about 18 Jy, implying that there are about 25 Jy in the source at this wavelength which are unaccounted for by these observations.

A possible interpretation of the first three regions described above is as a single, oscillating jet. In this case the wavelength for such an oscillation is about 70 to 130 mas, or 350 to 650 parsecs in projected length. The overall projected length of this jet is about 0.3 arcseconds, or ~ 1.5 kpc.

IV. Discussion

These five sources have several common features. Most prominent is the strong asymmetry seen in each of these objects. The asymmetry ranges from the slight NW extension in 3C454.3 through the core-jet type of morphology seen in 3C48 and 3C147 to the extremely asymmetric, double-structure seen in 3C309.1 and 3C380.

The asymmetry in the structure of 3C48 is less obvious until the high-frequency map of figure 6e is compared with the map in figure 6d. Since no absolute positions are possible with VLBI maps, due to the loss of absolute phase information, the relative alignment of the two maps must be done on the basis of the observed structure at the two frequencies. Fortunately, there are features in both of these maps which allow an approximate alignment to be made. First, the region to the east of the main source (region 4 in figure 6c) is present on both maps. Second, the position angle connecting the two main "blobs" in the source at this resolution is the same, at about 10°, and the dominant position angles within each of the main blobs are roughly the same in each map, $\sim 0^{\circ}$ PA The primary difference between the two maps is that the southern blob is considerably more elongated in the 22 GHz map than in the 329 MHz map. With the alignment suggested by the crosses in figures 6d and 6e, this difference must be caused by the existence of a component in 3C48 that is not seen at 329 MHz and which has a negative spectral index α ($S \propto f^{-\alpha}$) between 329 MHz and 22.5 GHz. Assuming a detection limit of ~ 0.1 Jy at 329 Mhz, the spectral index of this "missing component" is $\lesssim -0.5$. Note that it is possible that this component has a spectral peak somewhere between the two frequencies, so that the spectrum would be rising even more steeply at 329 MHz.

With the above alignment, the structure of 3C48 becomes somewhat easier to interpret. We identify the "missing component" as the central core of 3C48, on the basis of its rising spectrum. This core is analogous to the cores of other compact objects such as 3C147 (chapter 3, this thesis), 3C273 and 3C345 (Cohen _et al._, 1983; Unwin _et al._, 1983), and 3C84 (Readhead _et al._, 1983) in which the central core has a rising spectrum at low frequencies, while the more extended, jet-like structures have positive spectral indices. The complex structure seen in the 329 MHz maps of 3C48 can then be interpreted as a one-sided jet, much like that seen in 3C147, but with many bends and twists to its structure. Like 3C147, 3C48 must be classified as a "core" object (Readhead _et al._, 1978; Readhead, 1980) in view of its asymmetric, bent jet.

3C309.1 and 3C380 also seem to be in the same class as 3C147 and 3C48. Each also has a compact core with a bent, one-sided jet emerging from that core. There is an intrinsic difference, however, in the bending which occurs in 3C380 and that which occurs in the other three sources. For 3C380, the bending is seen in the inner few tens of parsecs at high frequencies (Pearson and Readhead, 1981); then there is no evidence either of emission or of a change in position angle until the compact, northwestern component is encountered 0.72 arcseconds (~ 5 kpc projected distance) from the core. On the other hand, 3C48, 3C147, and 3C309.1 all show clear evidence for bent, onesided, kiloparsec-scale jets.

In the case of 3C454.3, the dominance of the core at low frequencies may be masking a structure that is similar to that seen in the other sources. Higher frequency VLBI observations indicate that 3C454.3 is elongated along position angle -65° at 2.29 GHz (Cotton _et al_., 1981) and at position angle -56° at 1.67 GHz (Pearson _et al_., 1980). In the observations presented here, the dominant position angle of $\sim -45^{\circ}$ (far from the core, from modelfitting) is the same (within the errors) as the position angle observed by Browne _et al_. (1982) with MERLIN of the extended arcsecond-scale jet. Thus the dominant position angle in this source rotates smoothly through about $+15^{\circ}$ as the scale size increases. This behavior is similar to that discussed for 3C380 above; as a result, 3C454.3 can also be classified as a core object with an asymmetric, bent beam of radio emission.

In three of these quasars, in addition to the apparent core-jet morphology, there is evidence of weak emission on the side of the core opposite to the main beam or jet. This is most obvious in the case of 3C147, where the MERLIN map of P.N. Wilkinson in figure 5d shows weak emission roughly opposite to the jet to the northeast; a puzzling feature in that map, however, is the emission to the southeast of the core. Both these areas of emission were also detected at 329 MHz, confirming their reality. In 3C309.1, the emission opposite to the MERLIN arcsecond jet is in the form of a weak component about 0.9 arcseconds to the west (Cornwell and Wilkinson, 1981; Kus _et al_., 1981). In 3C380, it is the core which shows elongation in a direction nearly opposite to the position angle defined by the strong northwestern component. This elongation is slight, however; observations at a higher frequency (e.g., ~ 0.6 GHz) with improved resolution are needed to confirm this.

Conclusions

Without exception, the five quasars mapped show asymmetric, mostly one-sided structure at 329 MHz. Although there may be weak counter-jets in three of these objects, such counter-jets are not prominent (in terms of surface brightness) at this frequency.

With the exception of 3C454.3, these sources have extremely complex structure. Although their structure may be classified as "core-jet", the jets in these objects are undergoing sharp bends on the 1 - 10 kpc scale; bends greater than 90° are seen in 3C48, 3C147, and 3C309.1. The bending occurring in 3C380 and 3C454.3 is more gradual, but still apparent when higher frequency VLB observations are taken into account.

Acknowledgements

We wish to thank the US VLBI Network and the observers and technical staff of all the Network observatories involved in this work. In particular, we are extremely grateful to R. L. Mutel at North Liberty Radio Observatory who generously built an entire receiving system for these observations. We also wish to thank R.A. Perley for the use of the 3C48 VLA map in advance of publication. This work was supported by the National Science Foundation via grant AST 79-13249 to the Owens Valley Radio Observatory.

TABLE I

Sources observed at 329 MHz

Name	I.A.U. Desig.	z	329 Flux Density	Baseline Hours	Typical Coherence Time
3C48	0134+32	0.3670	43.5 Jy	115	60 sec
3C147	0538+49	0.545	53	204	60
3C309.1	1458+71	0.904	16	215	30
3C380	1828+48	0.691	42	174	60–120
3C454.3	2251+15	0.8600	13.6(var.)	57	$\lesssim 6$

TABLE II

Interferometer Elements

Station Name	Location	Diameter	System Temperature	Sensitivity ^{o}K/Jy
JBNK	Jodrell Bank, Cheshire, UK	76 m	270 K	0.63
HSTK[*]	Haystack, Ma., USA	46	220	0.21
NRAO[**]	Greenbank, W Va., USA	43	125	0.21
IOWA	North Liberty, Iowa, USA	18	160	0.042
FDVS	Fort Davis, Tx., USA	26	340	0.06
OVRO	Big Pine, Ca., USA	40	195	0.018
HCRK	Hat Creek, Ca., USA	26	210	0.06

[*] System temperatures at HSTK were about 360 ^{o}K for the observations on 3C48 and 3C309.1, and part of the observations on 3C454.3.

[**] The National Radio Astronomy Observatory is operated by Associated Universities Inc., under contract to the National Science Foundation.

TABLE III

Parameters for the Maps

Name	Restoring Beam Minor Axis	 Major Axis	 Position Angle	Scale pc/mas	Peak Brightness 10^8 °K	 Jy/beam	Dynamic Range
3C48	18 mas	39 mas	−31o	5.1	151	0.94	~10:1
3C147	18	20	−20	6.1	637	2.03	~30:1
3C309.1	18	-	-	7.0	938	2.70	~50:1
3C380	18	20	−20	6.6	568	1.82	~100:1
3C454.3	16	71	−19	6.9	596	6.02	~25:1

References

Broderick, J.J., and Condon, J.J. 1975, Ap.J., 202, 596.

Broten, N.W., Clarke, R.W., Legg, T.H., Locke, J.L., Galt, J.A., Yen, J.L., and Chisholm, R.M. 1969, M.N.R.A.S., 146, 313.

Browne, I.W.A., Clark, R.R., Moore, P.K., Muxlow, T.W.B., Wilkinson, P.N., Cohen, M.H., and Porcas, R.W. 1982, Nature (submitted).

Clark, B.G. 1980, A. and A., 89, 377.

Clark, B.G. 1973, Proc. I.E.E.E., 61, 1242.

Clark, T.A., Erickson, W.C., Hutton, L.K., Resch, G.M., Vandenberg, N.R., Broderick, J.J., Knowles, S.H., and Youmans, A.B. 1975, A.J., 80, 923.

Cohen, M.H. 1973, Proc. I.E.E.E., 61, 1192.

Cohen, M.H., Gunderman, E.J., and Harris, D.E. 1967a, Ap.J. 150, 767.

Cohen, M.H., Gundermann, E.J., Hardebeck, H.E., and Sharp, L.E. 1967b, Ap.J., 147, 449.

Condon, J.J., Ledden, J.E., O'Dell, S.L., and Dennison, B. 1979, A.J., 84, 1.

Cornwell, T.M., and Wilkinson, P.N. 1981, M.N.R.A.S., 196, 1067.

Cotton, W.D., Geldzahler, B.J., and Shapiro, I.I. 1982, Extragalactic Radio Sources, I.A.U. Symp. No. 97, p. 301 (Ed. Heeschen, D.S. and Wade, C.M., Reidel, Dordrecht).

Davies, J.G., Anderson, B., and Morrison, I. 1980, Nature, 288, 64.

Fisher, J.R., and Erickson, W.C. 1980, Ap.J., 242, 884.

Fanti, C., Fanti, R., Ficarra, A., Mantovani, F., Padrielli, L., and

Weiler, K.W. 1981, A.A. Suppl., 45, 61.

Galt, J.A., Broten, N.W., and Legg, T.H. 1977, M.N.R.A.S., 178, 301.

Harris, D.E., and Hardebeck, E.G. 1969, Ap.J. Suppl., 19, 115.

Hewish, A. 1952, Proc. Roy. Soc., 214, 494.

Hogbom, J.A. 1974, A. and A. Suppl., 15, 417.

Hunstead, R.W. 1972, Ap. Letters, 12, 193.

Jenkins, C.J., Pooley, G.G., and Riley, J.M. 1977, Mem. R.A.S., 84, 61.

Kus, A.J., Wilkinson, P.N., and Booth, R.S. 1981, M.N.R.A.S., 194, 527.

Milne, R.G. 1976, Aust. J. Phys., 29, 201.

Payne, H.E., Altschuler, D.R., Broderick, J.J., Condon, J.J., Dennison, B. and O'Dell, S.L. 1982, Contribution to N.R.A.O. Workshop on "Low-Frequency Variability of Extra Galactic Radio Sources".

Pearson, T.J., Readhead, A.C.S., and Wilkinson, P.N. 1980, Ap.J., 236, 714.

Pearson, T.J., and Readhead, A.C.S. 1981, Ap.J., 248, 61.

Phillips, R.B., and Shaffer, D.B. 1983, Ap.J. (submitted).

Readhead, A.C.S., and Hewish, A., 1974, Mem. R.A.S., 78, 1.

Readhead, A.C.S., Cohen, M.H.C., Pearson, T.J., and Wilkinson, P.N.W. 1978, Nature, 276, 768.

Readhead, A.C.S., Kemp, M.C., and Hewish, A. 1978, M.N.R.A.S., 185, 207.

Readhead, A.C.S., and Wilkinson,P.N. 1978, Ap.J., 223, 25.

Readhead, A.C.S., Napier,P.J., and Bignell, R.C. 1980, Ap.J., 237, L55.

Readhead, A.C.S 1980, Physica Scripta, 21, 662.

Readhead, A.C.S., and Wilkinson,P.N. 1980, Ap.J., 235, 11.

Readhead, A.C.S., Walker, R.C., Pearson, T.J., and Cohen, M.H. 1981, Nature, 285, 137.

Readhead, A.C.S., Hough, D.H., Ewing, M.S., Walker, R.C., and Romney, J.D. 1983, Ap.J. (in press).

Scott, M.A. and Readhead, A.C.S. 1977, M.N.R.A.S., 180, 539.

Simon, R.S., Readhead, A.C.S., Moffet, A.T., Wilkinson, P.N., and Anderson, B. 1980, Ap.J., 236, 707.

Smith, H.E., Spinrad, H., and Smith, Eileen O. 1976, P.A.S.P., 88, 621.

Spangler, Steven R., and Cotton, William D. 1981, A.J., 86, 730.

Unwin, S.C., Cohen, M.H., Pearson, T.J., Seielstad, G.A., Simon, R.S., Linfield, R.P., and Walker, R.C. 1983, Ap.J. (submitted).

Wilkinson, P.N., Readhead, A.C.S., Purcell, G.H., and Anderson, B. 1977, Nature, 269, 764.

Wilkinson, P.N., Readhead, A.C.S., Anderson, B., and Purcell, G.H. 1979, Ap.J., 232, 365.

Figure Captions

1. The sampling in the transform ("UV") plane for each of the sources mapped. The projected baseline is plotted as a dot for each UV-sample; on short baselines the points merge to form continuous lines with the scale plotted.

   (a) UV coverage for 3C48

   (b) UV coverage for 3C147

   (c) UV coverage for 3C309.1

   (d) UV coverage for 3C380

   (e) UV coverage for 3C454.3

2. 3C454.3 figures:

   (a) Map of 3C454.3 at 329 MHz. The clean components which compose this map have been convolved with an elliptical gaussian restoring beam with FWHM dimensions of 0.071 by 0.016 arcseconds, and a position angle of -19^{o}. In this and all other maps, the hatched area plotted in the lower left represents the FWHM shape of the clean beam and the scale of the map is given by the scale plotted in the lower right of the map. The contour levels in this map are -3,3,9,15,...,99% of the peak on the map; in this and all subsequent maps the negative contours are dotted. The peak brightness for the full-resolution map of each of the five sources is listed in table III.

(b) The fit of the delta functions which compose the map of 3C454.3 to the visibility data. In this and all subsequent plots of visibility amplitudes and closure phases, observations are plotted as vertical bars whose length represents the uncertainty in the data, while the predicted amplitudes and closure phases from the maps are drawn as a continuous line.

3. 3C380 figures:

(a) Map of 3C380. The beam used for this map was an elliptical gaussian with FWHM 0.018 x 0.020 arcsecond in position angle -20°. The contour levels on the map are -1,1,2,4,8,16,32, and 64% of the peak brightness (see caption for figure 2a).

(b) Fit of the delta functions which compose the map to the visibility data for 3C380 (see caption for figure 2b).

(c) Map of the core of 3C380. This is the southeastern component in figure 4a enlarged to show detail. The restoring beam and contour levels are the same as those used for figure 4a.

(d) Map of 3C380 convolved with a large beam. The components of the map of 3C380 have been convolved with a circular gaussian of 0.08 arcsecond FWHM to show the faint, extended structure which exists in this source. The contour levels used in this map are -2,2,4,8,16,32,64% of the peak on this map; the peak brightness temperature is 5.38×10^9, which equals 3.06 Jy/beam.

(e) MERLIN map of 3C380 at 5 GHz, and a resolution of 0.08 arcseconds. While the scale in this map is the same as for the map in figure 4e, the contour levels used are -0.3,.3,.6,.9,1.2,1.5,2.0,2.5,...,10% of the peak on the map. This map and the two MERLIN maps for 3C309.1 and 3C147 are reproduced from as-yet unpublished work with the kind permission of P.N. Wilkinson.

4. 3C309.1 figures:

(a) Full resolution map of 3C309.1. The beam used for this map was a circular gaussian with FWHM 0.018 arcseconds. The contour levels on the map are -1,1,3,5,10,20,40,60 and 80% of the peak brightness (see caption for figure

2a).

(b) Fit of the delta functions which compose the map to the visibility data for 3C309.1 (see caption for figure 2b).

(c) Map of 3C309.1 convolved with a large beam. The components of the map of 3C309.1 have been convolved with a circular gaussian of 0.08 arcsecond FWHM so that this map may be compared with the MERLIN map of figure 4e. The contour levels used in this map are -2,2,4,8,16,32,64% of the peak on this map; the peak brightness temperature is 1.07×10^{10} ^{o}K, which equals 6.07 Jy/beam.

(d) Map of the core of 3C309.1. This is the western component in figure 4a enlarged to show detail. The restoring beam used is the same as for figure 4a, but the contour levels are -2,2,4,6,10,15,20,30,40,...,90% of the peak brightness of the source.

(e) MERLIN map of 3C309.1 at 5 GHz, and a resolution of 0.08 arcseconds. While the scale in this map is the same as for the map in figure 4c, the contour levels used are -0.3,.3,.6,1.2,1.8,2.4,...,9.6% of the peak of the map.

5. 3C147 figures:

(a) Map of 3C147. The beam used for this map was an elliptical gaussian with FWHM 0.018 x 0.020 arcsecond in position angle -20°. The contour levels on the map are -3,3,9,15,21,...,99% of the peak brightness on the map (see caption for figure 2a). There is low-level emission outside the window of this map which is shown with a large beam in figure 5c.

(b) Fit of the delta functions which composse the map to the visibility data for 3C147 (see caption for figure 2b).

(c) Map of 3C147 convolved with a large beam. The components of the map of 3C147 have been convolved with a circular gaussian of 0.08 arcsecond FWHM to show the faint, extended structure seen in this source. The contour levels used in this map are -2,2,4,6,10,15,20,30,40,50,70,90% of the peak on this map; the peak corresponds to a brightness temperature of $1.55\text{x}10^{10}$, which equals 8.81 Jy/beam.

(d) MERLIN map of 3C147 at 5 GHz with a resolution of 0.08 arcseconds. While the scale in this map is the same as for the map in figure 5d, the contour levels used are -0.4,.4,1.2,2.0,3.6,5.2,8.0,11,14,17,20,25,30,35,...,75% of the peak on the map.

6. 3C48 figures:

(a) Full resolution map of 3C48. The beam used for this map was an elliptical gaussian of FWHM 0.018 x 0.039 arcseconds with position angle -19°. The contour levels on the map are -5,5,15,25,...,95% of the peak brightness (see caption for figure 2a).

(b) Fit of the delta functions which compose the map to the visibility data for 3C48 (see caption for figure 2b).

(c) Map of the inner area of 3C48 with the regions discussed in the text identified. The dashed lines form the divisions between the areas. The beam and contour levels in this figure are the same as for figure 6a; the scale has been increased for clarity.

(d) Map of 3C48 convolved with a large beam. The components of the map of 3C48 have been convolved with a circular gaussian of 0.08 arcsecond FWHM so that this map may be compared with the VLA map of figure 6e. The countour levels used in this map are -10,10,20,...,90% of the peak on this map; the peak corresponds to a brightness temperature of 4.81×10^{9} K, which equals 2.73 Jy/beam. The small crosses on this map and the map in 6e represent a possible alignment of the two maps (see text).

(e) VLA map of 3C48 at 22.5 GHz, with a resolution of 0.08 arcseconds. While the scale in this map is the same as for the map in figure 6d, the contour levels used are -2.5,2.5,5,10,20,30,50,70,90% of the peak of the map; the peak corresponds to 0.22 Jy/beam. This map has been reproduced prior to publication with the permission of R.A. Perley.

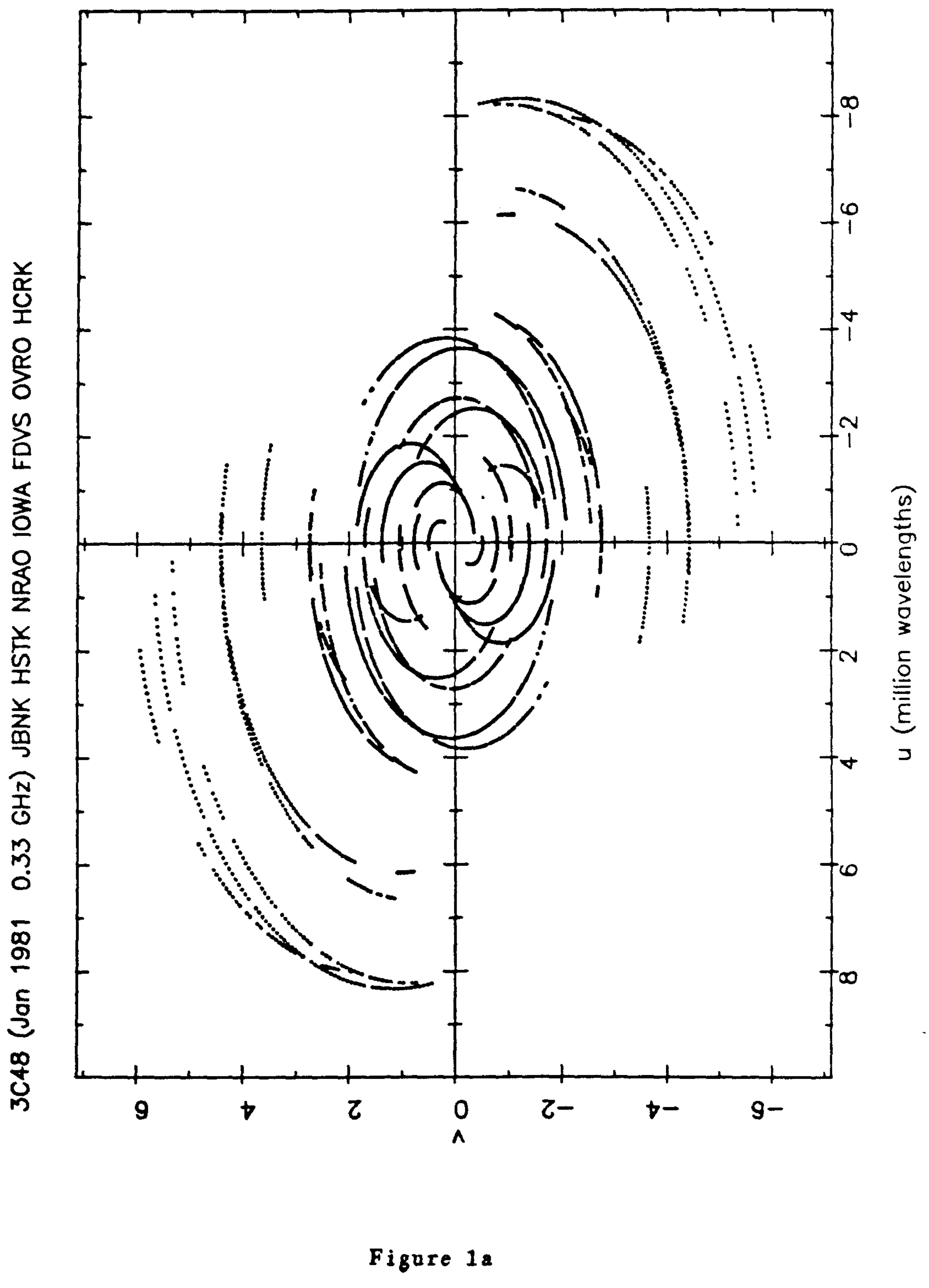
3C48 (Jan 1981 0.33 GHz) JBNK HSTK NRAO IOWA FDVS OVRO HCRK
v
6
4
2
0
−2
−4
−6
u (million wavelengths)
8
6
4
2
0
−2
−4
−6
−8

Figure 1a

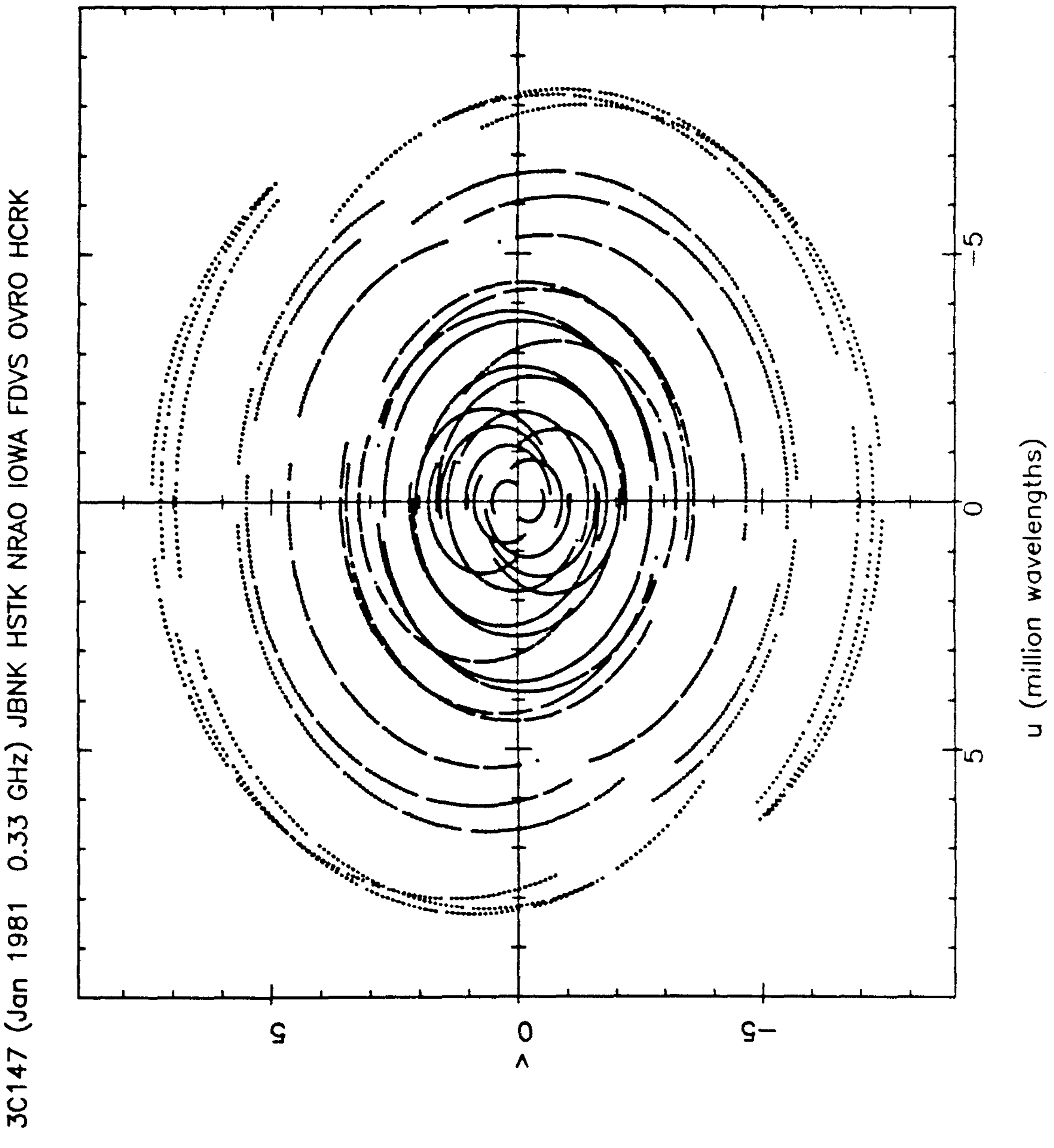
3C147 (Jan 1981 0.33 GHz) JBNK HSTK NRAO IOWA FDVS OVRO HCRK
5
0
-5
v
-5
0
5
u (million wavelengths)

Figure 1b

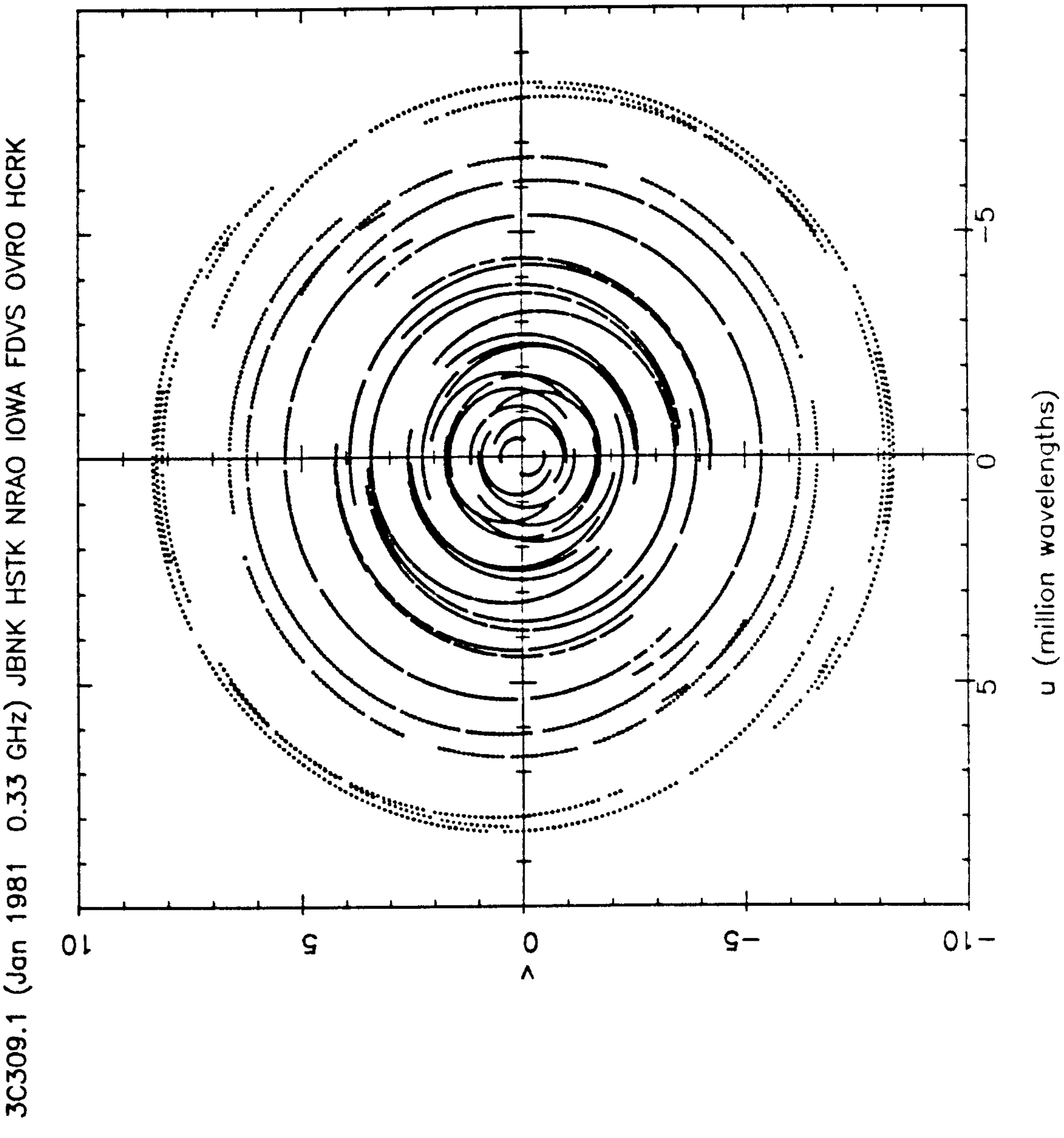
3C309.1 (Jan 1981 0.33 GHz) JBNK HSTK NRAO IOWA FDVS OVRO HCRK
v
10
5
0
−5
−10
u (million wavelengths)
5
0
−5

Figure 1c

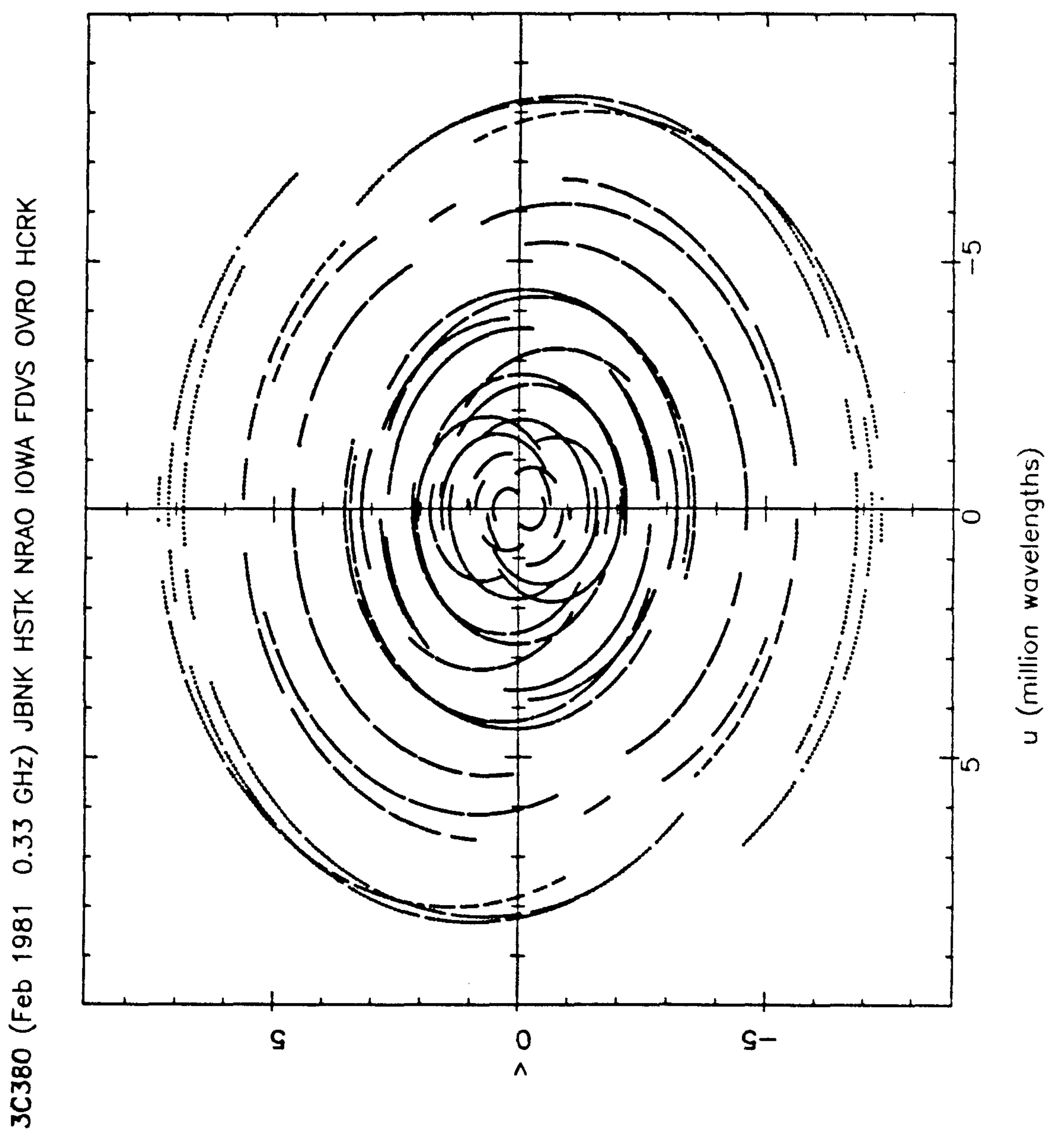
3C380 (Feb 1981 0.33 GHz) JBNK HSTK NRAO IOWA FDVS OVRO HCRK
5
0
-5
v
-5
0
5
u (million wavelengths)

Figure 1d

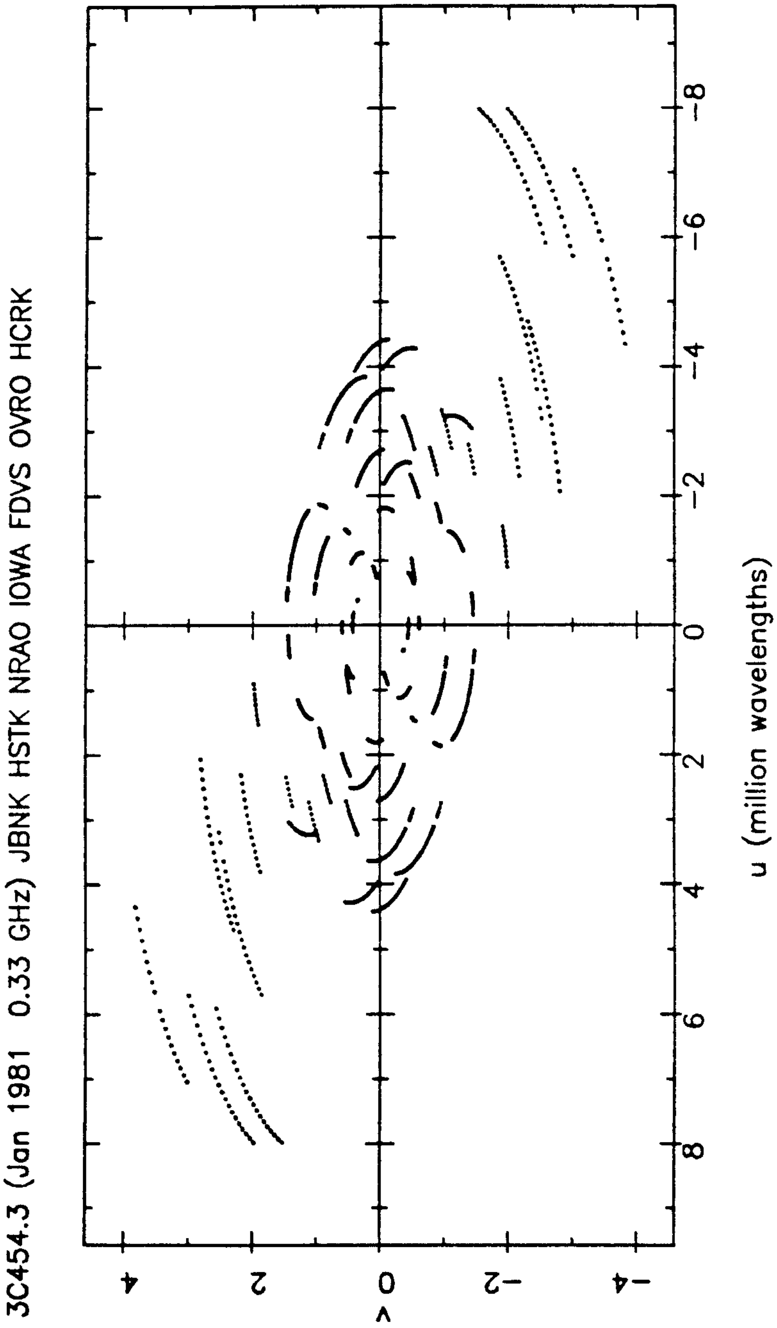
3C454.3 (Jan 1981 0.33 GHz) JBNK HSTK NRAO IOWA FDVS OVRO HCRK
v
4
2
0
-2
-4
u (million wavelengths)
-8
-6
-4
-2
0
2
4
6
8

Figure 1e

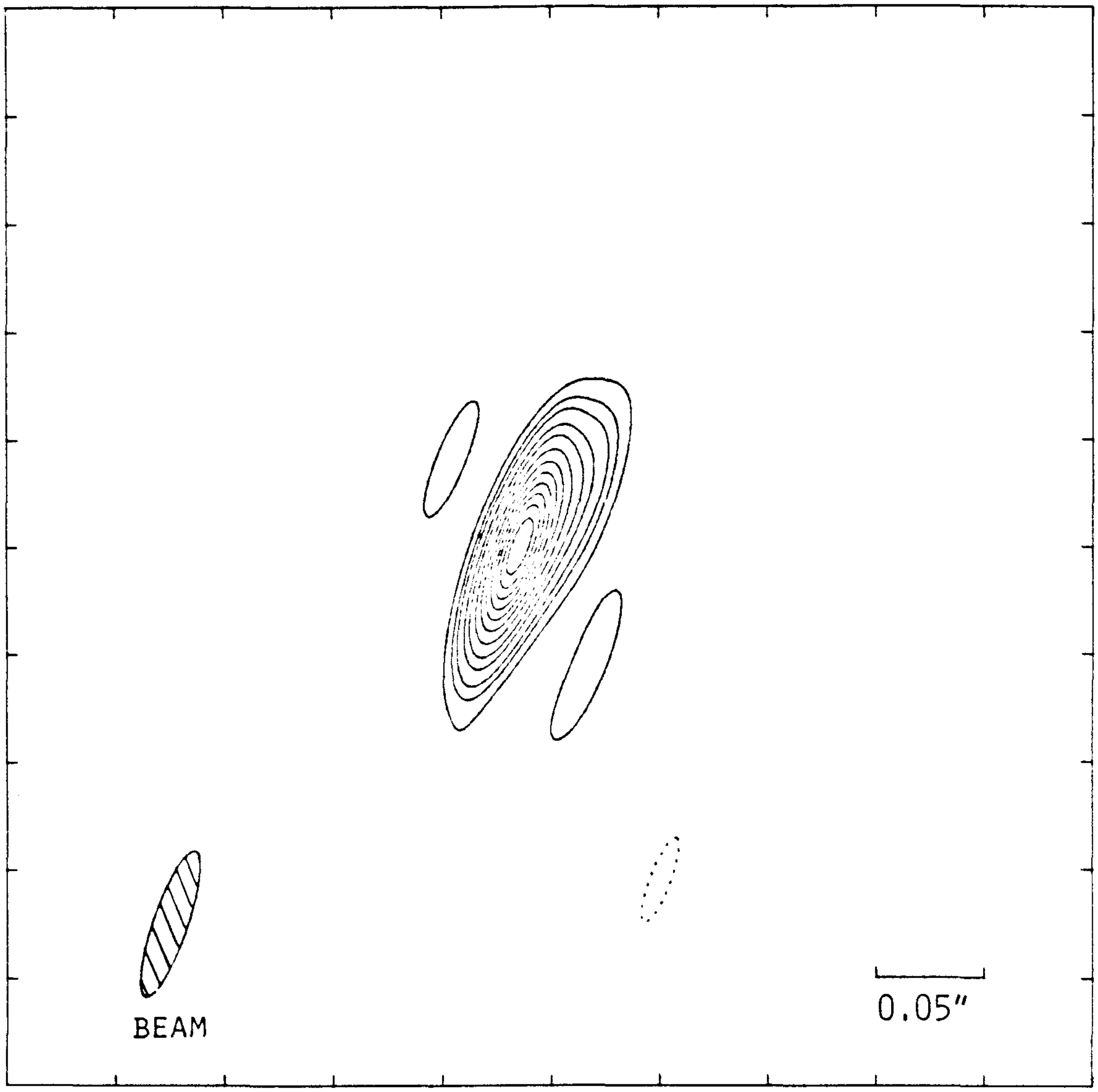

Figure 2a

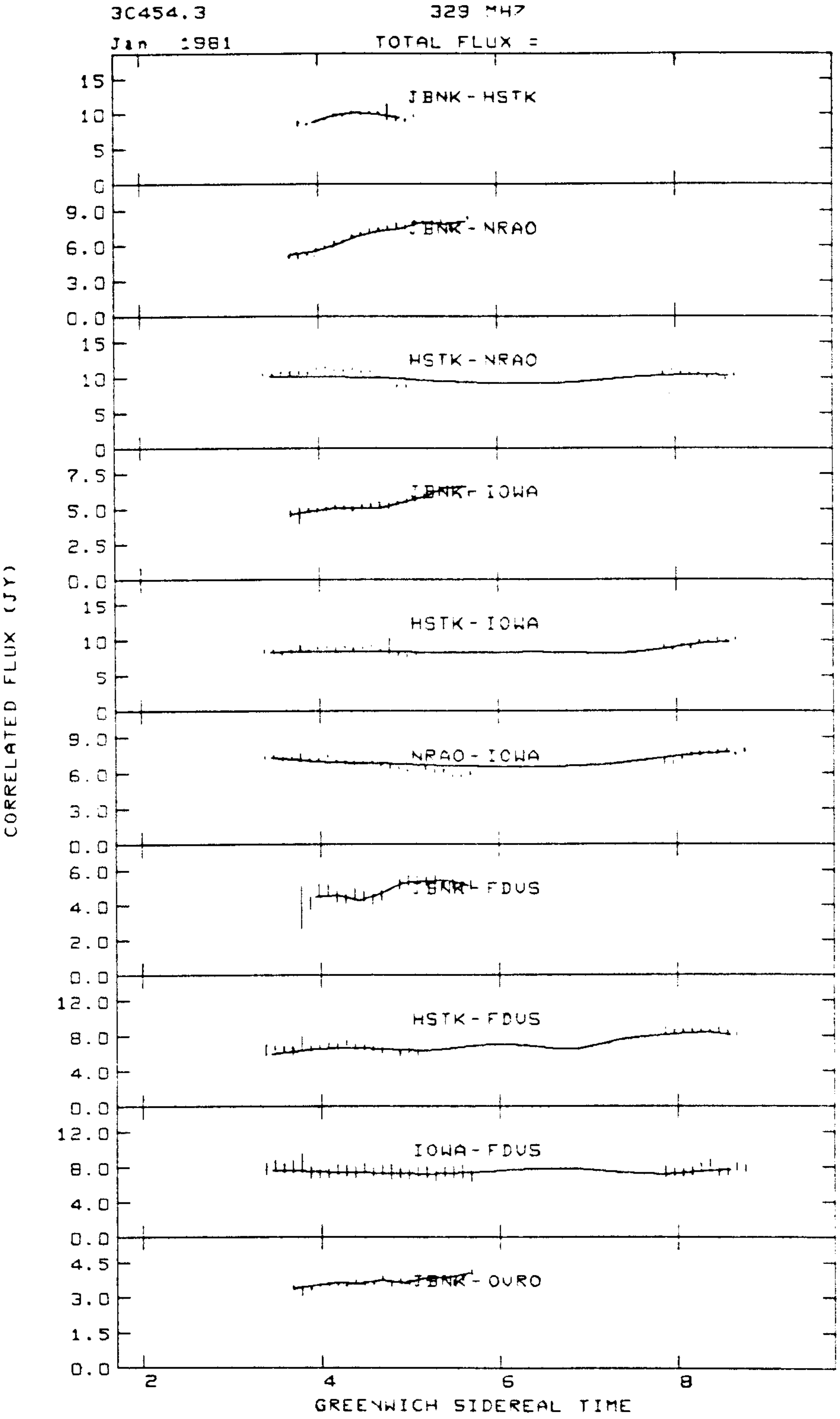
3C454.3
329 MHZ
Jan 1981
TOTAL FLUX =
CORRELATED FLUX (JY)
JBNK-HSTK
JBNK-NRAO
HSTK-NRAO
JBNK-IOWA
HSTK-IOWA
NRAO-IOWA
JBNK-FDUS
HSTK-FDUS
IOWA-FDUS
JBNK-OVRO
15
10
5
0
9.0
6.0
3.0
0.0
7.5
5.0
2.5
12.0
8.0
4.0
4.5
3.0
1.5
2
4
6
8
GREENWICH SIDEREAL TIME

Figure 2b

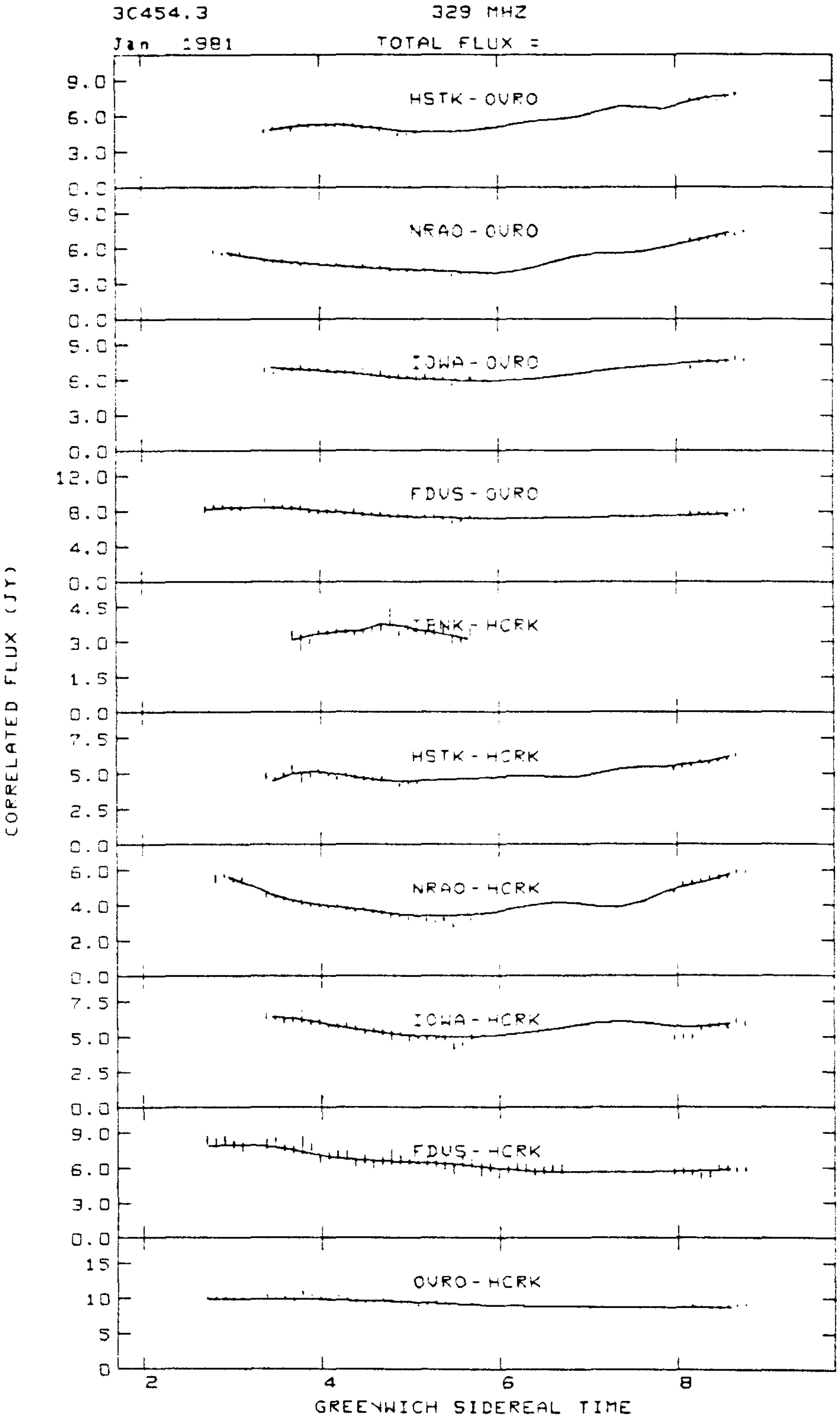

Figure 2b (continued)

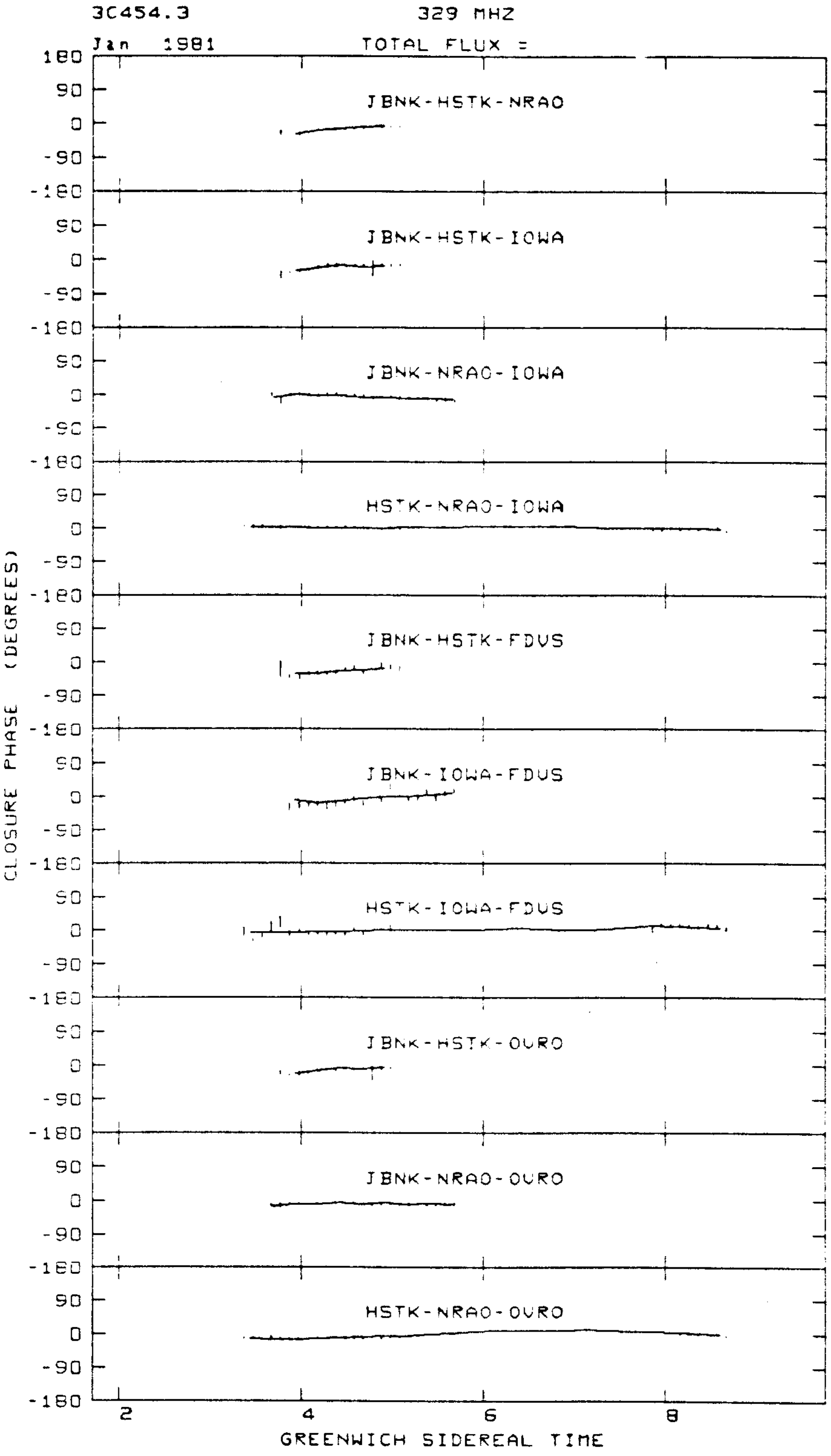

Figure 2b (continued)

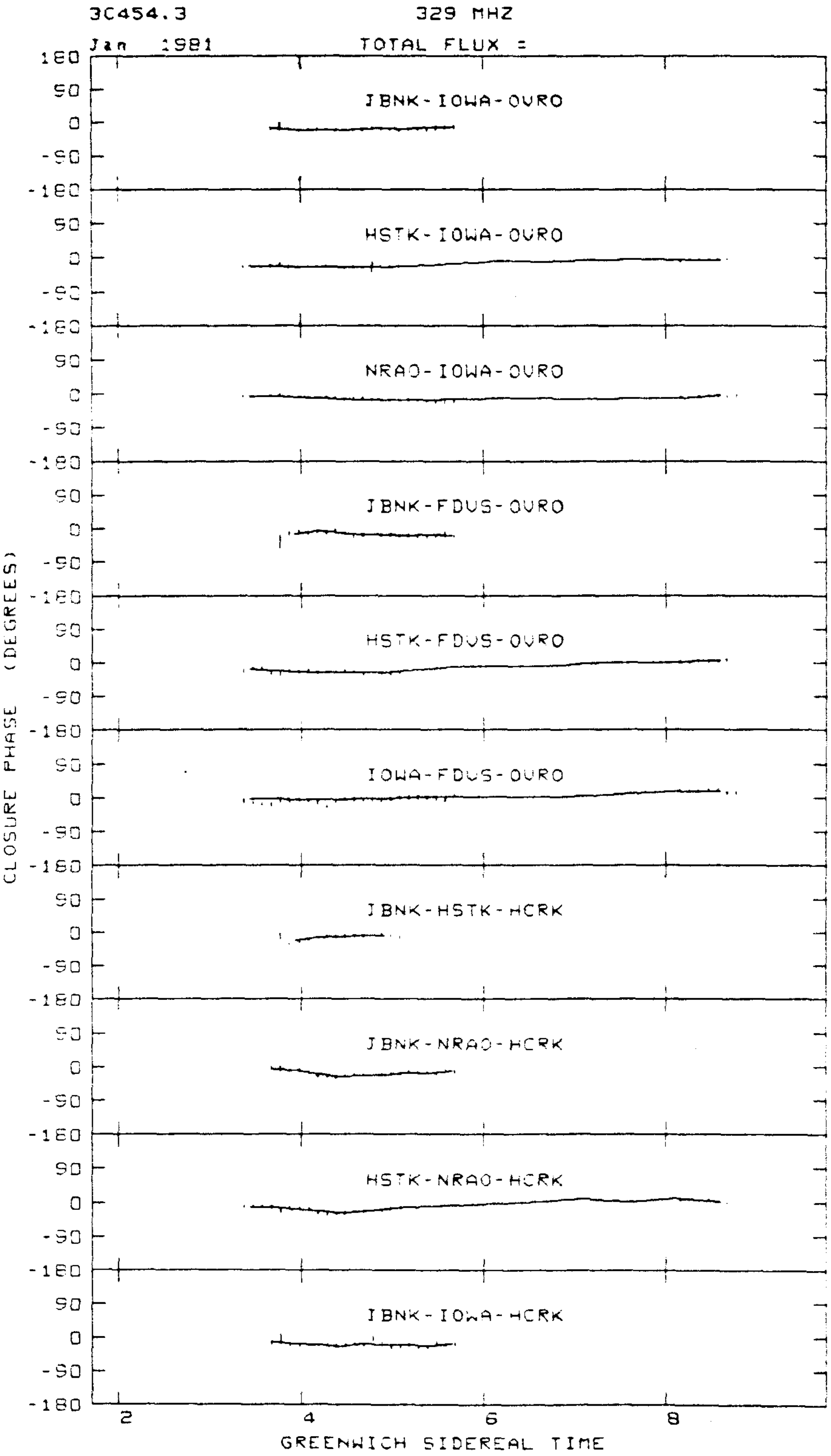

Figure 2b (continued)

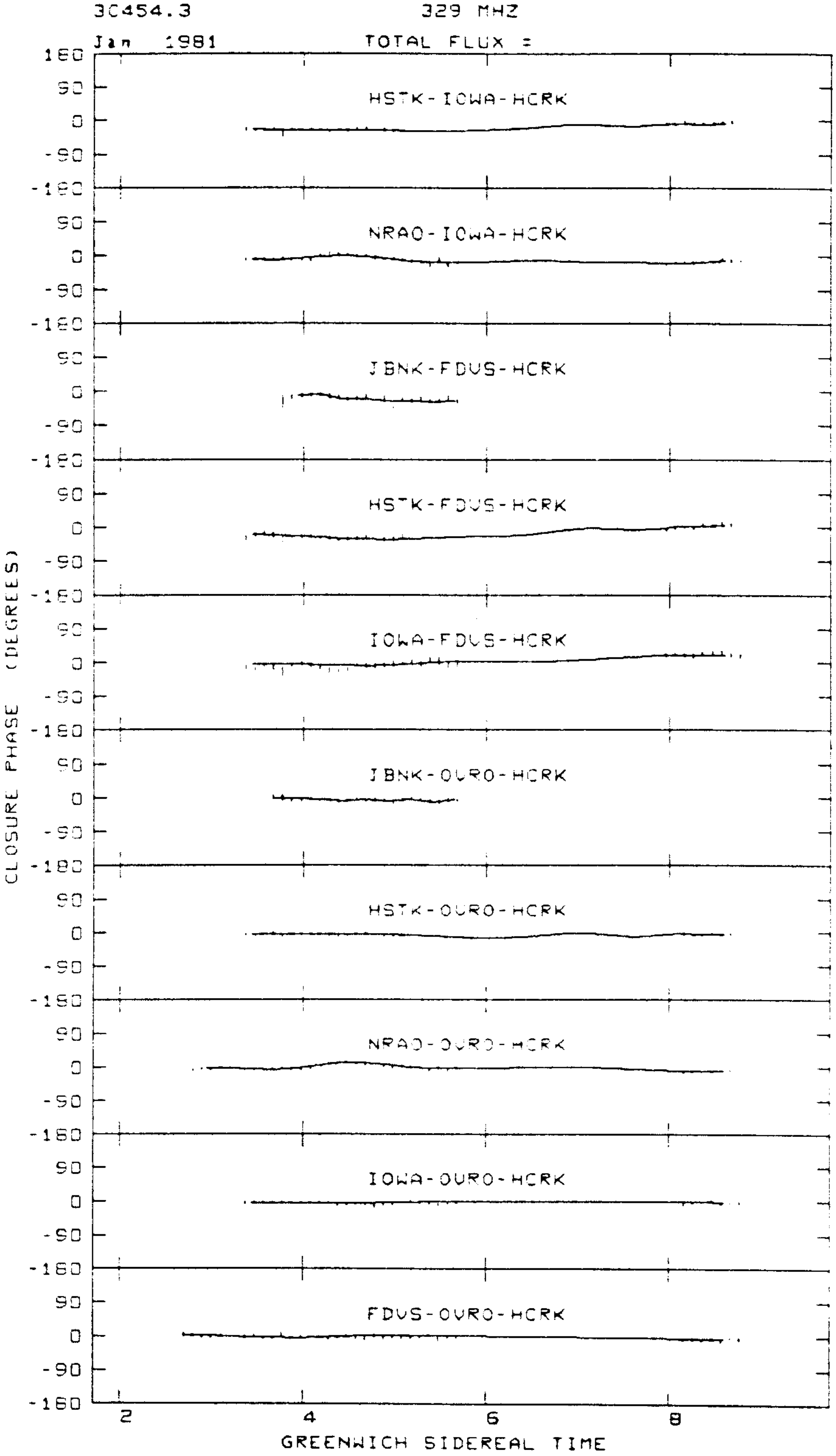

Figure 2b (continued)

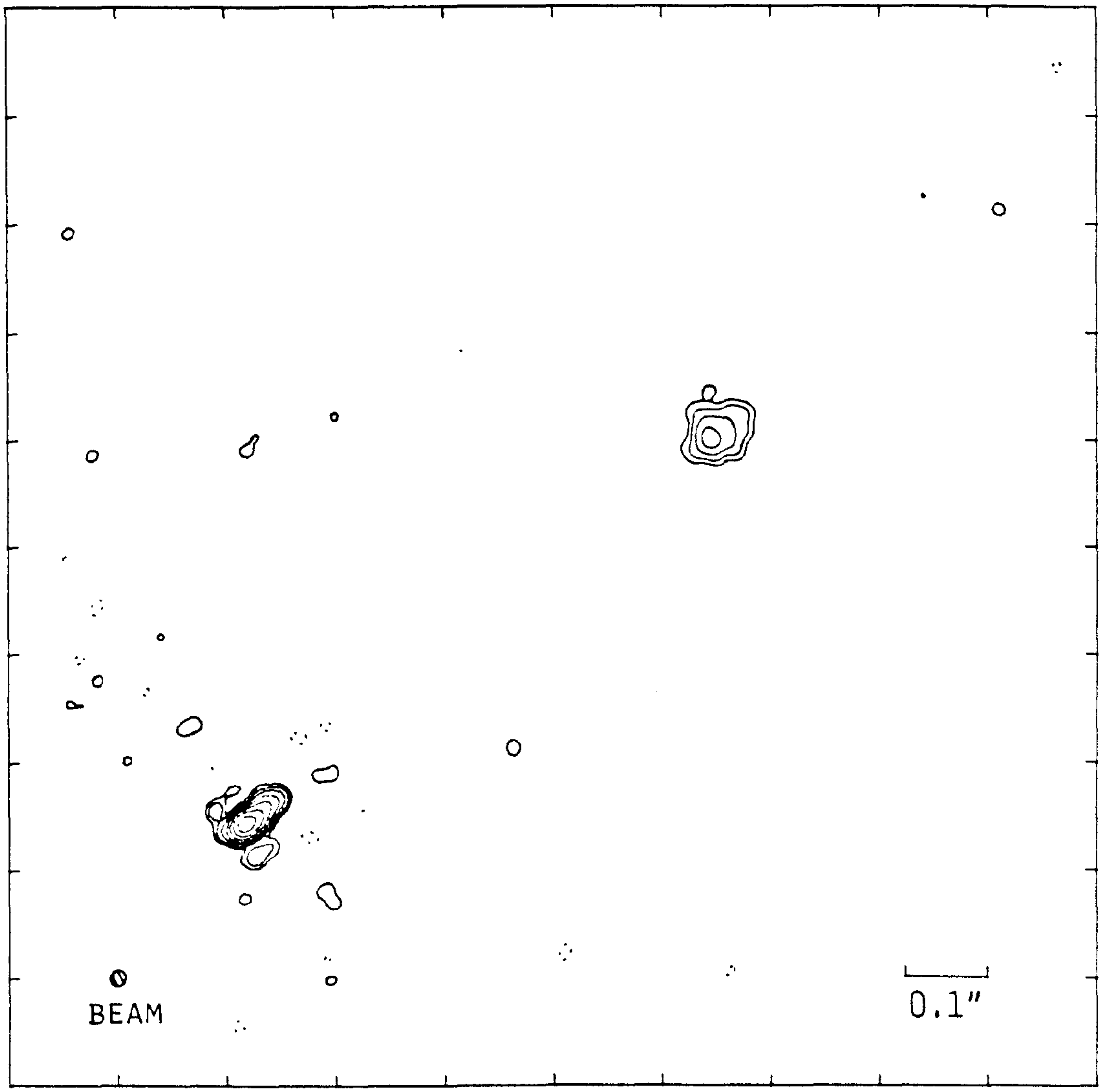

Figure 3a

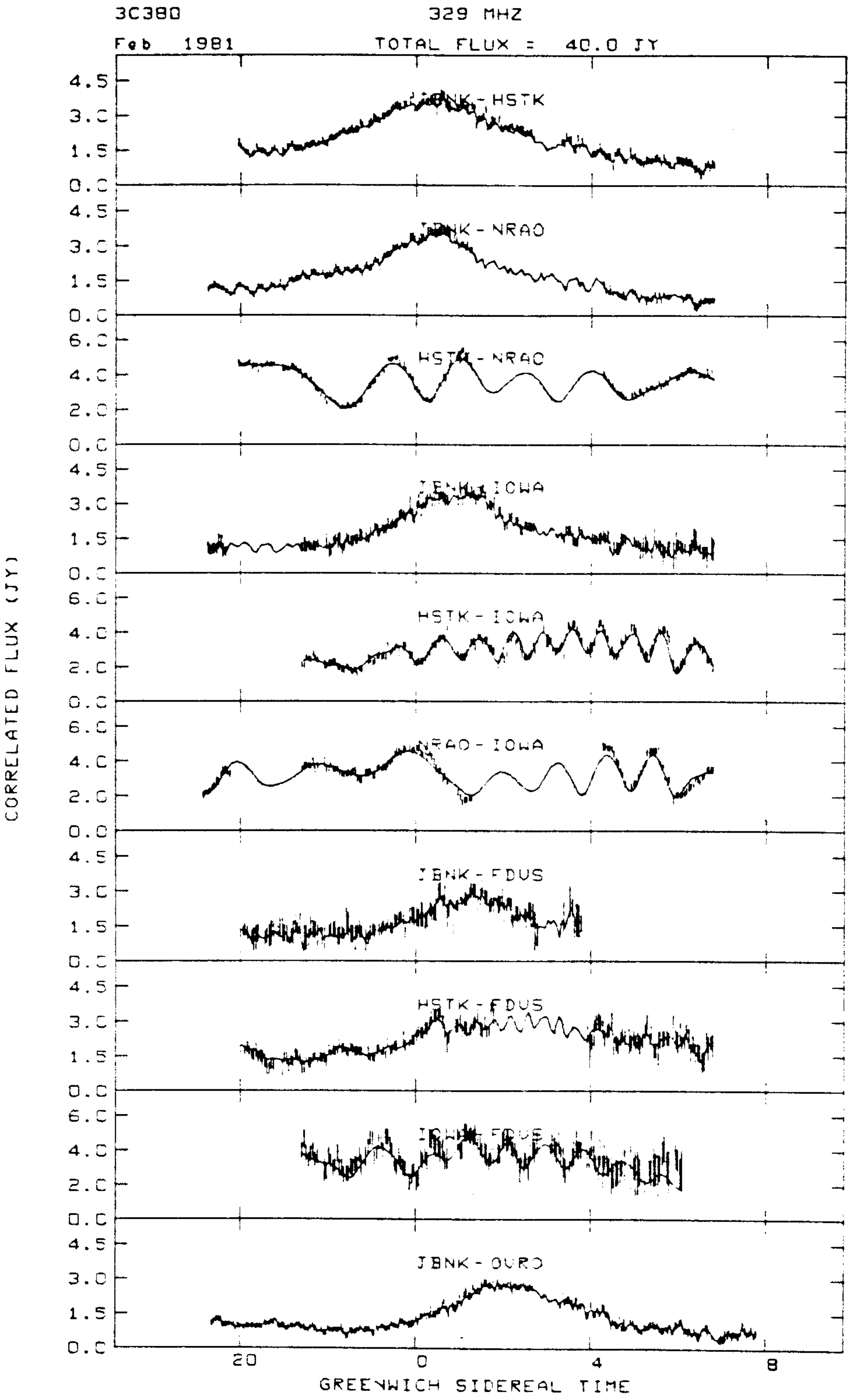
3C380
329 MHZ
Feb 1981
TOTAL FLUX = 40.0 JY
JBNK - HSTK
JBNK - NRAO
HSTK - NRAO
JBNK - IOWA
HSTK - IOWA
NRAO - IOWA
JBNK - FDVS
HSTK - FDVS
IOWA - FDVS
JBNK - OVRO
4.5
3.0
1.5
0.0
6.0
4.0
2.0
CORRELATED FLUX (JY)
20
0
4
8
GREENWICH SIDEREAL TIME

Figure 3b

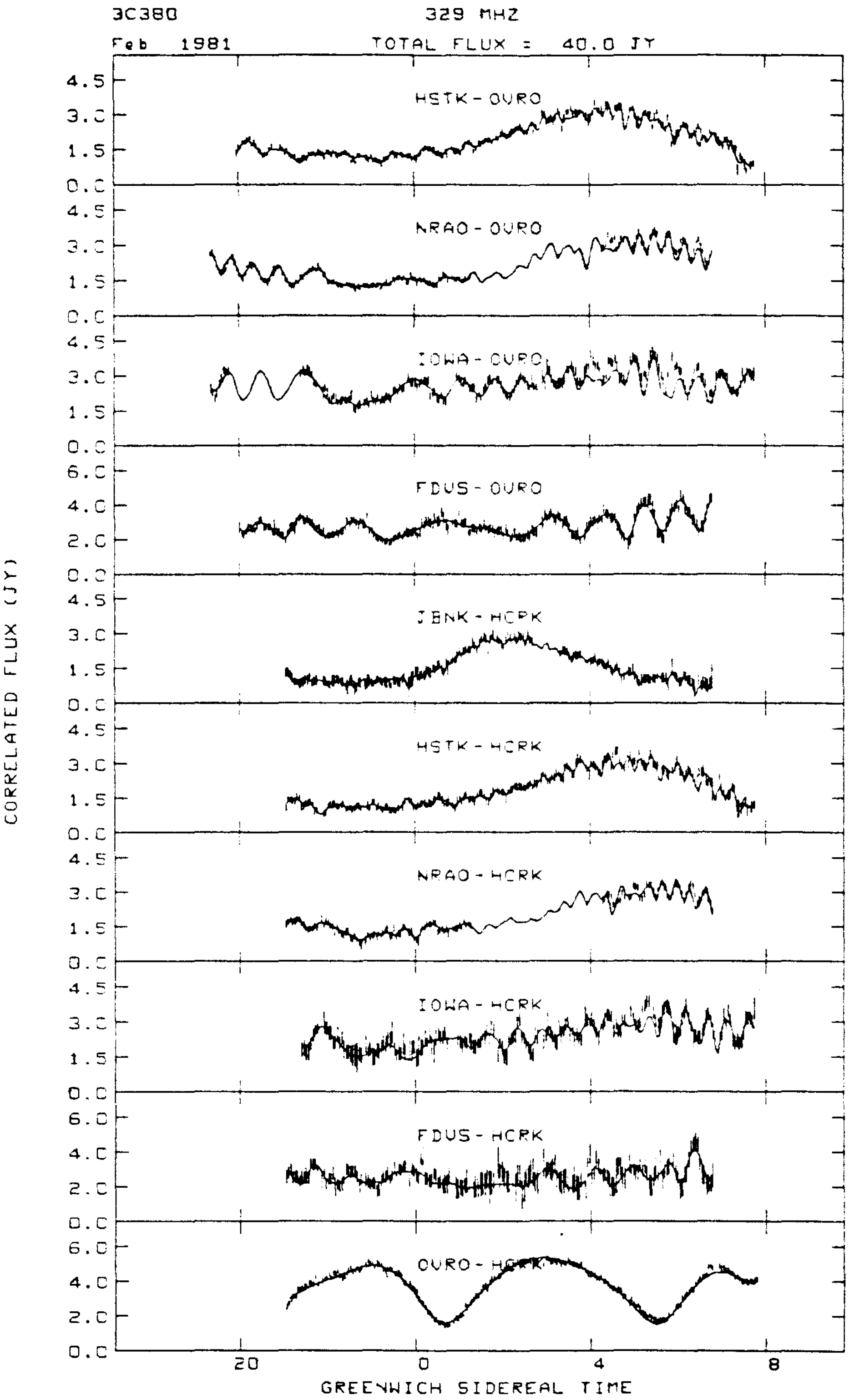

Figure 3b (continued)

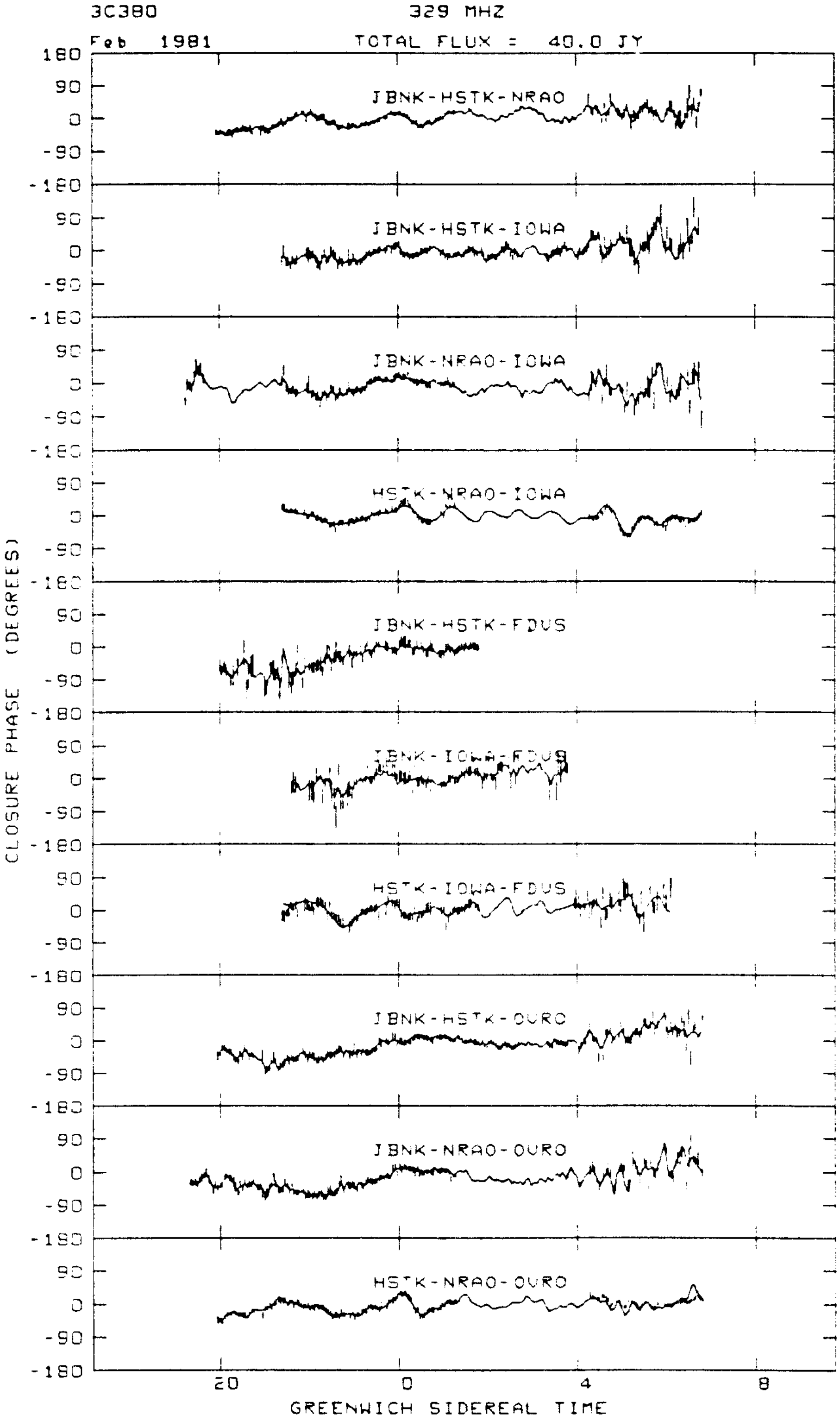

Figure 3b (continued)

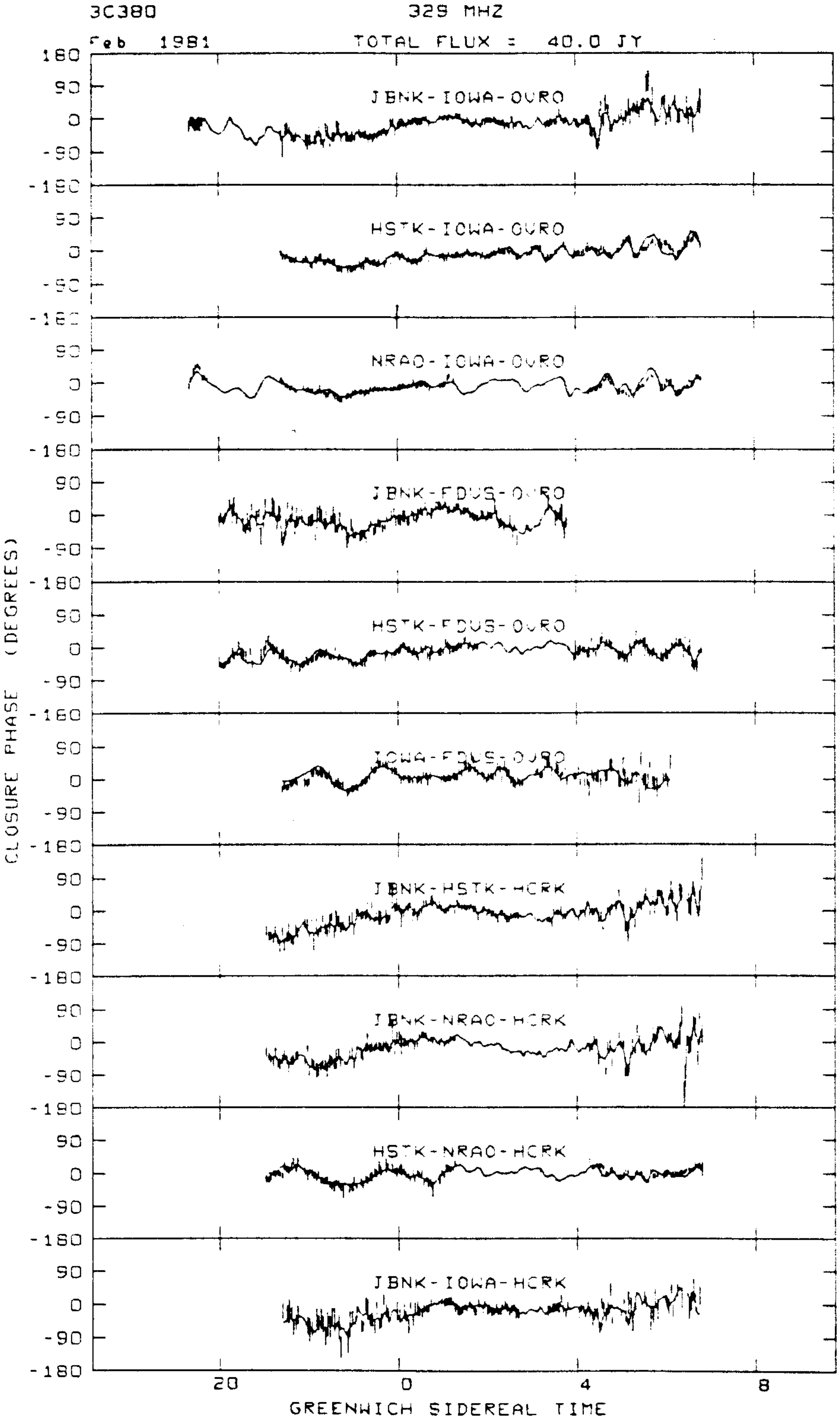

Figure 3b (continued)

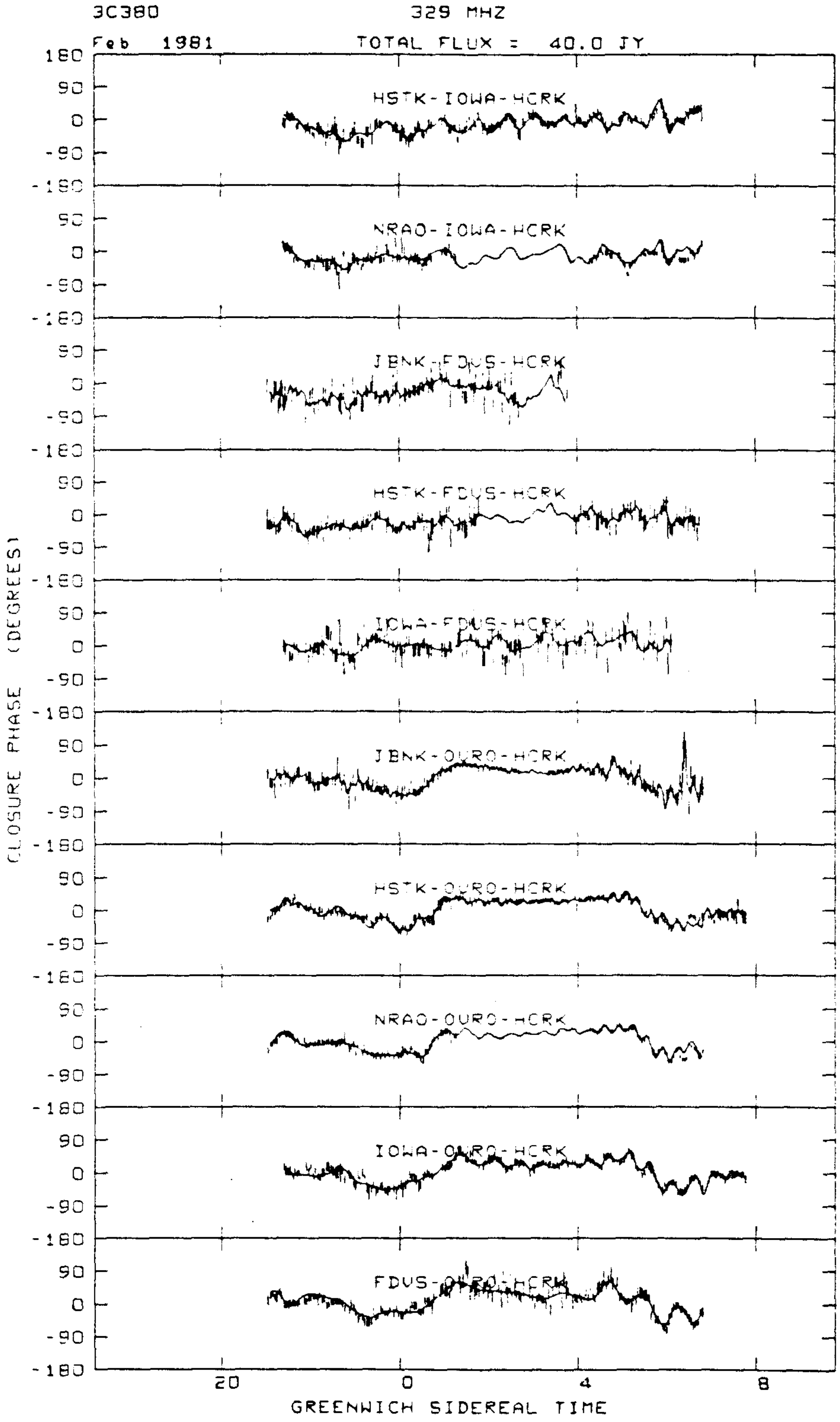

Figure 3b (continued)

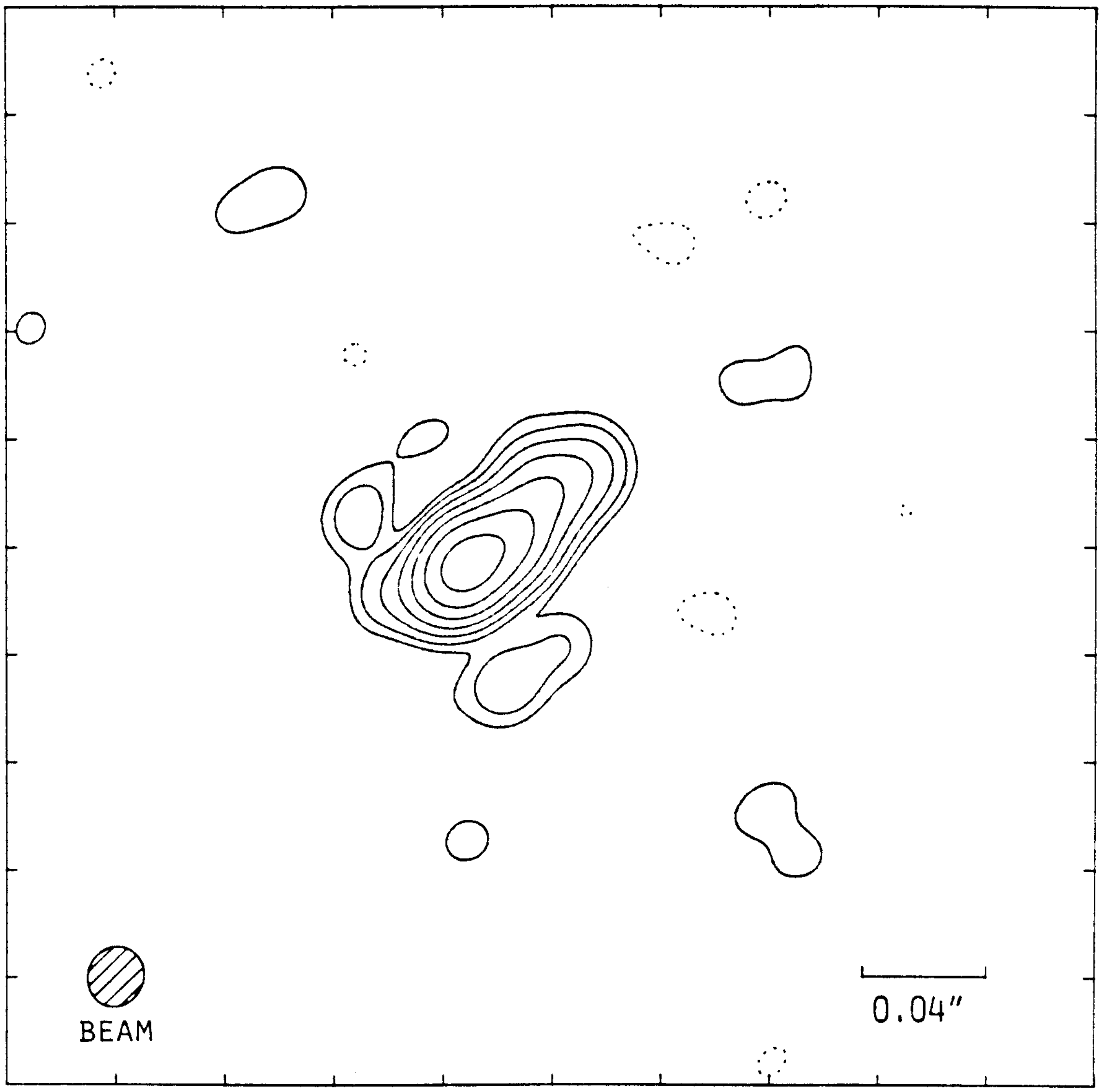

Figure 3c

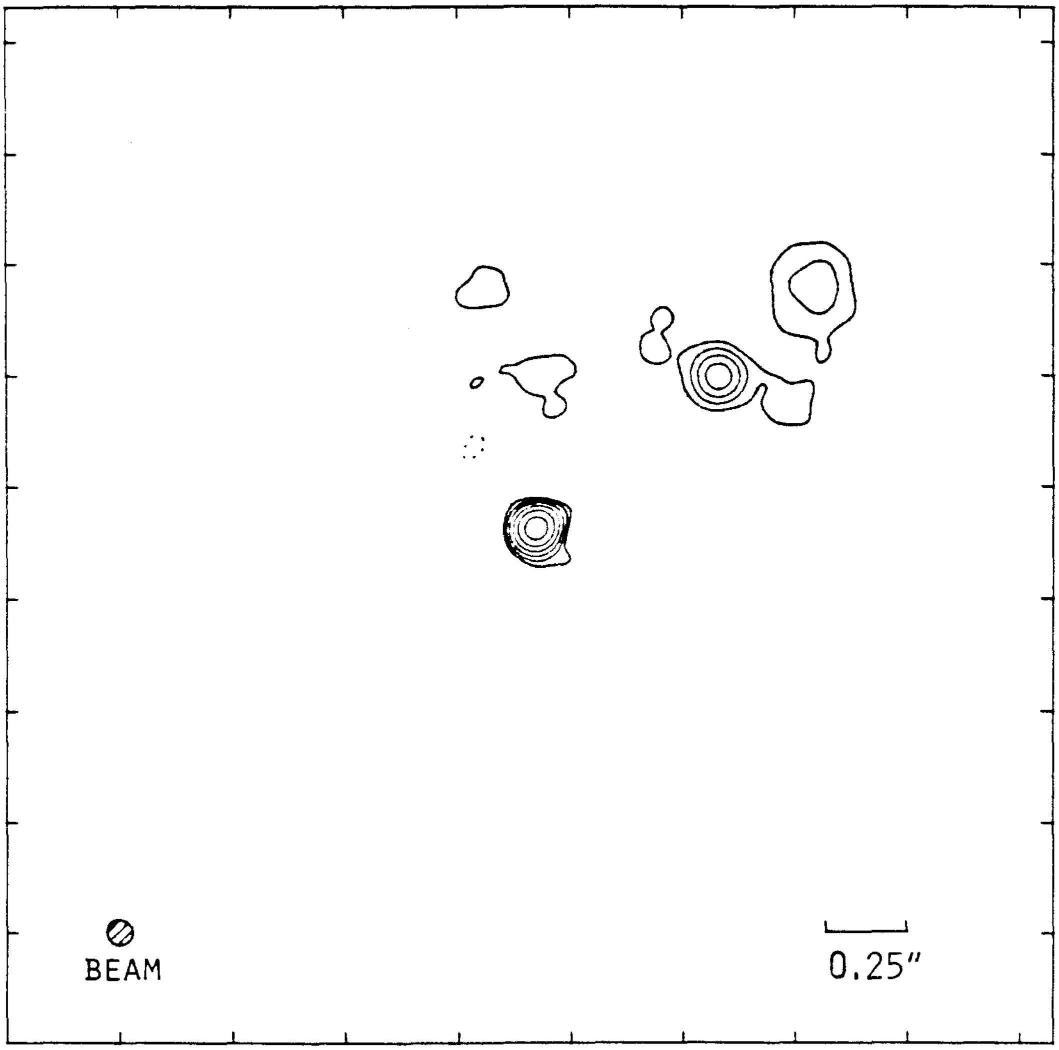

Figure 3d

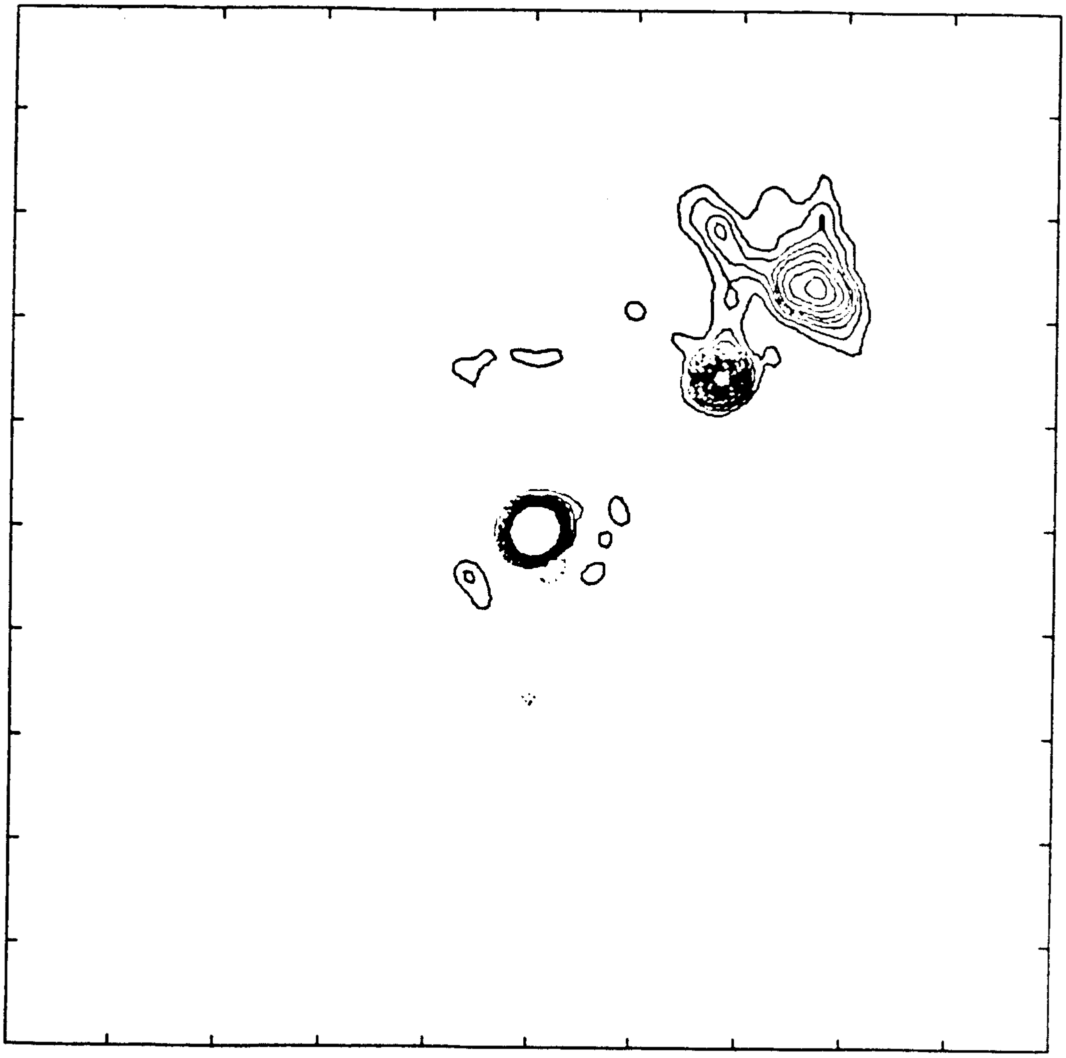

Figure 3e

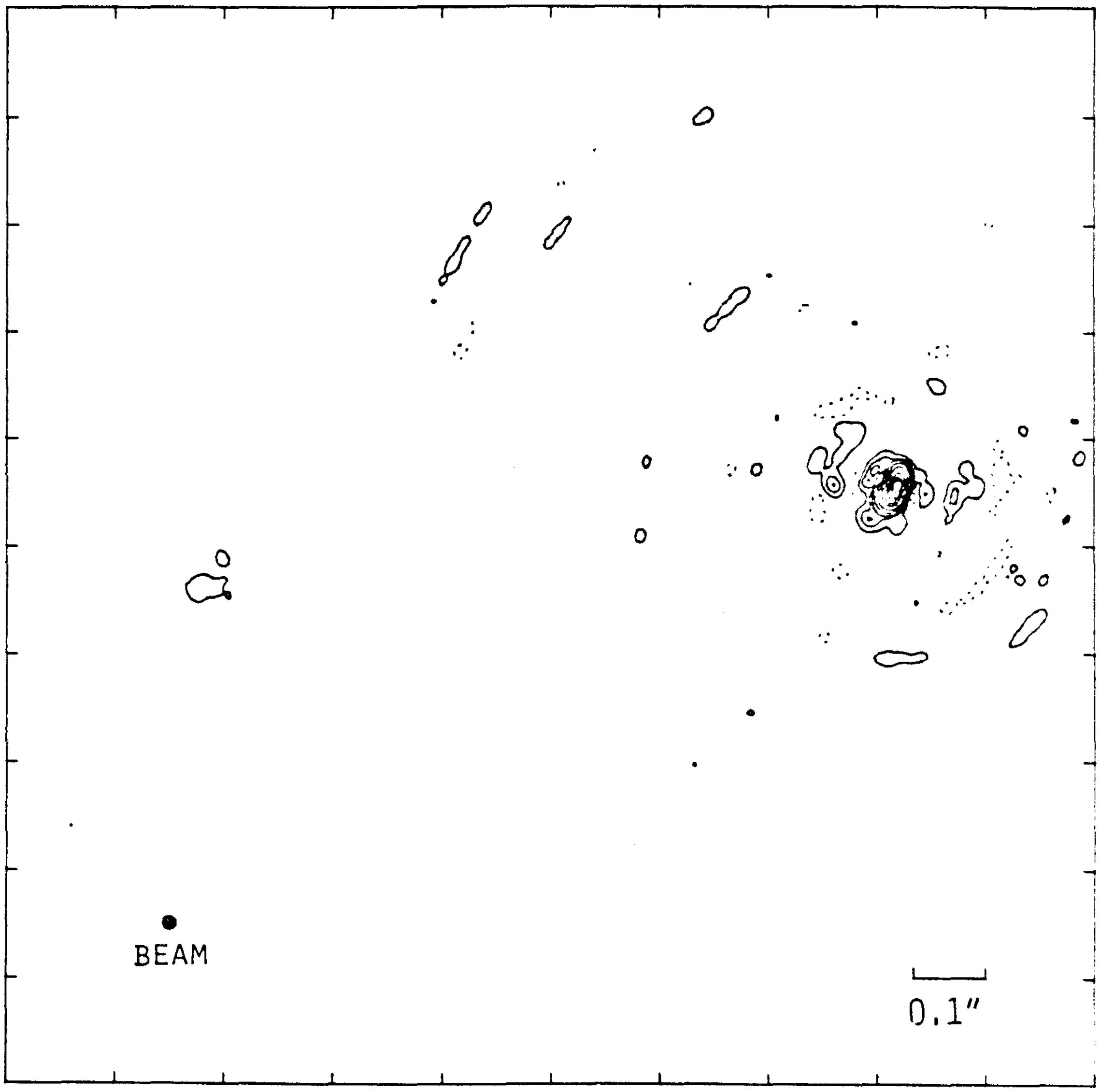

Figure 4a

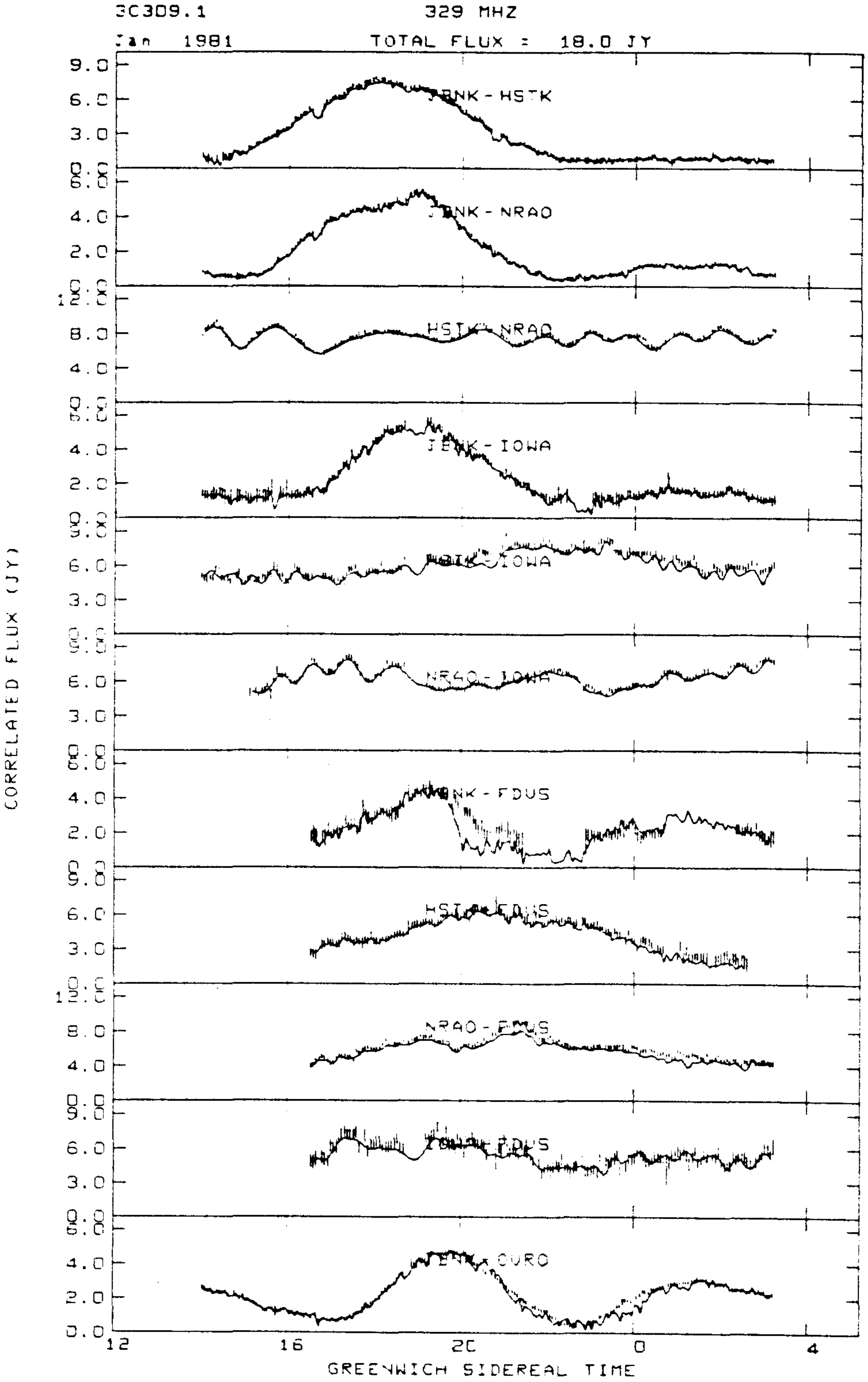
3C309.1
329 MHZ
Jan 1981
TOTAL FLUX = 18.0 JY
JBNK-HSTK
JBNK-NRAO
HSTK-NRAO
JBNK-IOWA
HSTK-IOWA
NRAO-IOWA
JBNK-FDUS
HSTK-FDUS
NRAO-FDUS
IOWA-FDUS
JBNK-OVRO
9.0
6.0
3.0
0.0
4.0
2.0
12.0
8.0
CORRELATED FLUX (JY)
12
16
20
0
4
GREENWICH SIDEREAL TIME

Figure 4b

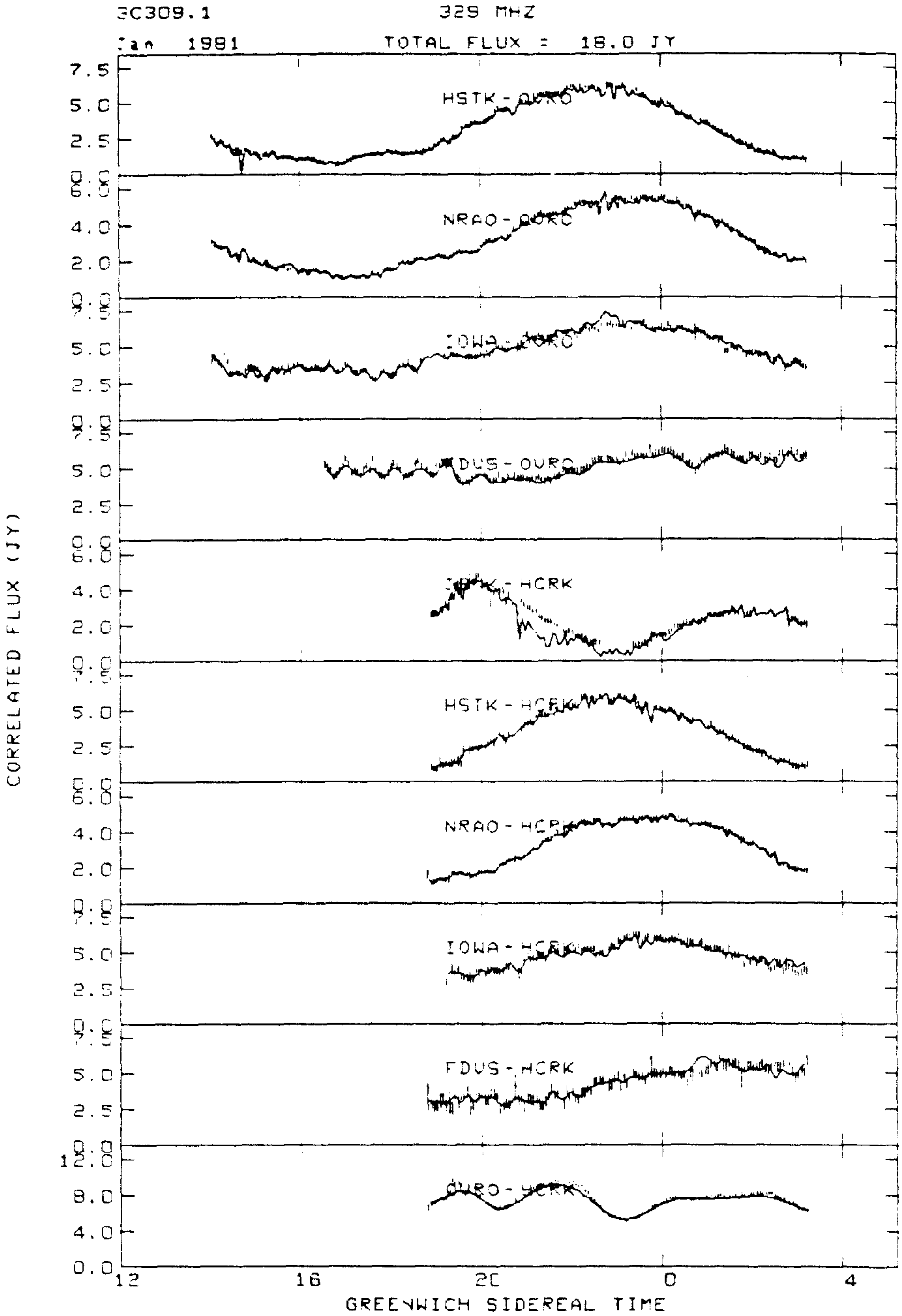

Figure 4b (continued)

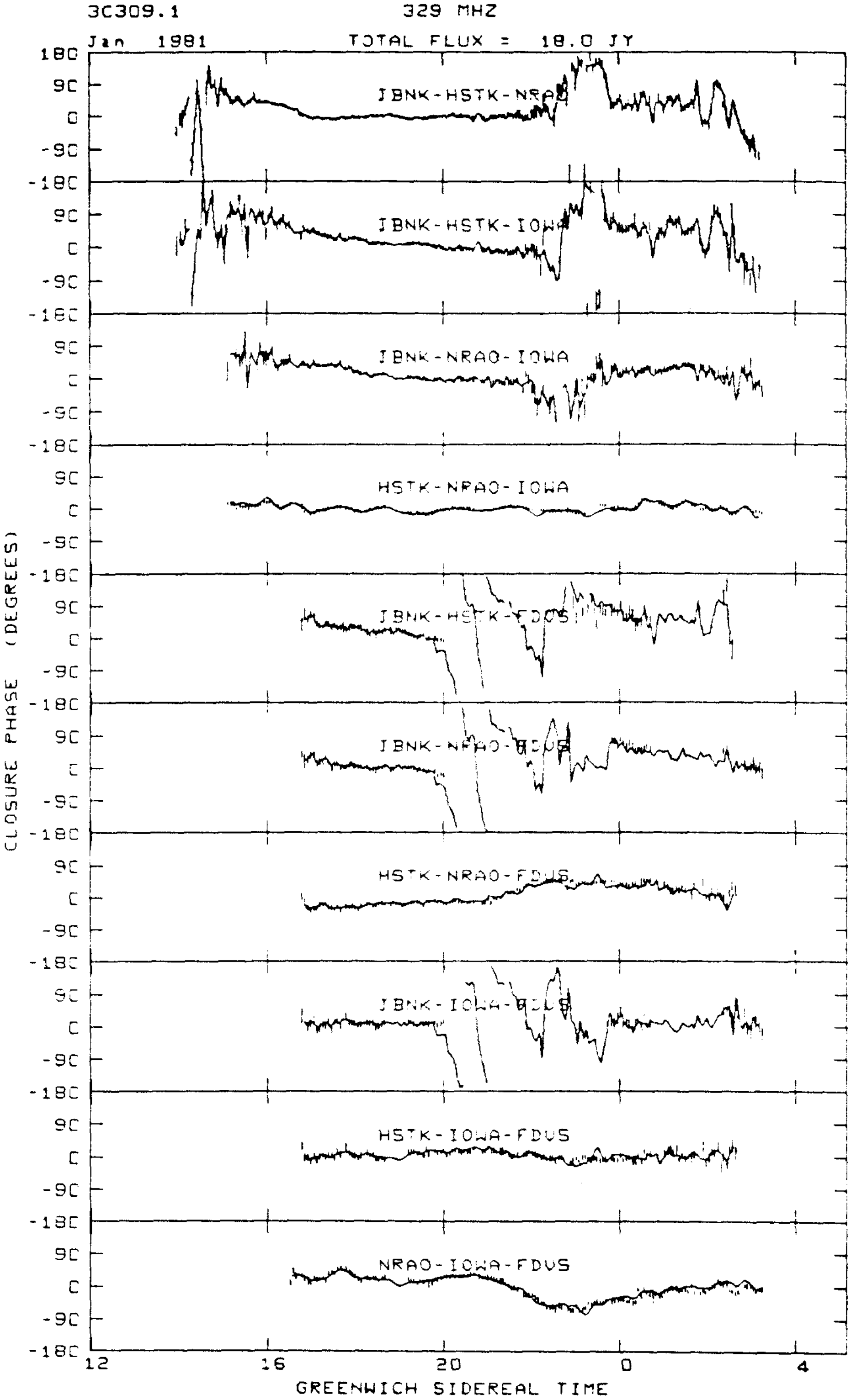

Figure 4b (continued)

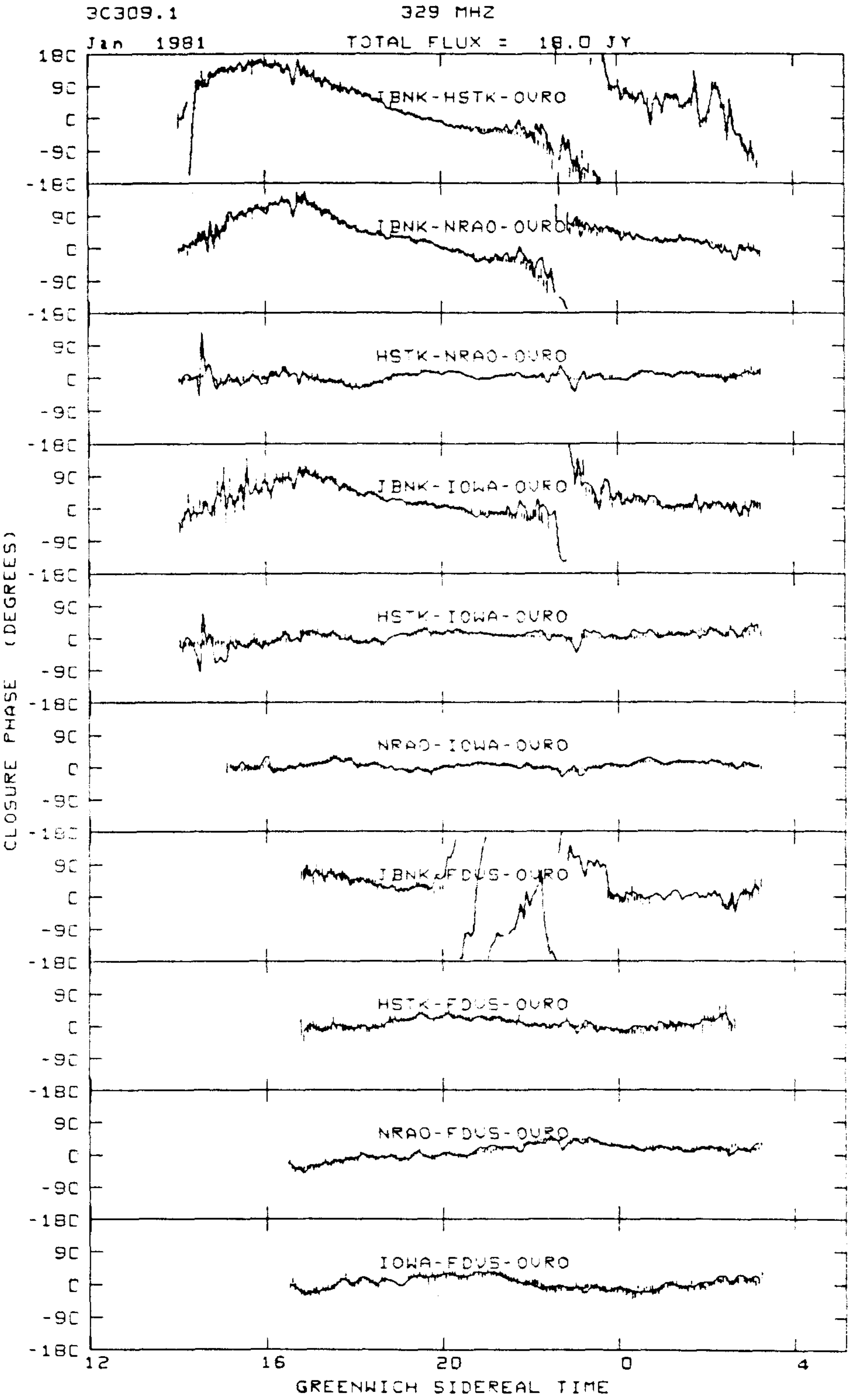

Figure 4b (continued)

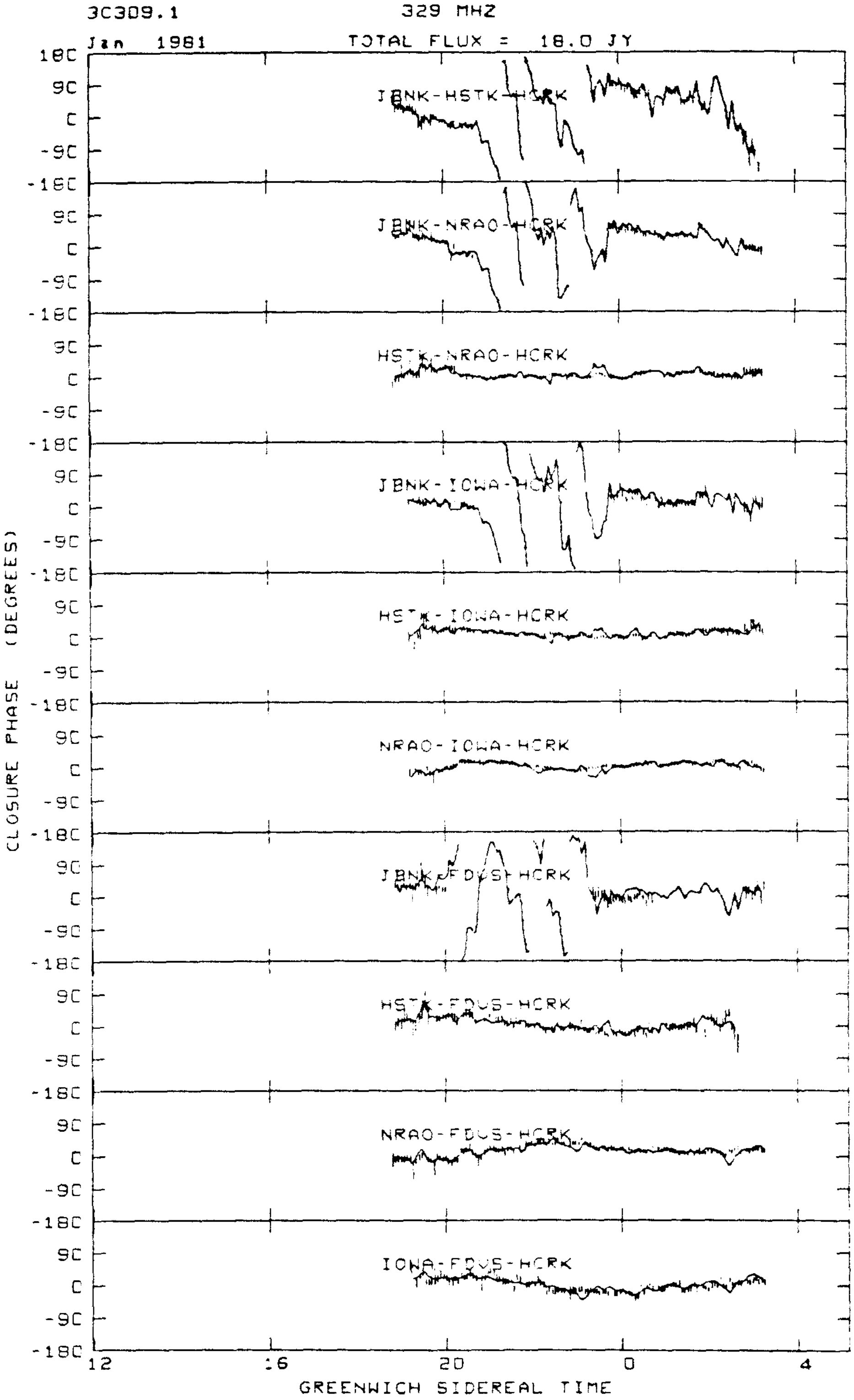

Figure 4b (continued)

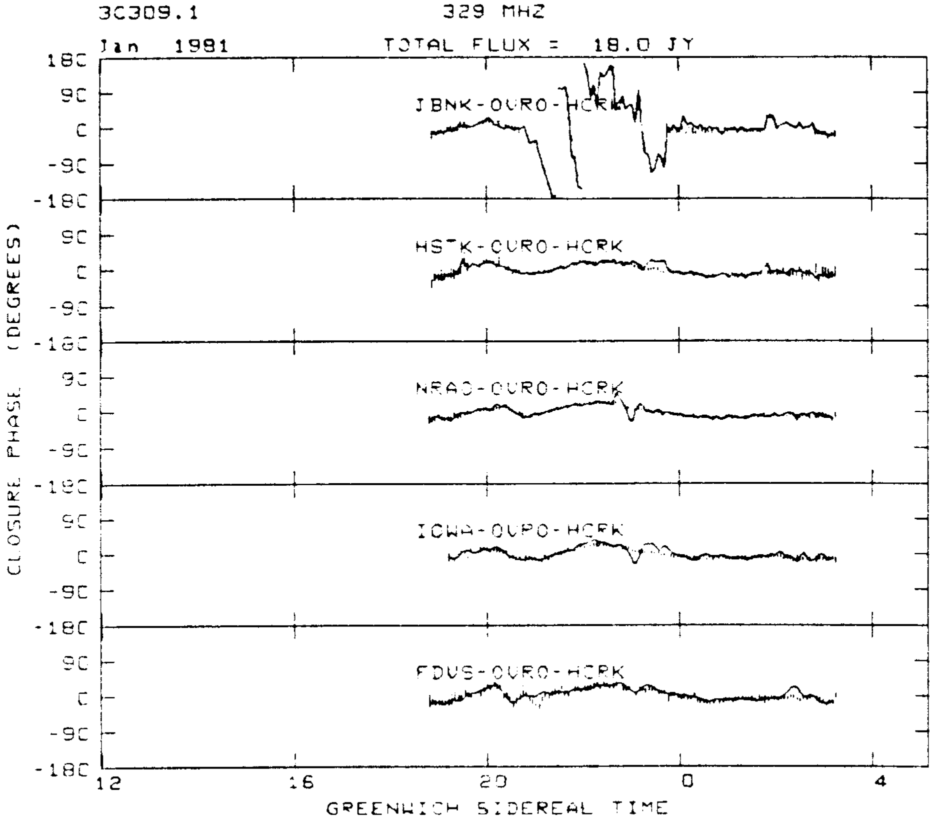

Figure 4b (continued)

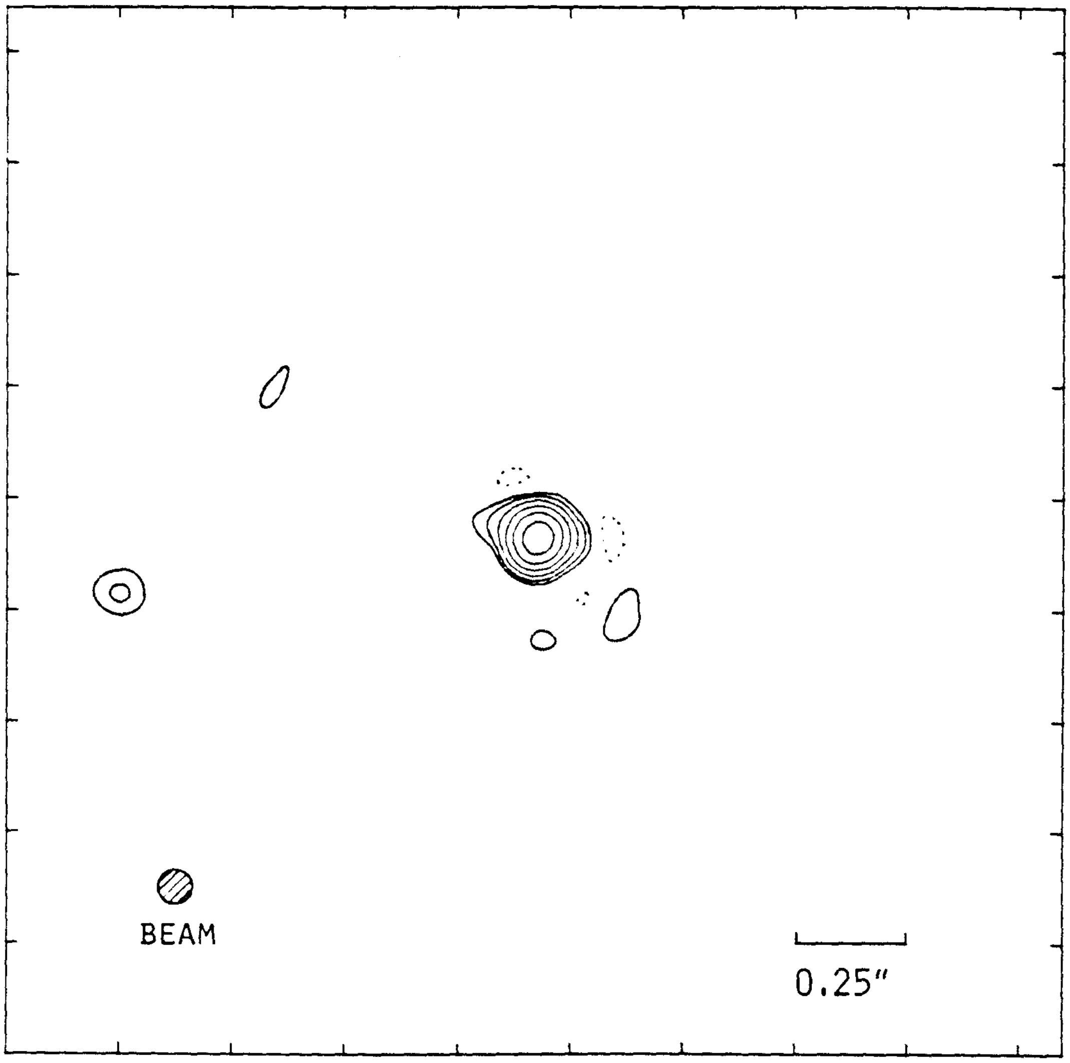

Figure 4c

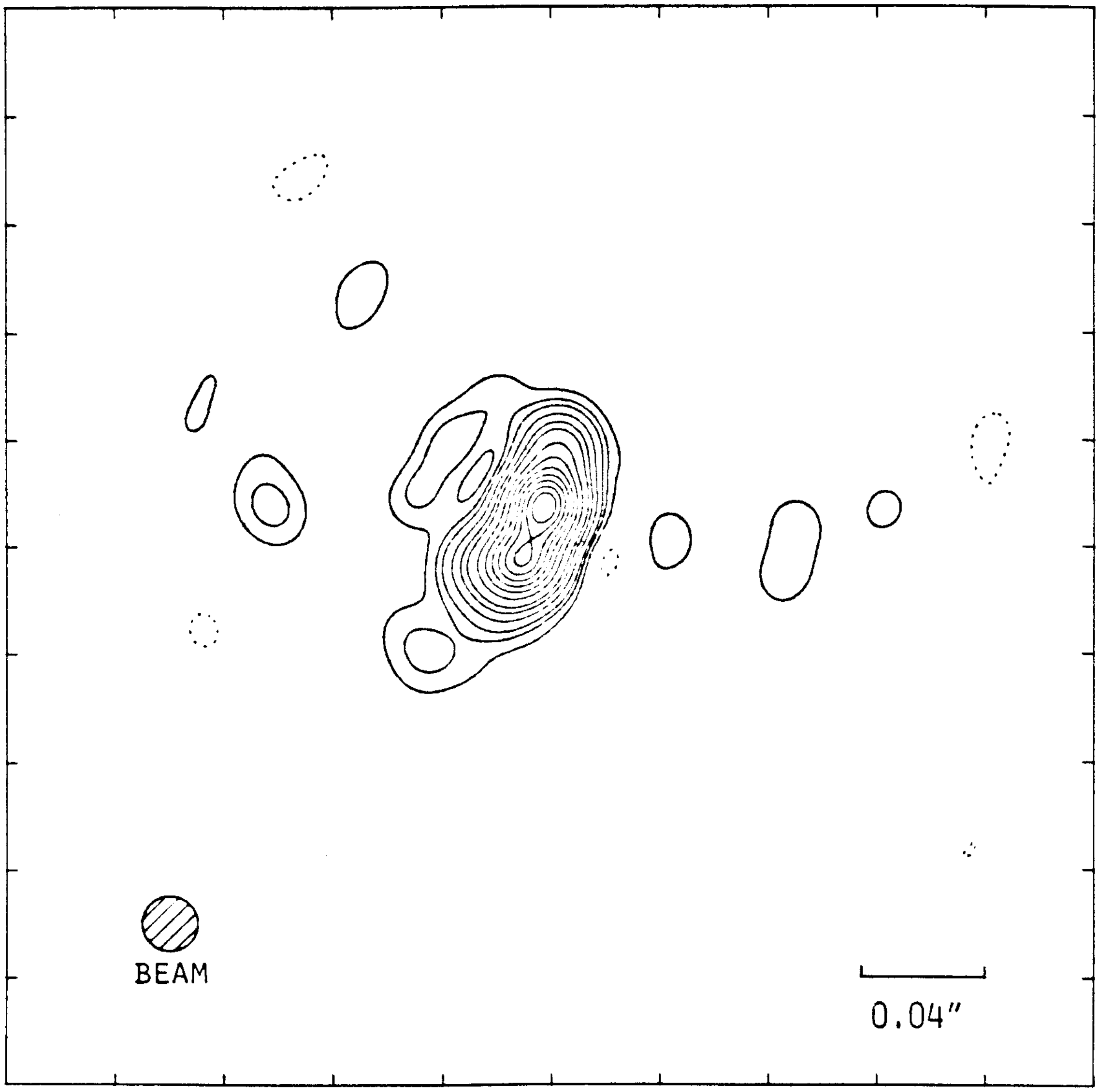

Figure 4d

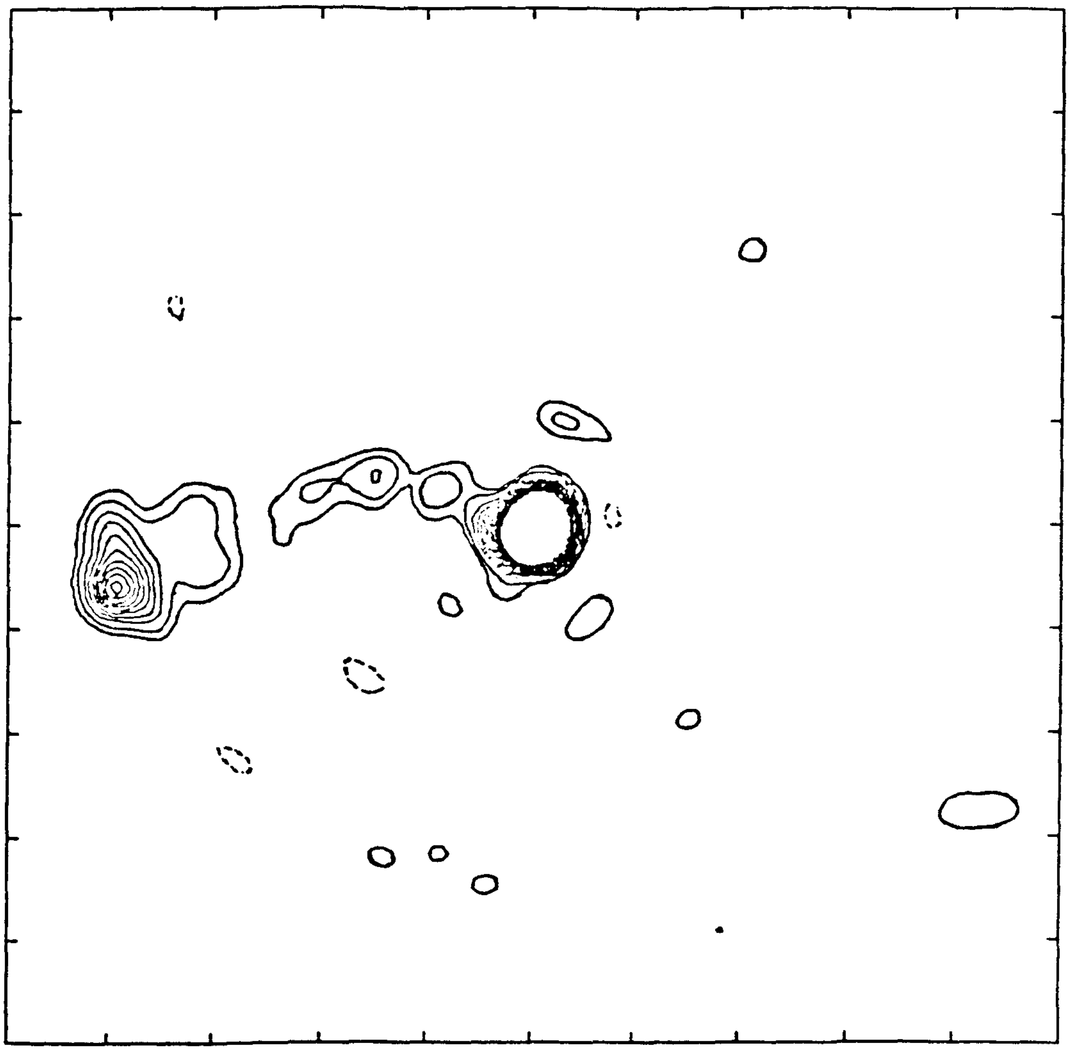

Figure 4e

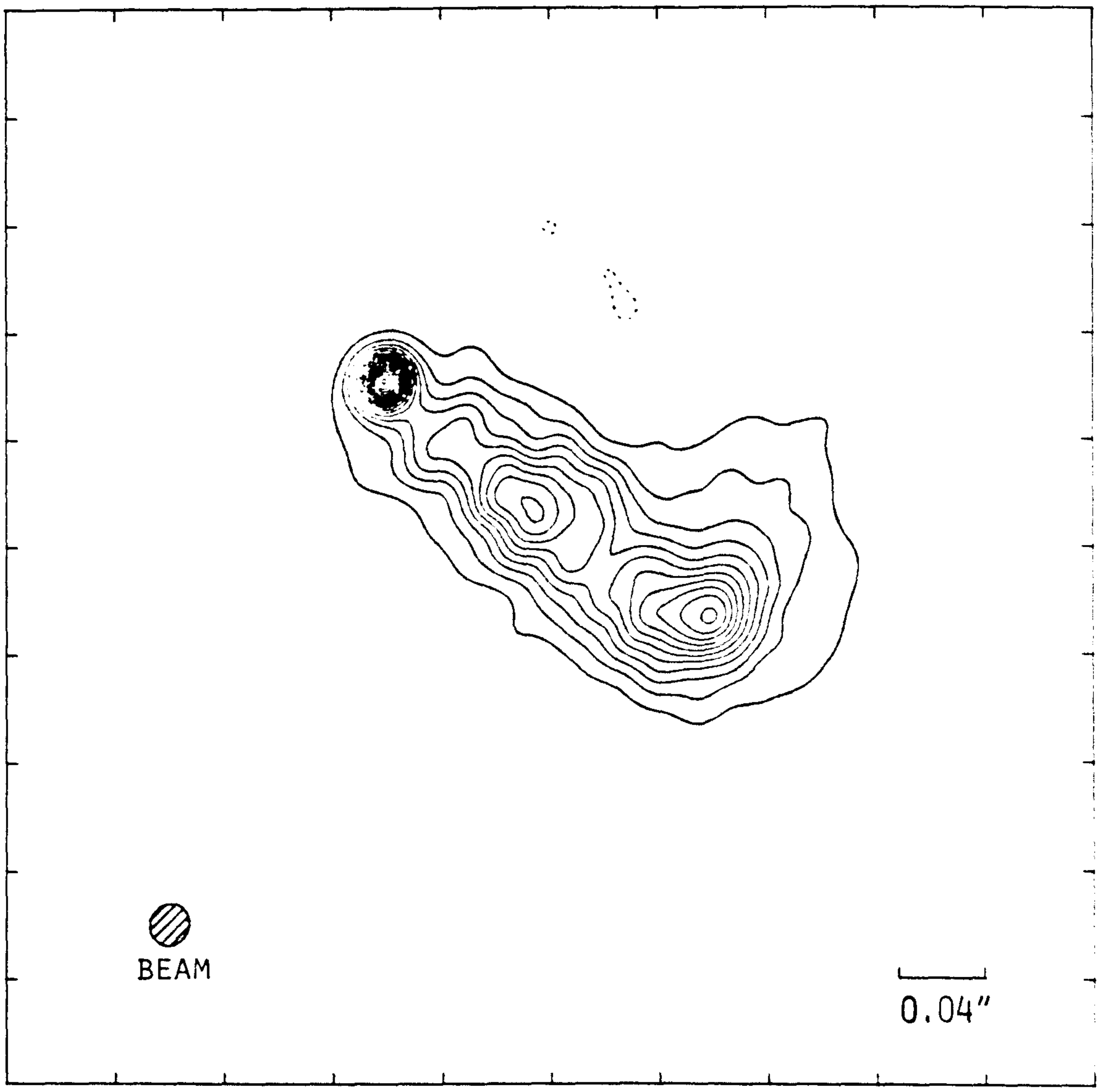

Figure 5a

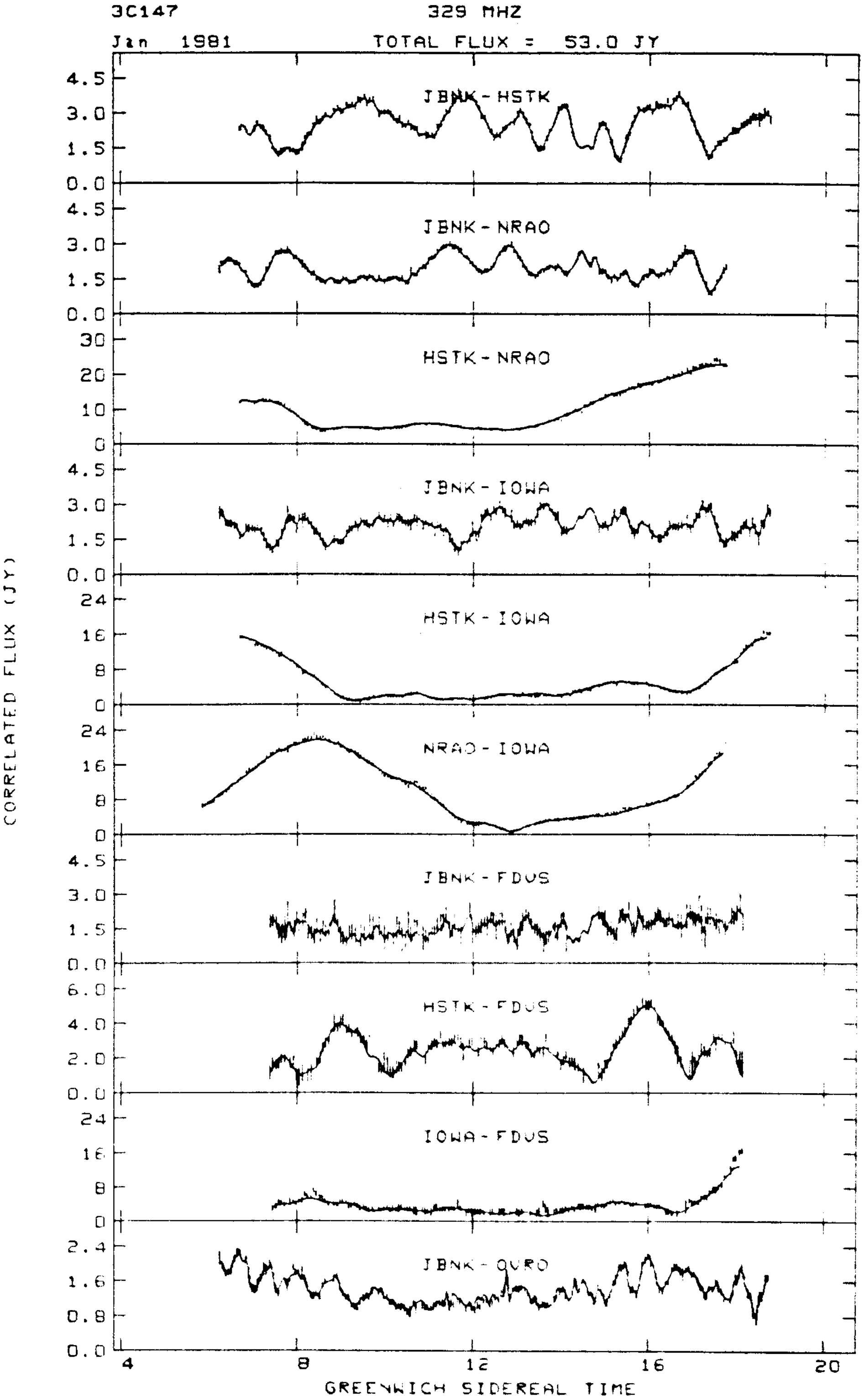
3C147
Jan 1981
329 MHZ
TOTAL FLUX = 53.0 JY
JBNK-HSTK
JBNK-NRAO
HSTK-NRAO
JBNK-IOWA
HSTK-IOWA
NRAO-IOWA
JBNK-FDVS
HSTK-FDVS
IOWA-FDVS
JBNK-OVRO
4.5
3.0
1.5
0.0
30
20
10
0
24
16
8
6.0
4.0
2.0
2.4
1.6
0.8
CORRELATED FLUX (JY)
4
8
12
16
20
GREENWICH SIDEREAL TIME

Figure 5b

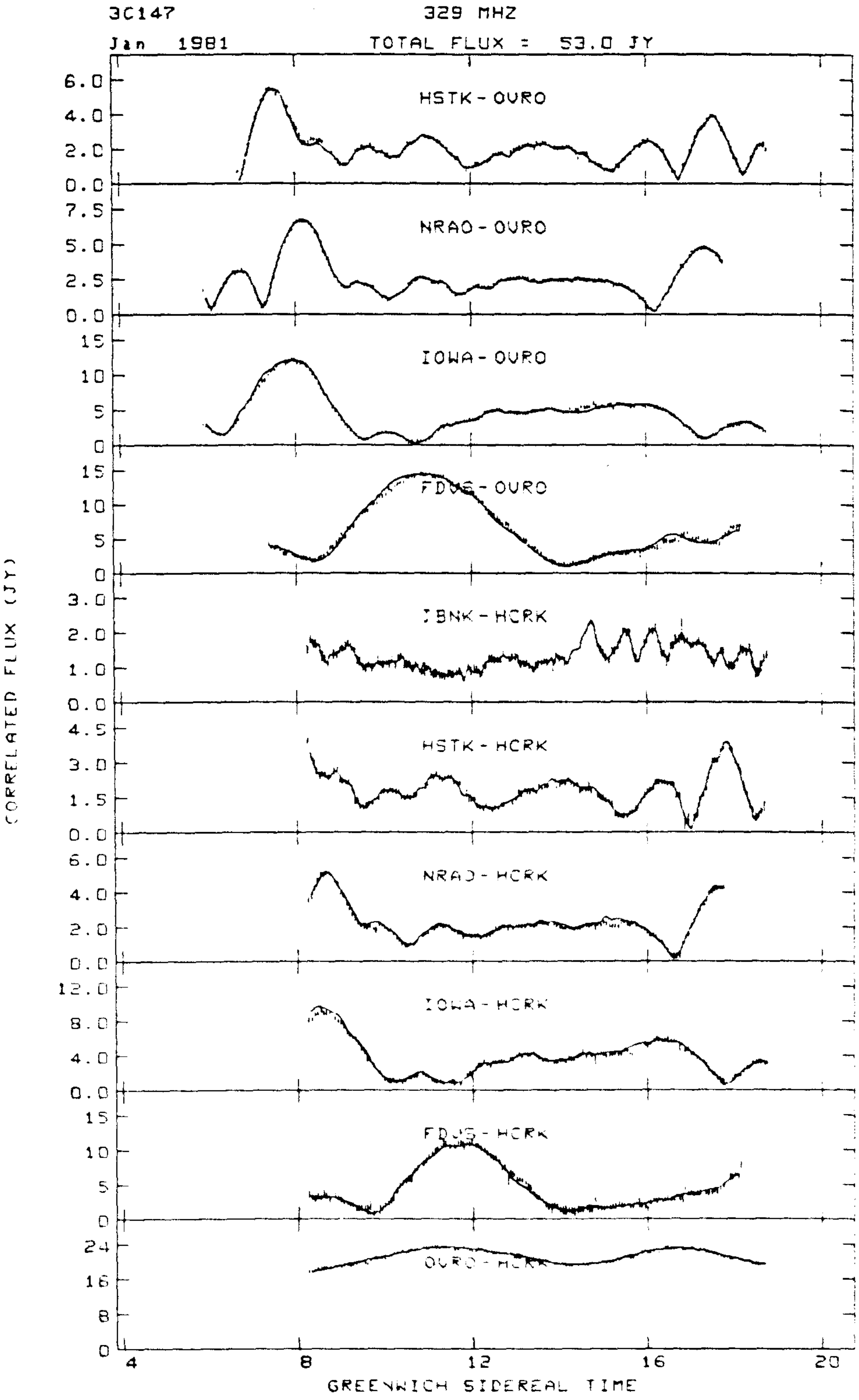

Figure 5b (continued)

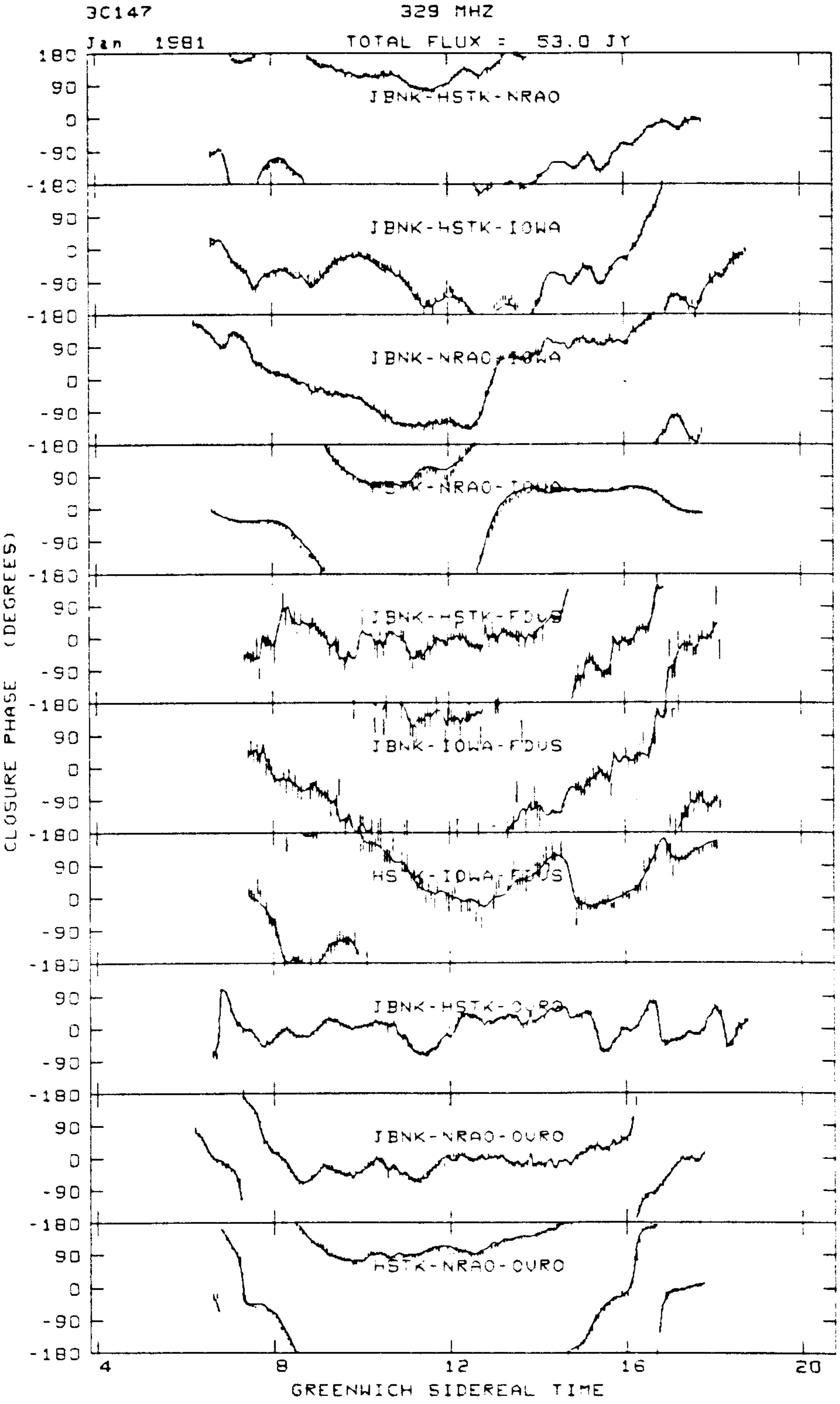

Figure 5b (continued)

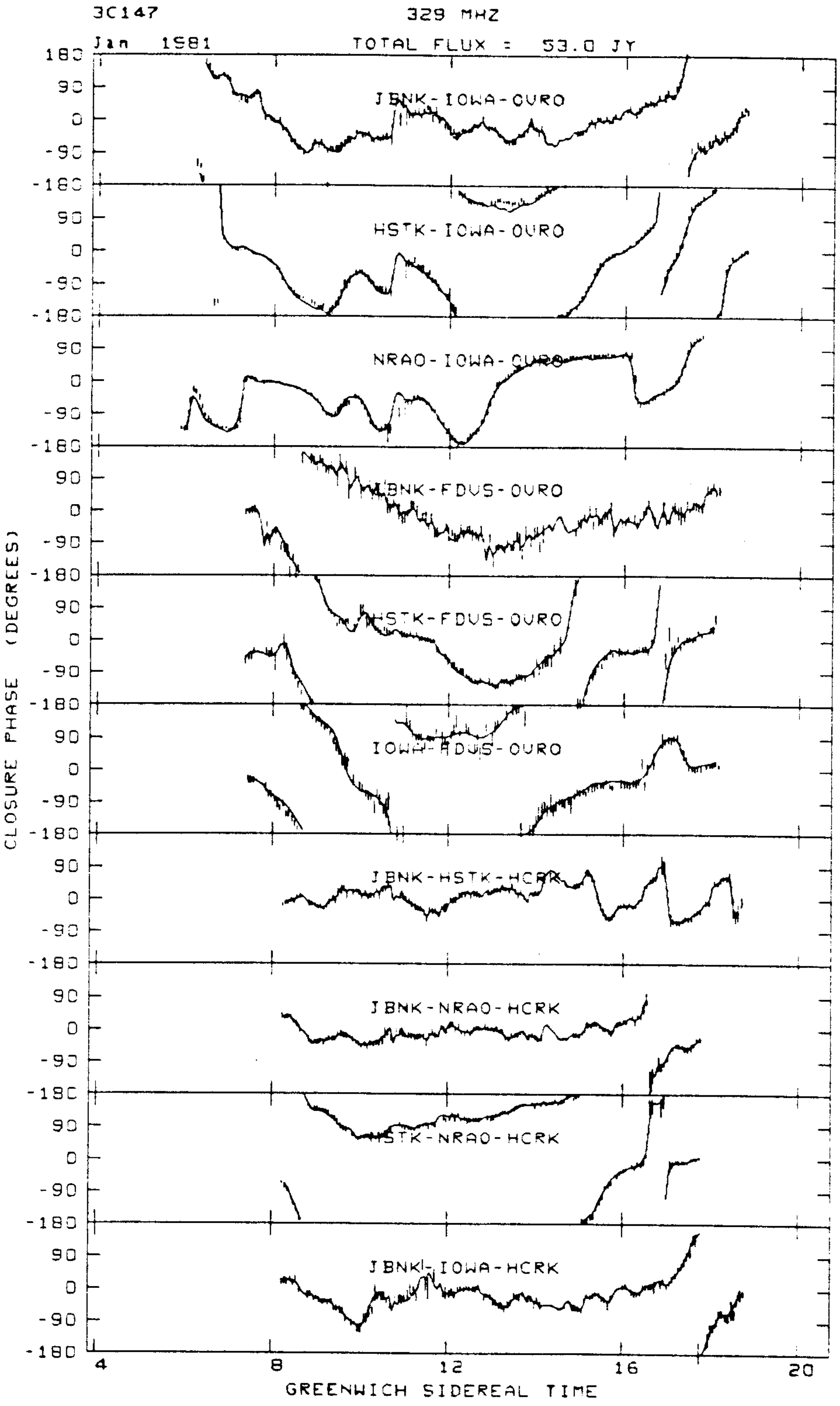

Figure 5b (continued)

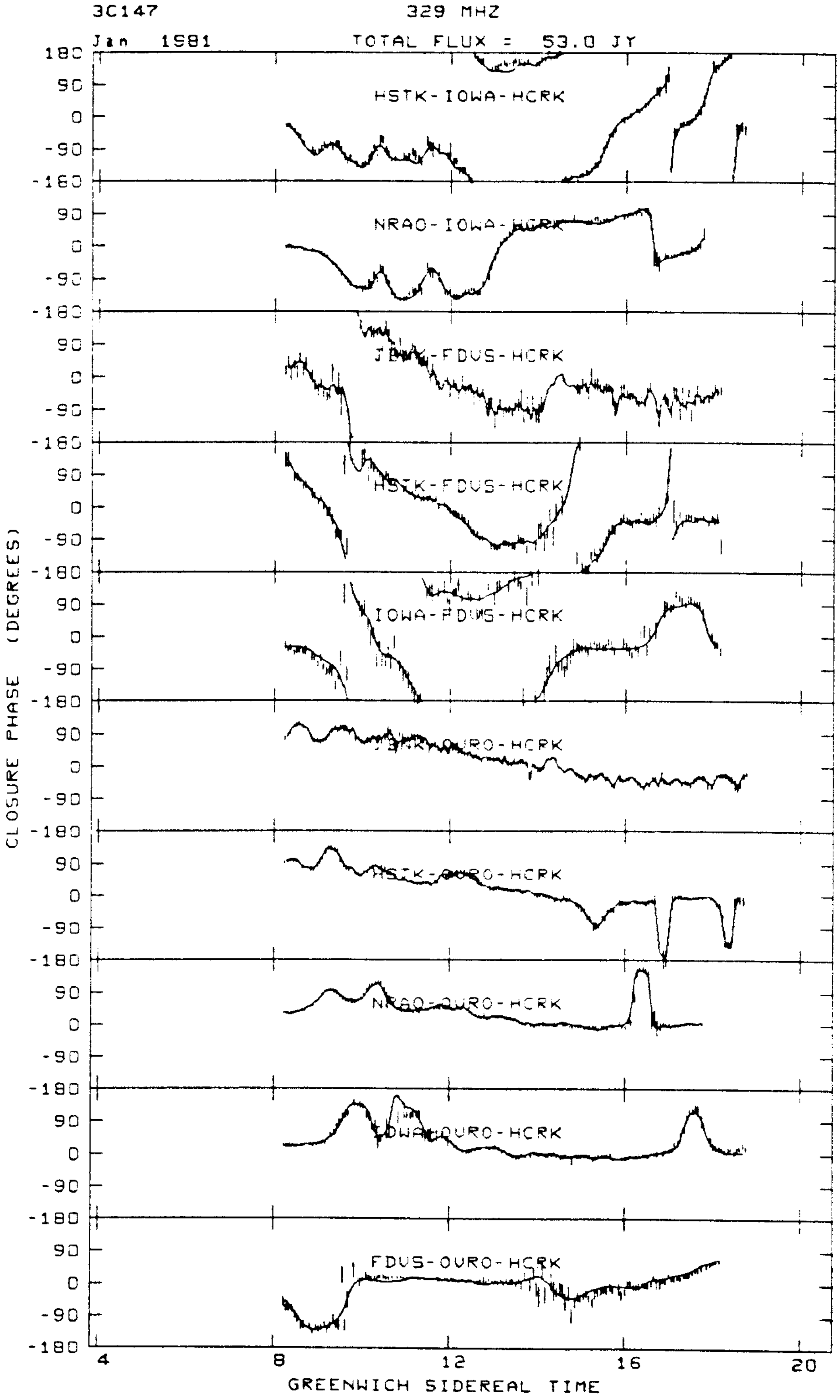

Figure 5b (continued)

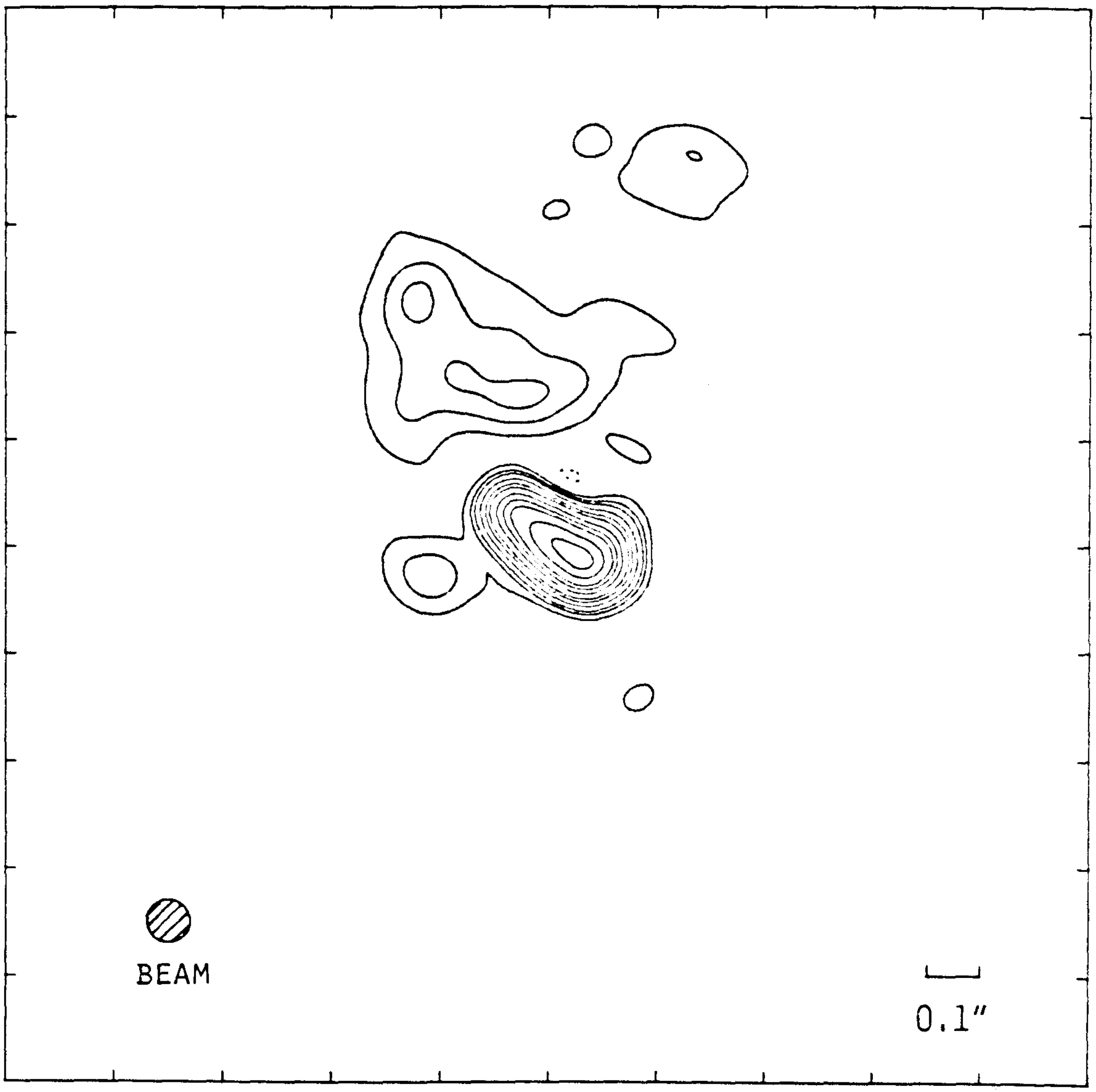

Figure 5c

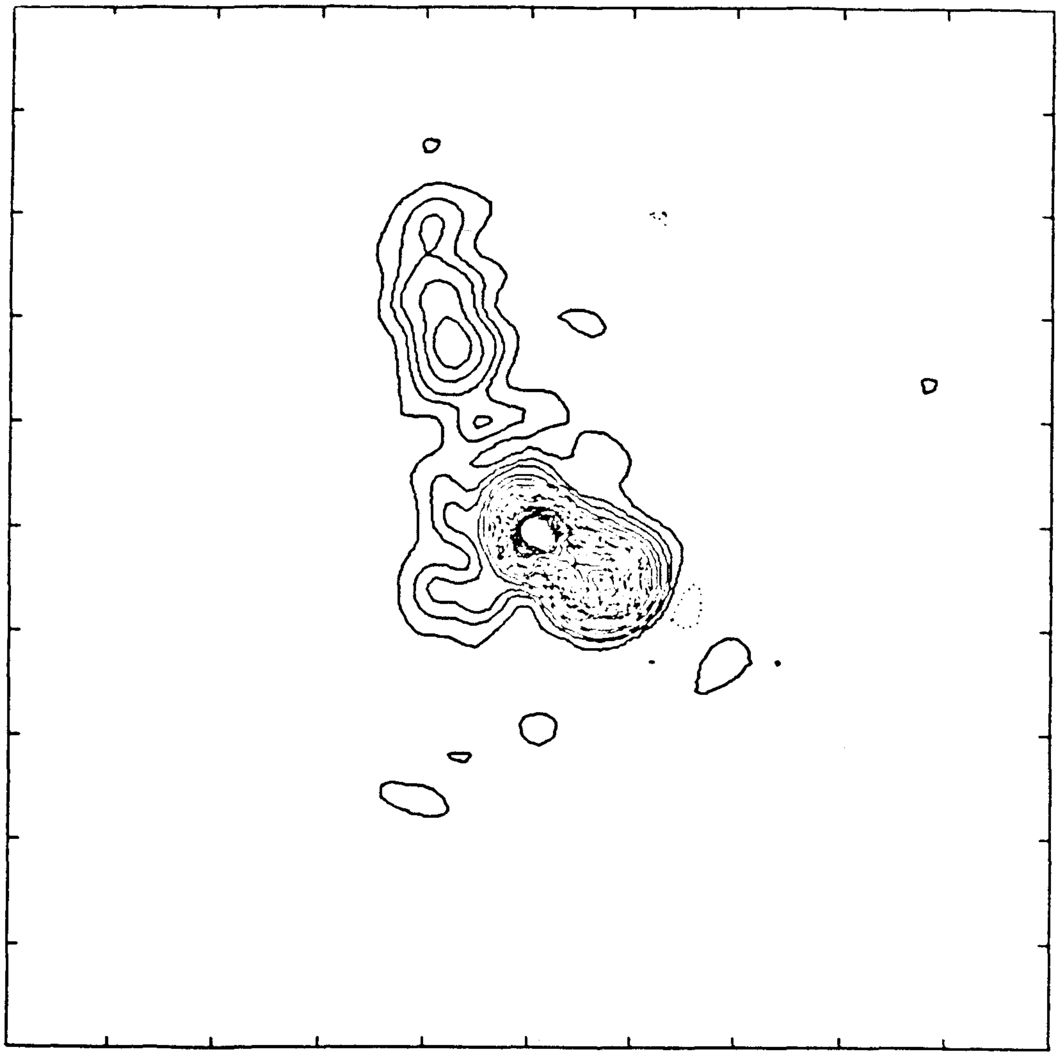

Figure 5d

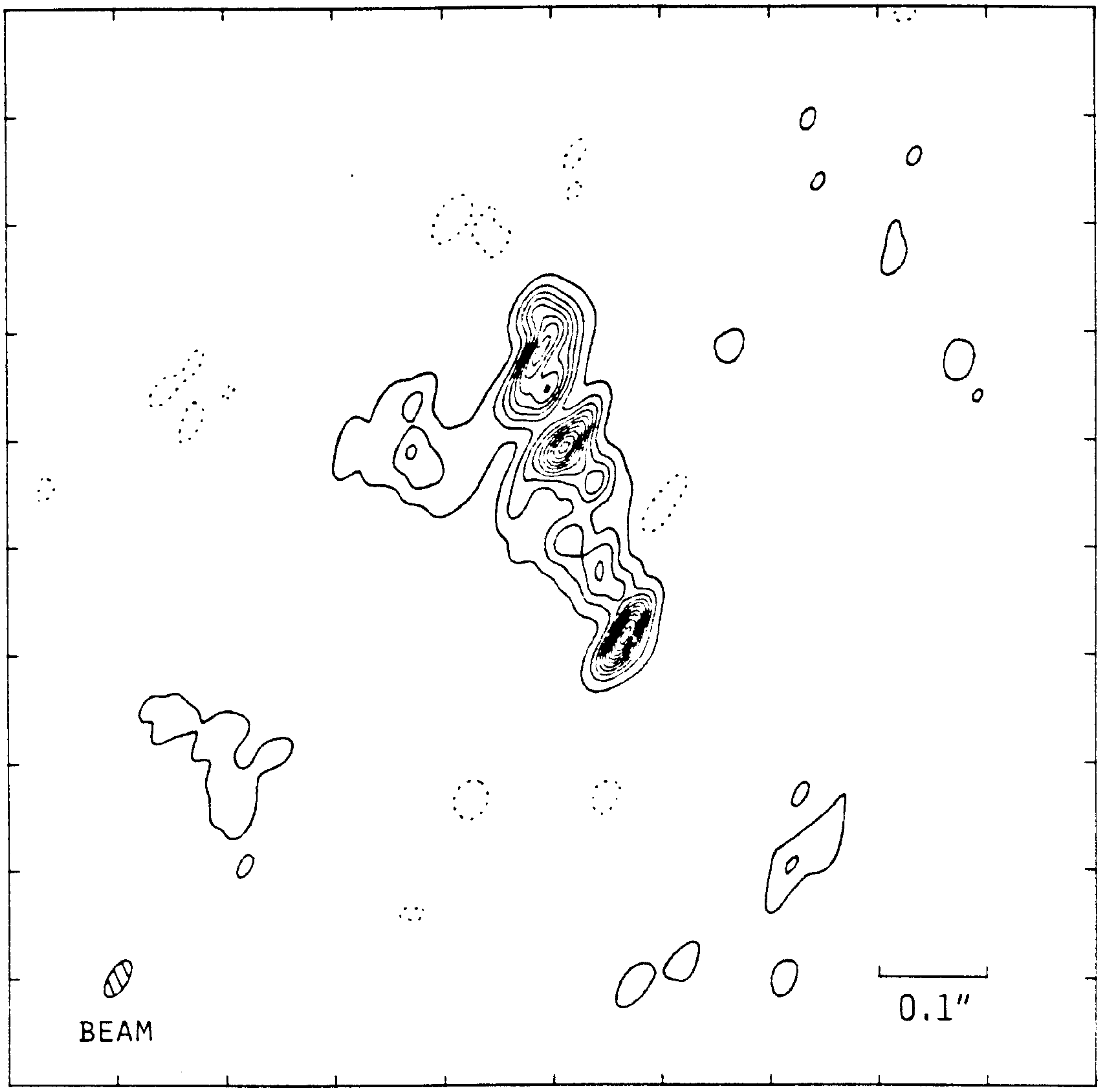

Figure 6a

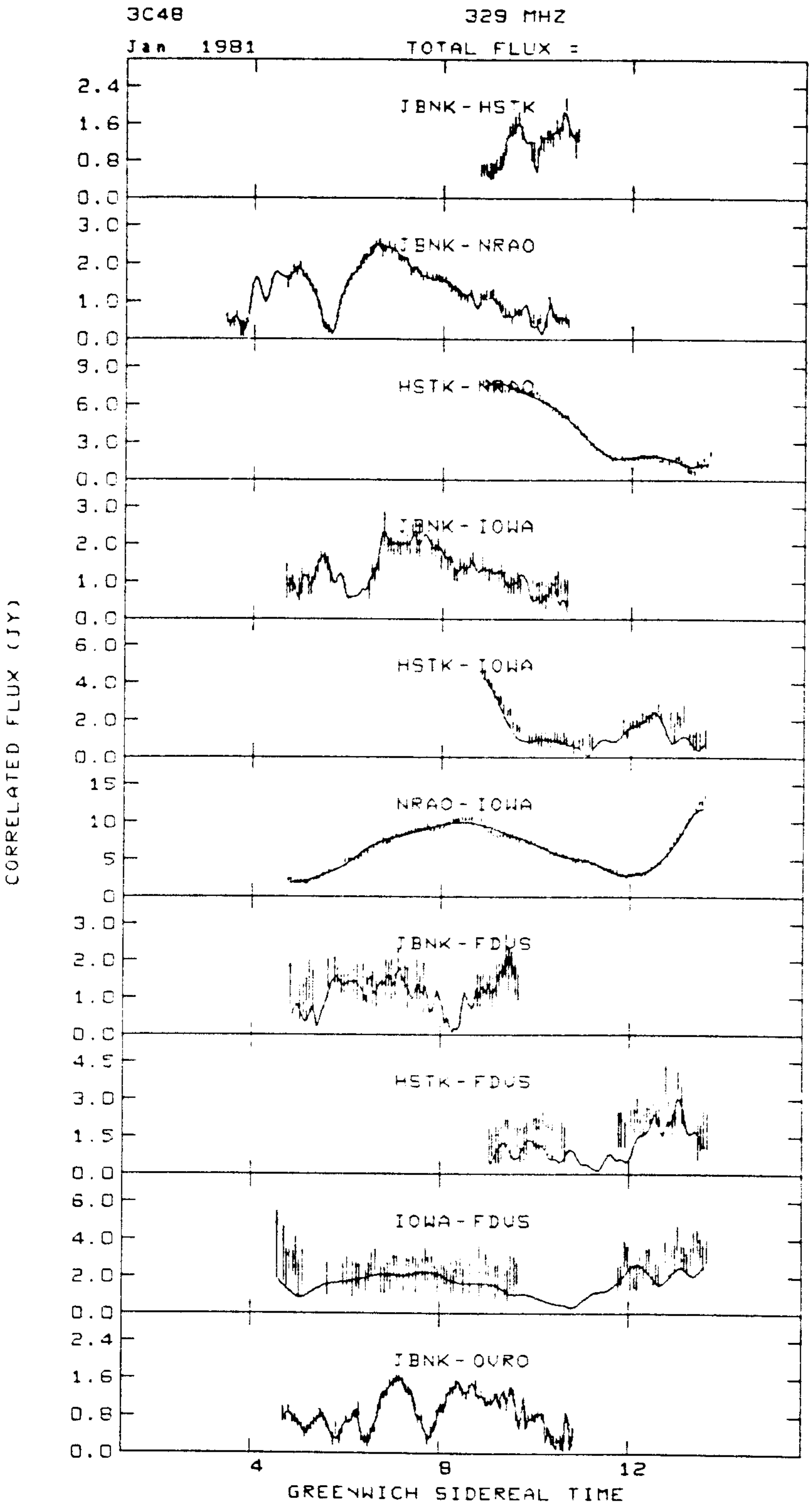
3C48
329 MHZ
Jan 1981
TOTAL FLUX =
JBNK-HSTK
2.4
1.6
0.8
0.0
JBNK-NRAO
3.0
2.0
1.0
0.0
HSTK-NRAO
9.0
6.0
3.0
0.0
JBNK-IOWA
3.0
2.0
1.0
0.0
HSTK-IOWA
6.0
4.0
2.0
0.0
NRAO-IOWA
15
10
5
0
JBNK-FDVS
3.0
2.0
1.0
0.0
HSTK-FDVS
4.5
3.0
1.5
0.0
IOWA-FDVS
6.0
4.0
2.0
0.0
JBNK-OVRO
2.4
1.6
0.8
0.0
4
8
12
GREENWICH SIDEREAL TIME
CORRELATED FLUX (JY)

Figure 6b

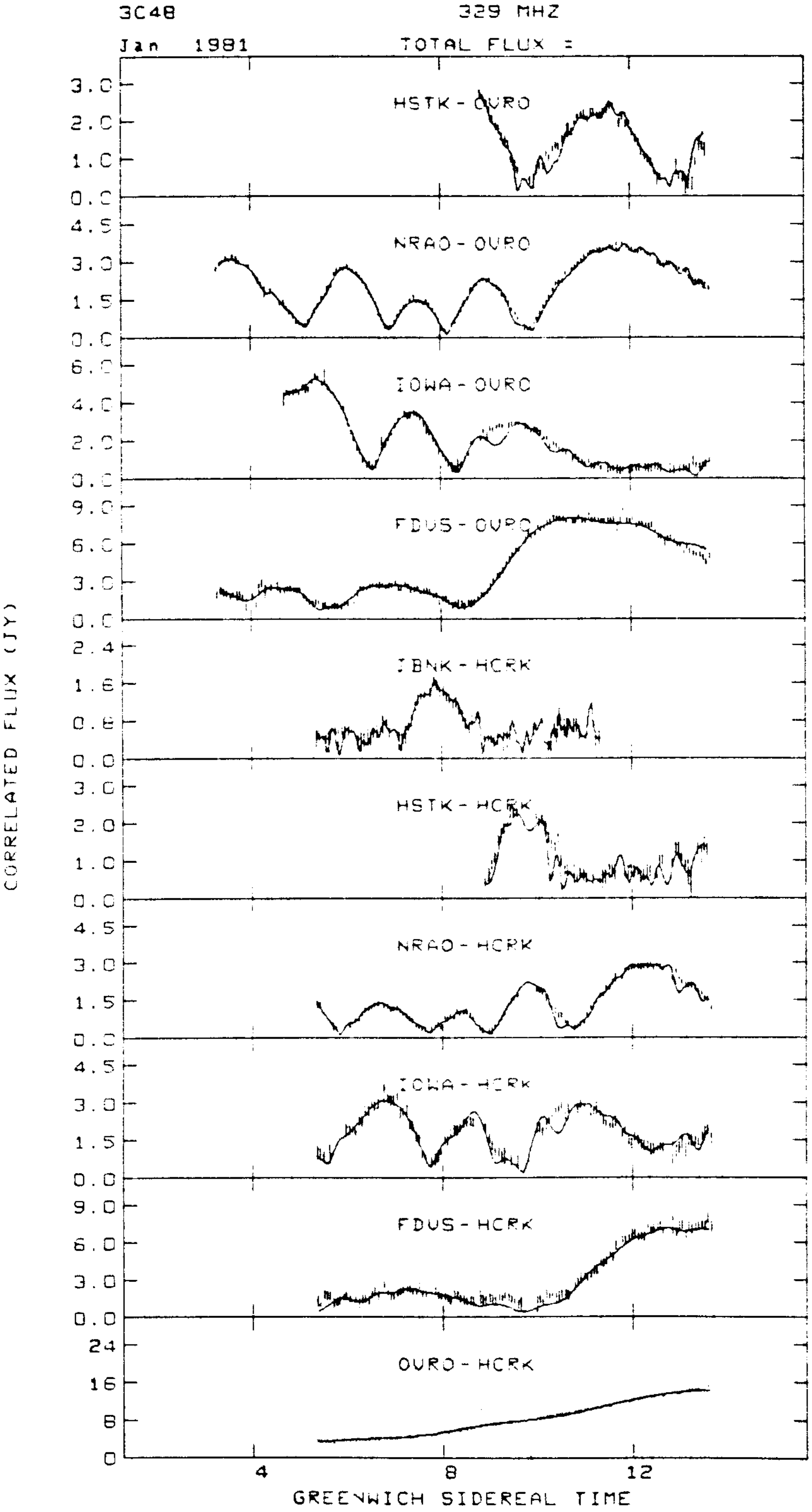

Figure 6b (continued)

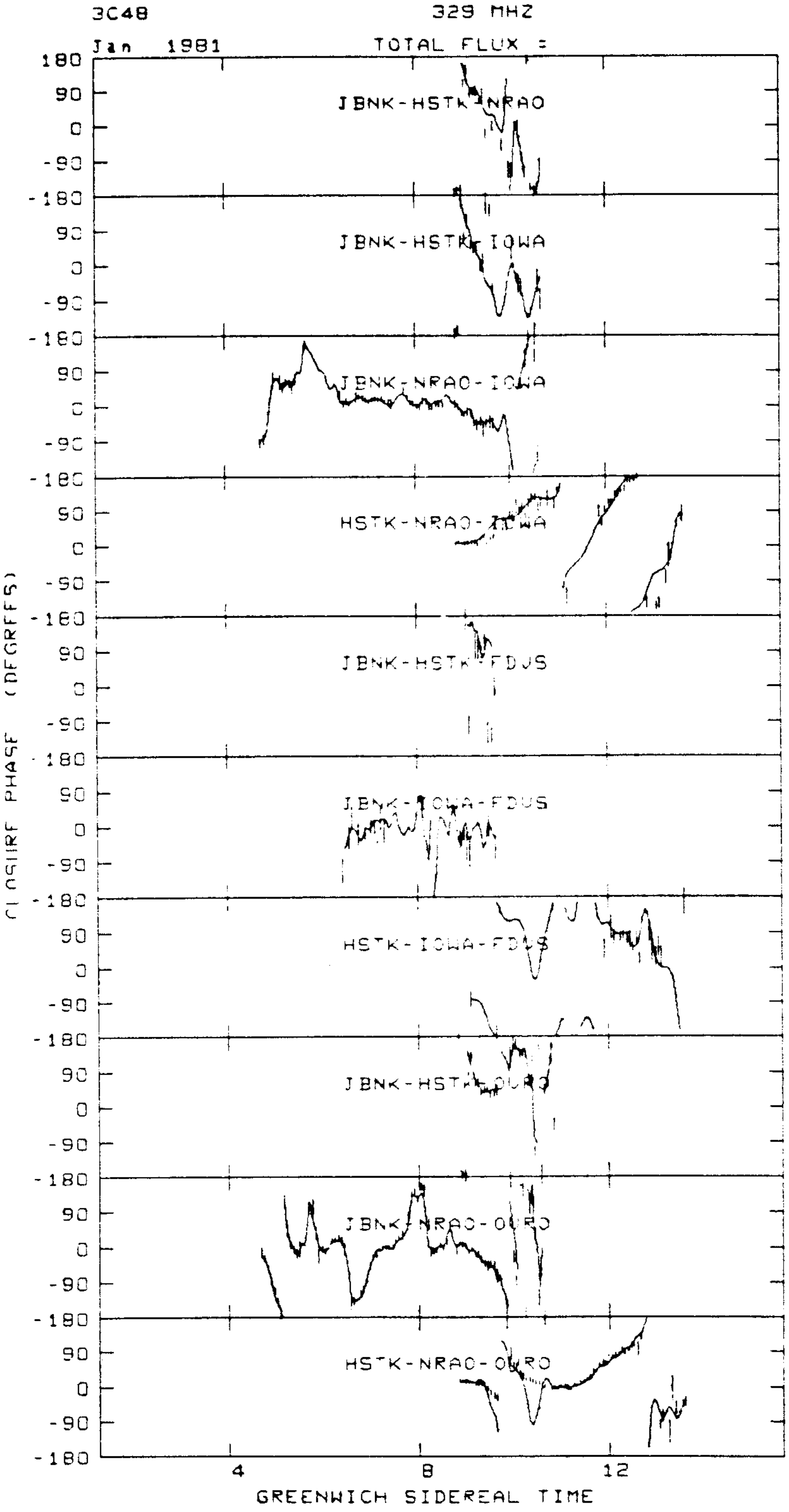

Figure 6b (continued)

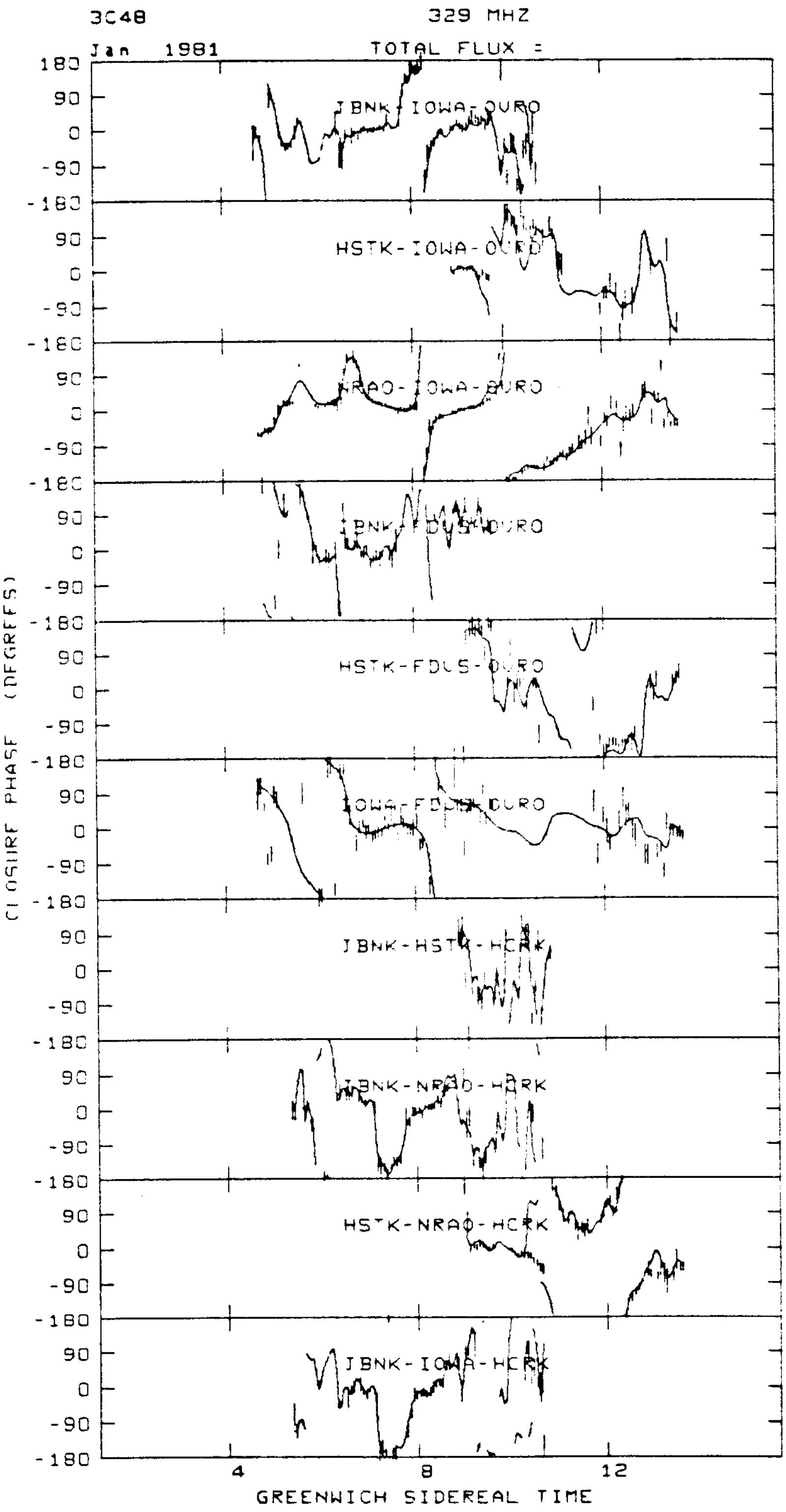

Figure 6b (continued)

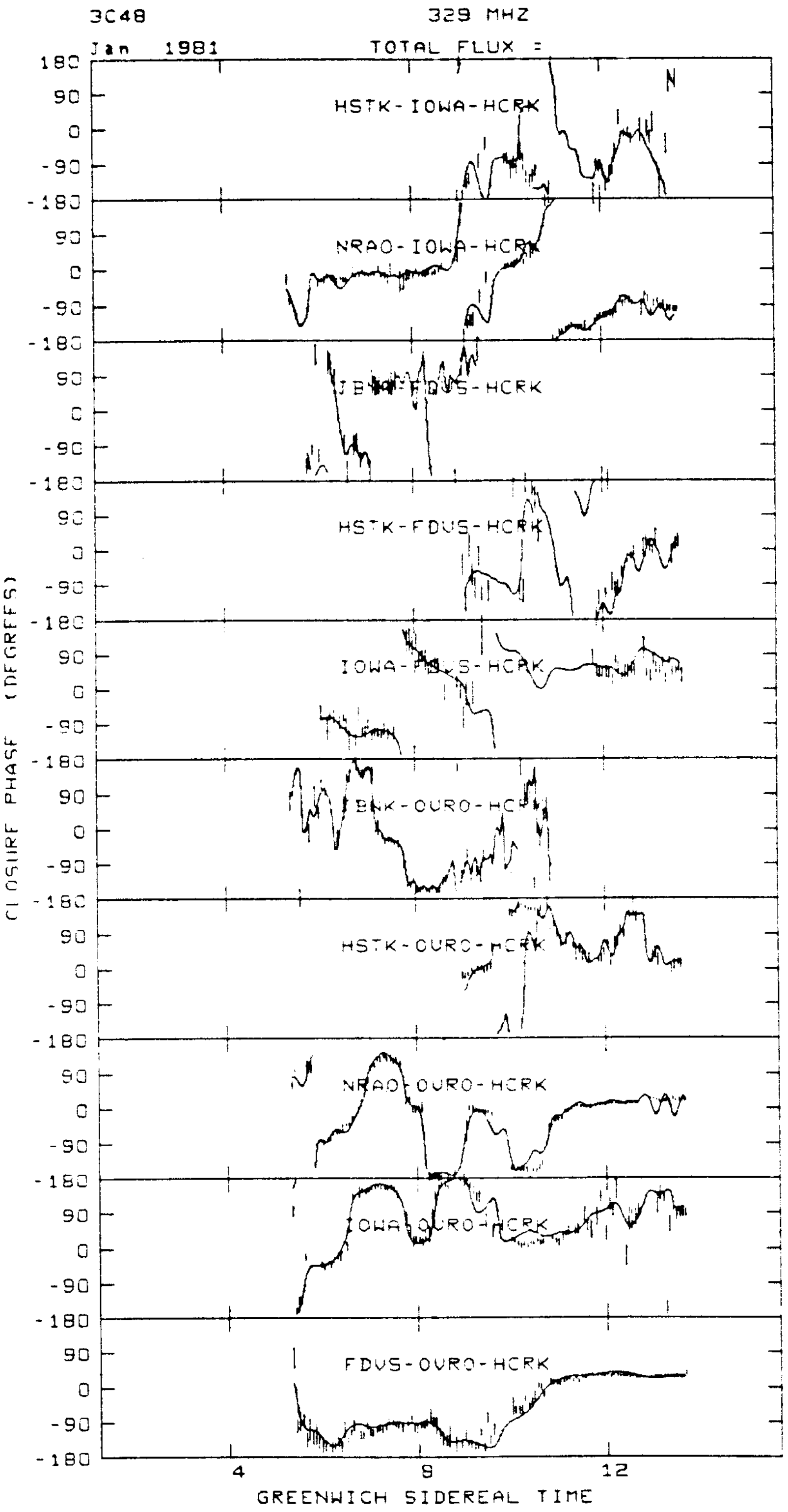

Figure 6b (continued)

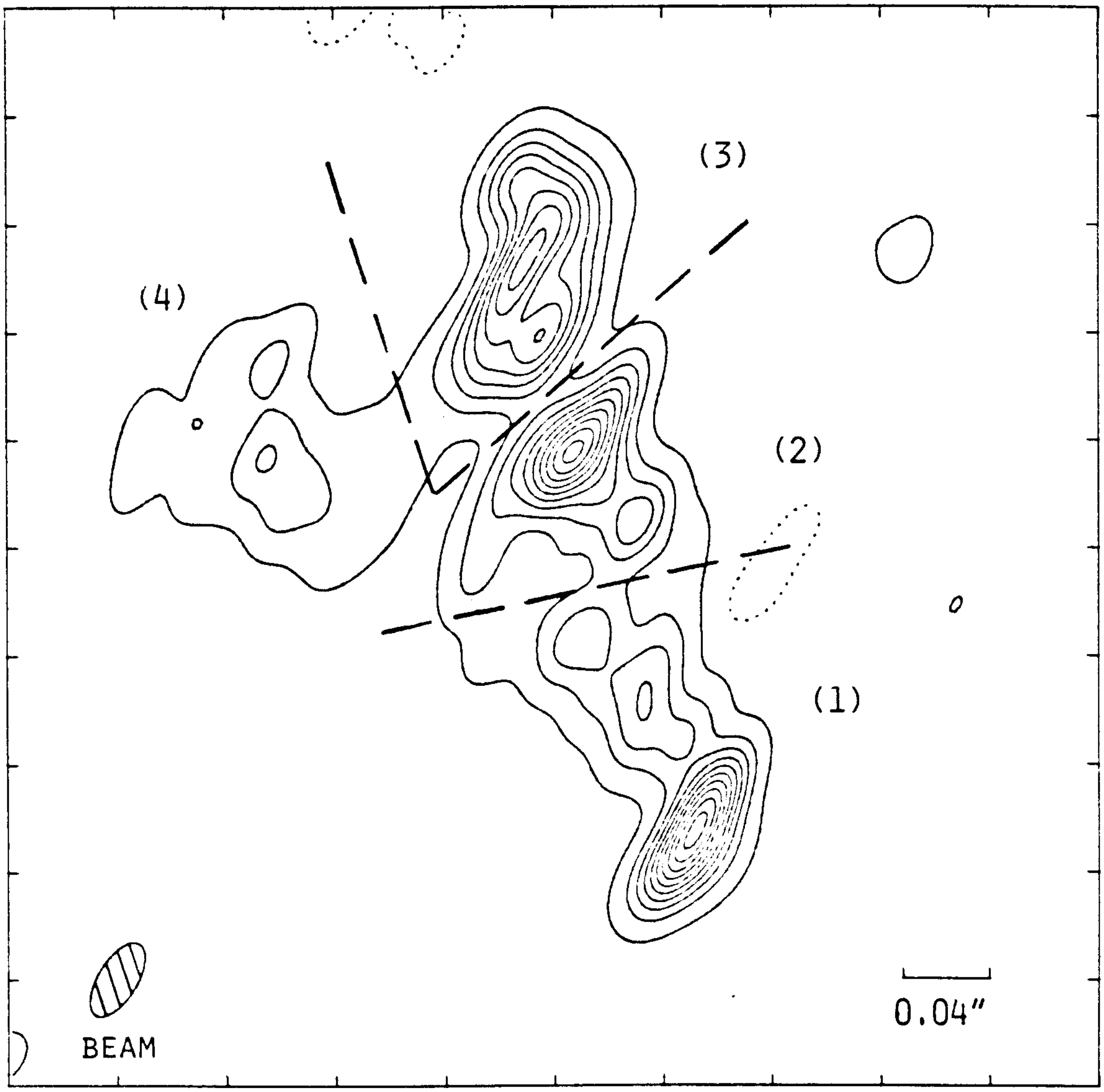

Figure 6c

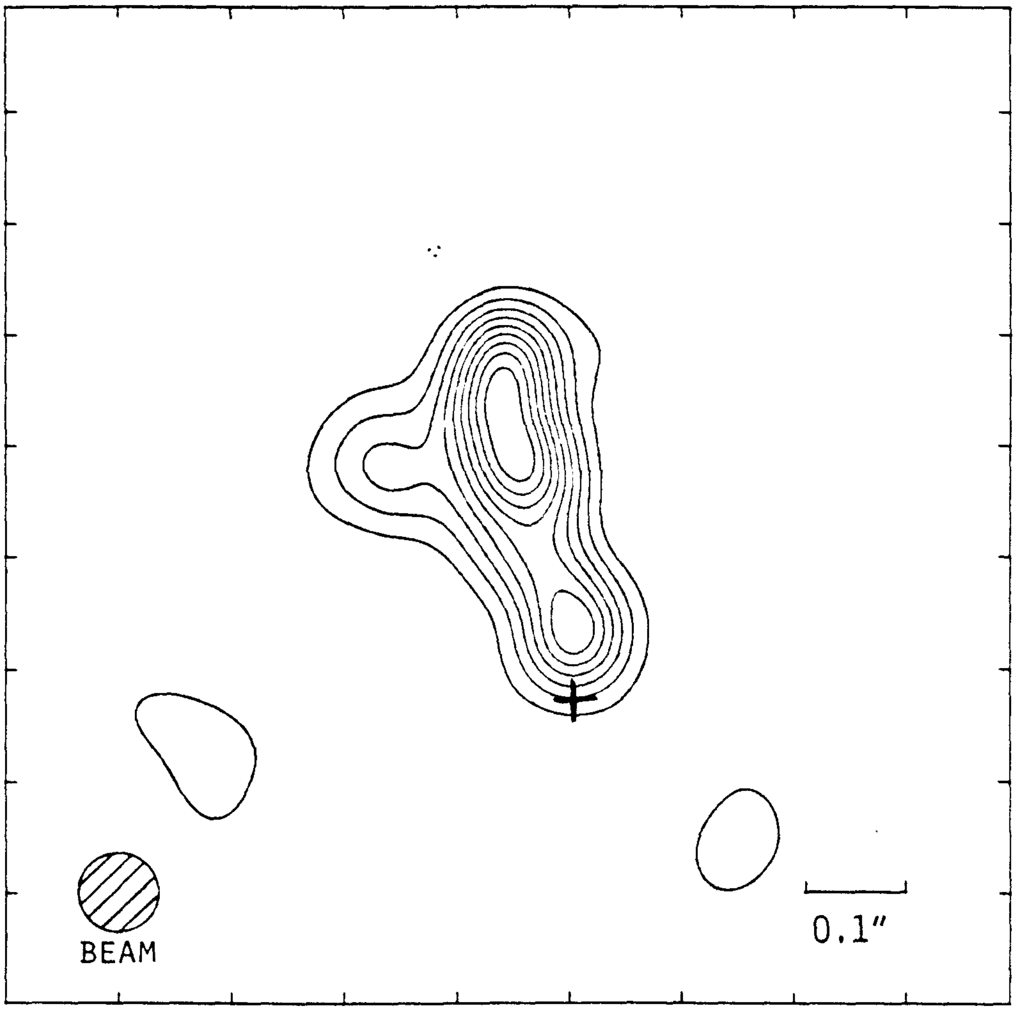

Figure 6d

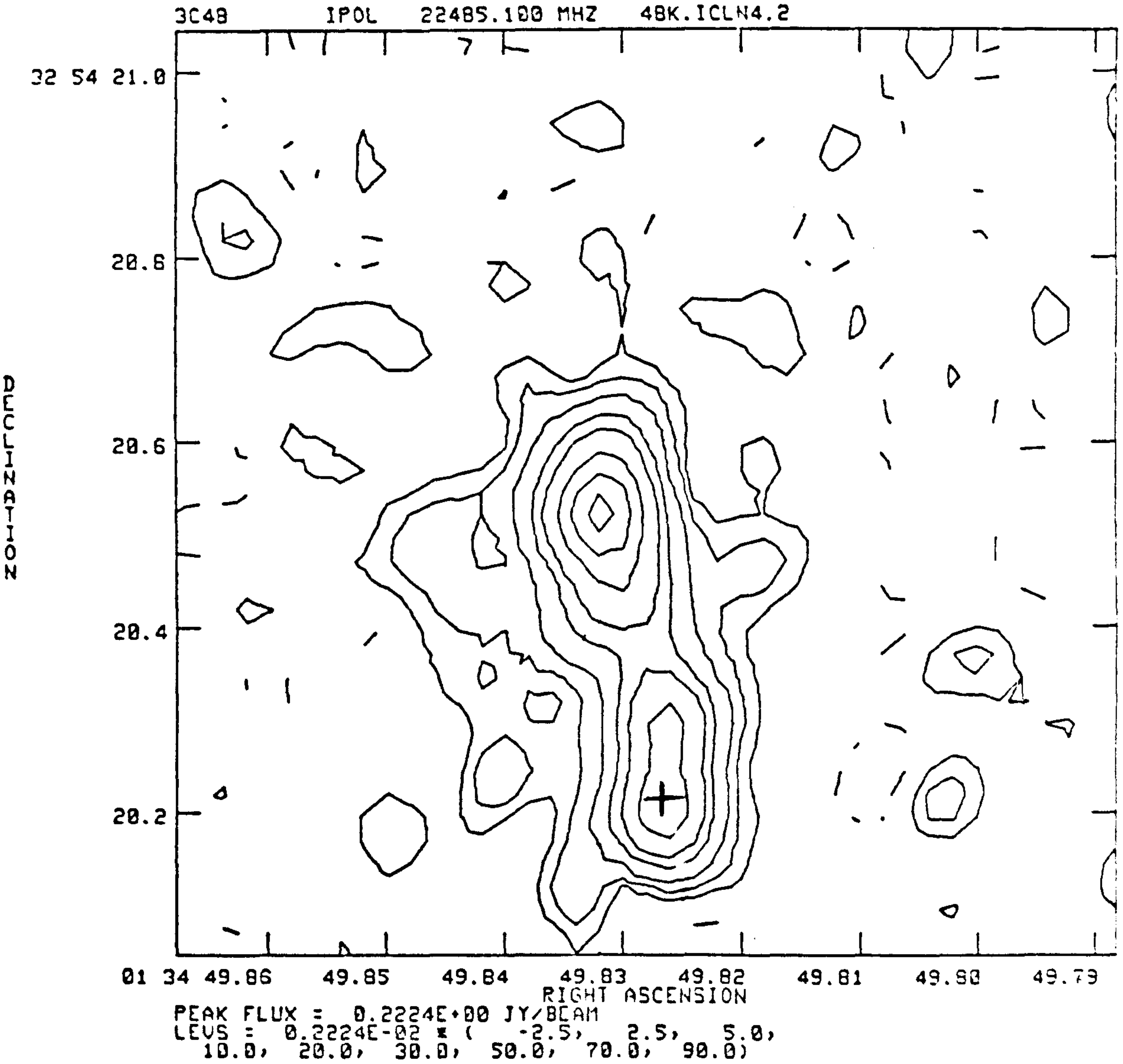
3C48 IPOL 22485.100 MHZ 48K.ICLN4.2
32 54 21.0
20.8
20.6
20.4
20.2
DECLINATION
01 34 49.86
49.85
49.84
49.83
49.82
49.81
49.80
49.79
RIGHT ASCENSION
PEAK FLUX = 0.2224E+00 JY/BEAM
LEVS = 0.2224E-02 * (-2.5, 2.5, 5.0,
10.0, 20.0, 30.0, 50.0, 70.0, 90.0)

Figure 6e

CHAPTER 3

Low-Frequency Variability and Predicted Superluminal Motion in 3C147

Submitted to: Nature

Authors: R.S. Simon, A.C.S. Readhead, A.T. Moffet,
P.N. Wilkinson, B. Allen, and B.F. Burke

Summary

VLBI observations of 3C147 reveal that the core of 3C147 is a low-frequency variable radio source which has brightened by a factor of two in six years. In combination with X-ray observations, this implies that bulk relativistic motion is taking place within the core, and leads to the prediction that 3C147 is a member of the class of "superluminal" radio sources.

Subject Headings: interferometry - quasars - radio sources: spectra - radio sources: variable - X-rays: sources

Changes in 3C147 at 329 MHz

Low-frequency variability in extragalactic radio sources poses some theoretical problems[1,2] since the time-scales involved imply brightness temperatures which exceed the inverse Compton limit[3] of 10^{12} K. One possible solution is that the radiating regions are moving towards us with a relativistic bulk speed, but this may lead to very large values of total energy, or require special source geometry[2,4]. We report here the first direct observations of component variability in an extragalactic radio source at low frequency. An analysis of the radio and X-ray observations reveals that at least part of the radio emission region must be moving towards us relativistically with a Doppler factor $\delta \gtrsim 6$.

We have observed the quasar 3C147 (0538+49, $z = 0.545$) using Very Long Baseline Interferometry (VLBI) at 329 MHz at two different epochs. The first observations were made in March, 1975 using a three station interferometer consisting of Jodrell Bank, Cheshire, UK (JBNK); Green Bank W.V., USA (NRAO)*; and Big Pine, Ca., USA (OVRO). These observations have been discussed elsewhere[5]. In February, 1981,

---

* The National Radio Astronomy Observatory is operated by Associated Universities Inc., under contract to the National Science Foundation.

we re-observed 3C147 with a seven station interferometer including the above three stations and four additional stations in the US: Haystack, Ma.; North Liberty, Iowa; Fort Davis, Tx.; and Hat Creek, Ca. A full discussion of the details of this second observation is in preparation[6]. Hybrid maps[7] made from the two data sets are shown in Figure 1. The 1981 map has been convolved with the beam appropriate to the 1975 map, and both maps have the same absolute contour levels in order that they may be compared directly. Each map can be described roughly as an unresolved core with a partially resolved jet consisting of two knots extending to the SW. Due to the very low dynamic range of the 1975 map, only the positions and the relative brightnesses of the three components are well determined[5]. The shapes of the components in the 1975 map are poorly defined and in particular, the width of the jet is not strongly constrained. In contrast, the 1981 map is very reliable with a dynamic range exceeding 25:1.

Comparisons between the two maps reveal that the barely resolved core has increased in flux density by a factor of about 2 in the six years between observations, from 0.9 Jy in 1975 to 2.0 Jy in 1981. This is the first direct observation of a change in the flux of a component of an extragalactic radio source below a frequency of 2 GHz, as well as the first positive detection of low-frequency variability in 3C147. While Fischer and Erickson[8] found 3C147 to "show evidence" of variability below 1 GHz, Fanti _et al._[9] failed to detect 3C147 as a low-frequency variable, with an upper limit to any variations at 408

MHz of ~ 5% of the total flux.

Readhead et al.[10] first pointed out that there is an advantage in using VLBI to study low frequency variability, since the visibility on the largest baseline would be sensitive only to the most compact, and presumably varying, structure. In the present case the advantage of VLBI over single dish observations is clear, since the observed flux density increase of 1 Jy amounts to only 2% of the total source intensity, but corresponds to a factor of 3 increase in the correlated flux density on the longest baseline (JBNK-OVRO).

Despite their use of VLBI, Readhead et al. detected no appreciable variation in structure in 3C147 between December 1973 and March 1975 at 609 MHz, and succeeding observations at this frequency have been marred by repeated failures at one or more telescopes. Their failure to detect variation interferometrically is possibly due to three factors. First, the long time constant of the variation requires observations spaced by several years. Second, a reduction in the amplitude of variability at higher frequencies is implied, with the spectral index of the variable component ~ 1 (the flux density S_f at frequency f is related to the spectral index α by $S_f \propto f^{-\alpha}$). This is consistent with an observed property of other low-frequency variables, namely, the amplitude of variability decreases as the observing frequency increases[11]. Finally, variability in the core may occur intermittently.

The evidence for variability in the source can be seen directly in the closure phase data. In Figure 2 is shown part of the closure phase measured for the triangle JBNK-NRAO-OVRO for both 1975 and 1981. Since the closure phase is free of both calibration and systematic errors (to approximately the 2 degree level), the large differences between the two data sets (up to ~ 50 degrees) imply significant changes in the source structure. At 16.2 hours GST the closure phase for both observations undergoes a large phase jump, corresponding to a deep minimum in the visibility amplitude on the baseline NRAO-OVRO. The 1981 data undergo the larger phase change because the amplitude minimum was deeper in 1981 than in 1975. This was caused by the stronger beating (in 1981 as compared to 1975) of the core against the knot at the end of the jet, due to the increased flux density of the core. Detailed modeling[6] indicates that the core has increased in brightness by a factor of 2.2 ± 0.2.

In addition to the low frequency variability, the 10.6 GHz flux density has been slowly decreasing over the past decade[12], which is a further indication of activity within the source.

Relativistic Bulk Motion

The direct evidence for relativistic bulk motion comes from a comparison of the predicted inverse Compton X-ray emission with the observed emission, and the assumption that the observed X-ray flux density is an upper limit to the inverse Compton X-ray flux density. Marscher and Broderick were the first to apply this method of analysis in detail[13,14], and successfully predicted superluminal motion in the quasar NRAO 140[15]. In order to perform the analysis and make this comparison it is first necessary to determine the spectrum shape and the size of the radio emitting region.

Readhead and Wilkinson[16] made a hybrid map of 3C147 at 1671 MHz in September 1976. Combining this map with those at 329 MHz[5] and 609 MHz[17] from March 1975, the 2.3 GHz map of Phillips and Shaffer[18], and including more limited data at 2.7 GHz, 15 GHz, and 86 GHz (see Simon et al.[5] and references therein) enables us to determine the spectrum of the core (see Figure 3). Note that the 86 GHz core flux density is based on the total flux density minus the flux density extrapolated for the jet. The observations of the core show that it is optically thick at 329 MHz and that the spectrum has a maximum between 609 MHz and 1671 MHz. We have fitted the spectrum to that of a spherical, homogeneous, self-absorbed synchrotron source. Such a spectrum is completely specified by three parameters: α, the high-frequency (optically thin) spectral index; and f_m and S_m, the frequency and flux density, respectively, at the maximum in the spectrum. Note that we define S_m as the flux density at f_m extrapolated from the optically thin spectrum. For the core of 3C147, we find that $\alpha = 0.45$, $f_m = 0.8$ GHz, and $S_m = 4.7$ Jy (the actual peak flux density is 4.0 Jy). The estimated errors for these parameters are ~ 10%, and do not significantly affect the calculations which follow. Furthermore, these three parameters are not independent; in the calculations below, an error in the determination of one of these parameters will be partially compensated by changes in the values of the other parameters (see Figure 3, and equation(1); equation(1) is insensitive to α, while S_m and f_m are roughly proportional and vary monotonically with α).

The observed Einstein X-ray flux[19] of 3C147 in the .27-3.28 keV band is 2.9×10^{-13} erg s^{-1} cm^{-2}. After correction for galactic absorption this corresponds to an X-ray flux density of 6.5×10^{-8} Jy at 1.29 keV. Rather than directly comparing the observed X-ray flux S_x to the predicted inverse Compton X-ray flux as a function of the equivalent Doppler factor δ, it is more convenient to express δ in terms of observable source parameters. δ is defined as $\delta = [\gamma(1-\beta\cos\phi)]^{-1}$, where γ is the Lorentz factor ($\gamma = (1-\beta^2)^{-1/2}$), β is the bulk velocity in units of c, and ϕ is the angle between the direction of motion and the line of sight. We have followed the standard procedures[20] for calculating the inverse Compton X-ray emission for the radio emitting region. For an assumed uniform, spherical, synchrotron source, the following relationship applies[21,22] between the Doppler factor, δ, the angular diameter of the core in m arc s, Θ, the X-ray flux density in Jy at 1.3 keV, S_x, the turnover frequency for the core spectrum in GHz, f_m, and the extrapolated peak flux density in Jy, S_m:

$$\text{For } \alpha = 0.45, \qquad \delta \gtrsim 0.29\ \Theta^{-1.59}\ S_x^{-.20}\ S_m\ f_m^{-1.30}\ . \qquad (1)$$

The above is for a redshift z = 0.545, as is appropriate for 3C147, and assumes that the optically thin spectrum is straight to a frequency $f_2 \sim 100$ GHz. Substituting the parameters for the radio spectrum and the observed X-ray flux yields the following relationship for the Doppler factor, which depends only upon the angular diameter θ in m arc s:

$$\delta \gtrsim 29\,\theta^{-1.59} \quad . \tag{2}$$

This relationship is independent of distance, but does depend upon our assumptions of simplified source geometry and negligible absorption of the inverse Compton X-rays.

We can therefore get an estimate of δ that requires no assumptions about the distance to 3C147, given a measurement of the angular diameter of the core. If the overall angular size of the core is used for θ (~ 5 m arc s), $\delta \gtrsim 2.2$. Unfortunately, the core of 3C147 is complex, so that equation (2) will only yield a lower limit to δ. In fact, the core consists of at least two components[16,23], with angular sizes of $\lesssim 2.5$ and ~ 3.5 m arc s. Thus, 5 m arc s is an over-estimate of the equivalent angular diameter for the core, and $\delta = 2.2$ is a strong lower limit to the Doppler factor. Since the individual spectra of the components within the core are essentially unknown, we cannot further improve our limit to δ. However, we note that equation (2) is relatively insensitive to the high-frequency spectral index in the range $.25 < \alpha < .75$, due to the limits on the total core spectrum, so that different spectral indices for the components within the core will not significantly affect our lower limit for δ.

An additional constraint on δ and θ can be derived from the variability timescale t_v, if causality is not to be violated[21]:

$$\theta \lesssim .13 \; t_v \; \delta \; r^{-1} \; \text{m arc s} \quad , \tag{3}$$

where r is the co-moving coordinate distance in Gpc, and (following Burbidge <u>et al.</u>[2]) the variability timescale t_v at 329 MHz is defined by

$$t_v = |d(\ln S_{329})/dt|^{-1} \quad . \tag{4}$$

In the present case we have $t_v = 7.5$ years. We assume throughout that $H_0 = 60$ Km s^{-1} Mpc^{-1} and $q_0 = 0.5$; then for $z = 0.545$, $r = 2.0$ Gpc. From equations (3) and (4) we can now derive a second expression for δ which, again, depends only on θ:

$$\delta \gtrsim 2.1 \; \theta \quad . \tag{5}$$

Taken together, and allowing for errors in the measurement of parameters for the core, equations (2) and (5) imply that $\delta \gtrsim 6$ (see Fig. 4). Thus, we have demonstrated that bulk relativistic motion is occurring in the core of 3C147.

Further VLBI observations are planned (at 1.6 GHz in October, 1982) to test for bulk relativistic motion in 3C147. That this motion is likely to be "superluminal" (with $\frac{v}{c}$(apparent) > 1) can be seen from a consideration of the angle between the direction of motion and the line of sight. For $\delta > 6$, the angle to the line of sight must be

$\phi \leq 10^{\circ}$. If ϕ were distributed randomly up to this limit, the most likely observed velocity is $\frac{v}{c}$(apparent) ~ $\delta(1+z)$ (see Unwin et al.[25] for plots of δ vs $\frac{v}{c}$(apparent) for various values of γ and ϕ). Thus, with no a priori knowledge of ϕ, the most likely situation is that $\frac{v}{c}$(apparent) ~ 9; we therefore predict that 3C147 is a superluminal source.

Such a rapid expansion (separation?) of the core would be readily observable. The corresponding increase in size of ~ 1.8 m arc s in six years (for $\frac{v}{c} = 9$, $\mu \approx 0.3$ m arc s yr^{-1}) is many times the estimated error in measuring either the separation between the core components or the overall angular size of the core at 1.6 GHz. Failure to detect significant motion in the core would imply that either the dominant emission mechanism in the core is not incoherent synchrotron radiation, or that the motion is occurring nearly along the line of sight, so that $\frac{v}{c} \ll \delta(1+z)$. In the latter case, the angle to the line of sight would be $\phi \lesssim 3^{\circ}$. In either case, if proper motion in the core in six years is less than the minimum detectable (≈ 0.2 m arc s at 1.6 GHz), then $\frac{v}{c}$(apparent) $\lesssim 1$. Therefore the planned observations will be a stringent test of our prediction of superluminal motion in the core of 3C147.

A weak test of this prediction can be made, based on VLBI observations at two frequencies. In the September 1976 18cm map of Readhead and Wilkinson, the core had a partially resolved double structure with a separation between components of 2.6 m arc s. In January, 1981 it was observed with VLBI at 6 cm[23]; the core had a separation of ~ 3.6 m arc s, corresponding to a possible proper motion of $\mu \approx 0.23$ m arc s yr^{-1}. Including the time dilation correction factor due to the redshift, this implies an apparent separation velocity of $\frac{v}{c} \approx 7$. This is suggestive, but not conclusive, since the possibility exists that the different separations could have been due to strong spectral gradients across the individual components in the core, rather than motion of the components. Such a spectral gradient is suspected in the quasar 3C380[18,24], while no gradients are observed across the components in the superluminal quasar 3C345[25]; widely spaced observations at a single frequency are necessary to distinguish the two possibilities.

The Energy

In spite of the bulk relativistic motion occurring in the core of 3C147, an extreme value of the total energy is not required. From standard synchrotron formulae[2,20] we can estimate the energy densities u_e in the relativistic electrons and u_M in the magnetic field, in the rest frame of the emitting region. Due to the complex structure of the core, we shall assume $\Theta = 5$ m arc s and $\delta = 10$ as the most conservative values for these parameters consistent with the observations and with the constraints on δ and Θ. We find that $u_e \sim 4 \times 10^{-7}$ ergs cm^{-3} and $u_M \sim 2 \times 10^{-6}$ ergs cm^{-3}. The total energy of the core is then $U_T \sim 10^{54}$ ergs (about the rest mass energy of a one solar mass object) and $u_e/u_M \sim 0.2$. In addition, for the core of 3C147 the following relationship for the ratio u_e/u_M applies:

$$\frac{u_e}{u_M} \sim 8\times10^{9} \ \Theta^{-17} \ f_m^{-17} \ S_m^{8} \ \delta^{-7} \ (1+z)^{8} \ r^{-1} \quad . \qquad (6)$$

In figure 4 we have plotted the relationship between Θ and δ for three different values of u_e/u_M. We see that $u_e/u_M \sim 1$ (within ~ 2 orders of magnitude) is certainly allowed by the constraints on Θ and δ.

Therefore, within the rest frame of the radiating region the core is near equipartition of energy density between the magnetic field and the relativistic electrons (cf. Scott and Readhead[26]). In contrast, lower frequency observations[26] have shown that the large scale structure in 3C147 (~ 0.5 arcseconds, or ~ 3 kpc) is also near equipartition, but only if no bulk relativistic motion is assumed for that structure.

The total energy we have found can be compared with the total energy required for the radio core of 3C345, for which $U_T \sim 10^{56}$ ergs[25], or the even more extreme possibilities discussed by Burbidge et al[2].

Implicit in the derivation of this relatively reasonable value of the total energy is the assumption that any relativistic motion which is occurring is in the form of component motion nearly along the line of sight, and not in the form of relativistic expansion. Furthermore, we have assumed that any contribution to the total energy from non-relativistic matter swept up or entrained by the moving components of the core is negligible or, equivalently, that the motion is occurring in a channel of negligible density. This model is essentially the relativistic beaming model discussed by Readhead et al.[27] and others[28-31] to explain asymmetric core radio sources.

We see that a self-consistent picture of 3C147 as a low-frequency variable has emerged which is consistent with the available observations, yet does not require an extreme value of the total energy. The key to understanding both the rapid flux increase of the core at 329 MHz and the strength of the observed X-ray flux is the occurrence of bulk relativistic motion within the core. Together with NRAO 140 there are now two extragalactic low-frequency variable radio sources in which bulk relativistic motion has been demonstrated. Furthermore, Condon and Dennison[32] have used the lower limits to angular sizes implied by the lack of interstellar scintillation to infer that bulk relativistic motion is required in three other sources: DA 406, CTA 102, and 3C454.3. Thus it may well be that bulk relativistic motion is responsible for the required time-scales in most, if not all, low-frequency variables.

We wish to thank the US VLBI Network and the observers and technical staff of all the Network observatories involved in this work. In particular, we are extremely grateful to R. L. Mutel at North Liberty Radio Observatory who generously built an entire receiving system for these observations. We also thank R. D. Blandford and S. C. Unwin for helpful comments. This work was supported by the National Science Foundation via grant AST 79-13249 to the Owens Valley Radio Observatory.

Figure Captions

1. Hybrid maps of 3C147 at 329 MHz. In each map, the lowest contour corresponds to a brightness temperature of $3x10^9$ K, and the contour interval is $6x10^9$ K. The delta functions which compose each map have been convolved with a circular Guassian restoring beam (lower left) of 20 m arc s diameter. The arms of the L in the lower right are 40 m arc s in length.

   (a) Map from March, 1975. The core (the most north-easterly of the three components) is only slightly greater in peak brightness temperature than the two knots in the jet.

   (b) Map from February, 1981. The core is substantially brighter than it was in 1975.

2. Closure phase observations on the triangle JBNK-NRAO-OVRO at329 MHz from 1975 and 1981. The 1975 data are plotted as open circles with error bars; the 1981 data as filled circles (the 1981 data are connected with a solid line for clarity). The error bars for the 1981 data are approximately the same size as the symbol used.

3. The radio spectrum of the core of 3C147. Measurements are represented as open circles with error bars. The solid line is the best-fit of a model (in a least-squares sense) to the data. The model consists of a homogeneous, spherical,

incoherent synchrotron source.

4. Limits on the equivalent Doppler factor δ and the angular diameter Θ for the core of 3C147. The dotted line is a lower limit to Θ based on the requirement that the observed X-ray flux cannot exceed the predicted inverse Compton X-ray flux. The solid line is an upper limit to Θ based on the variability timescale observed for the core, and assuming the cosmological distance to the source. The hatched area represents the region of allowed values of δ and Θ. The three dashed lines are the curves of Θ vs δ for three different values of u_e/u_M (see text):

(a) $u_e/u_M = 0.01$ (field dominated).

(b) $u_e/u_M = 1$ (equipartition).

(c) $u_e/u_M = 100$ (particle dominated).

References:

1. Jones, T.W., and Burbidge, G.R. Ap.J. 186, 791-799 (1973).
2. Burbidge, G.R., Jones, T.W., and O'Dell, S.L. Ap.J. 193, 43-54 (1974).
3. Kellermann, K.I., and Pauliny-Toth, I.I.K. Ap.J. 155, L71-L78 (1969).
4. Blandford, R.D. and McKee, C.F. M.N.R.A.S. 180, 343-371 (1977).
5. Simon, R.S., Readhead, A.C.S., Moffet, A.T., Wilkinson, P.N., and Anderson, B. Ap.J. 236, 707-713 (1980).
6. Simon, R.S., et al. (in preparation).
7. Readhead, A.C.S., and Wilkinson, P.N. Ap.J. 223, 25-36 (1978).
8. Fischer, J.R., and Erickson, W.C. Ap.J. 242, 884-893 (1980).
9. Fanti, C., Fanti, R., Ficarra, A., Mantovani, F., Padrielli, L., and Weiler, K.W. A.A. Suppl. 45, 61-78 (1981).
10. Readhead, A.C.S., Wilkinson, P.N., and Purcell, G.H. Ap.J. 215, L13-L15 (1977).

11. Spangler, Steven R., and Cotton, William D. A.J. 86, 730-746 (1981).

12. Andrew, B.H., MacLeod, J.M., and Feldman, P.A. Astr. and Astrph. 99, 36-38 (1981).

13. Marscher, A.P. and Broderick, J.J. Ap.J. 247, L49-L52 (1981).

14. Marscher, A.P. and Broderick, J.J. Ap.J. 249, 406-414 (1981).

15. Marscher, A.P. and Broderick, J.J. I.A.U. Symposium No. 97, "Extragalactic Radio Sources", D.S. Heeschen and C.M. Wade (eds.), 359-360 (1982).

16. Readhead, A.C.S., and Wilkinson, P.N. Ap.J. 235, 11-17 (1980).

17. Wilkinson, P.N., Readhead, A.C.S., Purcell, G.H., and Anderson, B. Nature, 269, 764-768 (1977).

18. Phillips, R.B., and Shaffer, D.B. Ap.J. (submitted 1982).

19. Zamorani, G. et al. Ap.J. 245, 357-374 (1981).

20. Jones, T.W., O'Dell, S.L., and Stein, W.A. Ap.J. 192, 261-278 (1974).

21. Marscher, A.P., Marshall, F.E., Mushotsky, R.F., Dent, W.A., Balonek, T.J., and Hartman, M.F. Ap.J. 233, 498-503 (1979).

22. Marscher, A.P., Ap.J. 264 (in press, 1983).

23. Preuss, E., Alef, W., Pauliny-Toth, I., and Kellermann, K.I., I.A.U. Symposium No. 97, "Extragalactic Radio Sources", D.S. Heeschen and C.M. Wade (eds.), 289-290 (1982).

24. Pearson, T.J. and Readhead, A.C.S. Ap.J., 248, 61-81 (1981).

25. Unwin, S.C., Cohen, M.H., Pearson, T.J., Seielstad, G.A., Simon, R.S., Linfield, R.P., and Walker, R.C. Ap.J. (submitted 1982).

26. Scott, M.A. and Readhead, A.C.S. M.N.R.A.S., 180, 539-550 (1977).

27. Readhead, A.C.S., Walker, R.C., Pearson, T.J., and Cohen, M.H. Nature, 276, 768-771 (1978).

28. Scheuer, P.A.G., and Readhead, A.C.S. Nature, 277, 182-185 (1979).

29. Blandford, R.D., and Konigl, A. Ap.J., 232, 34-48 (1979).

30. Marscher, A.P. Ap.J. 239, 296-304 (1980).

31. Readhead, A.C.S., Hough, D.H., Ewing, M.S., Walker, R.C., and Romney, J.D. Ap.J. (1983, in press).

32. Condon, J.J., and Dennison, B. Ap.J., 224, 835-840 (1978).

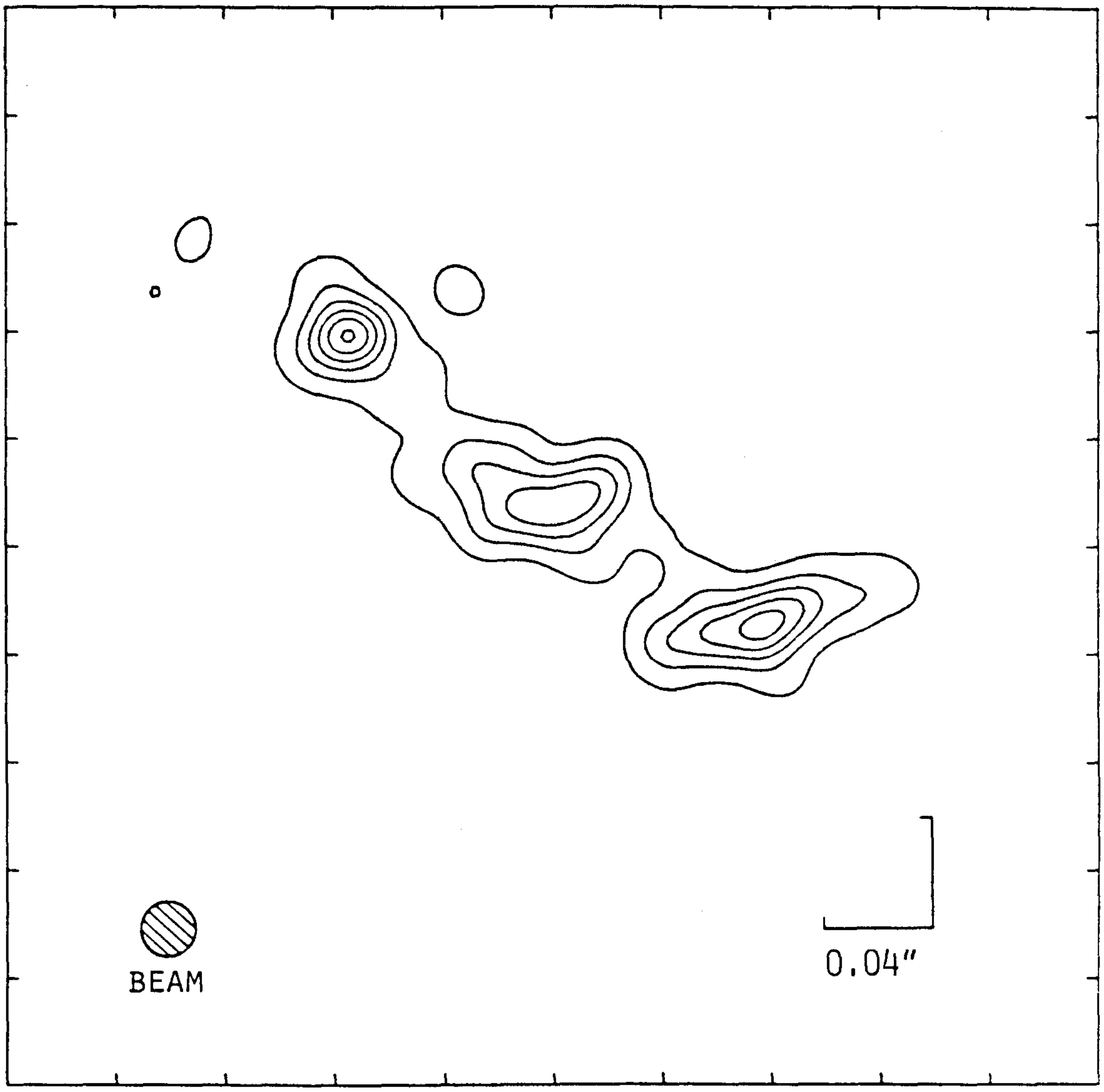

Figure 1a

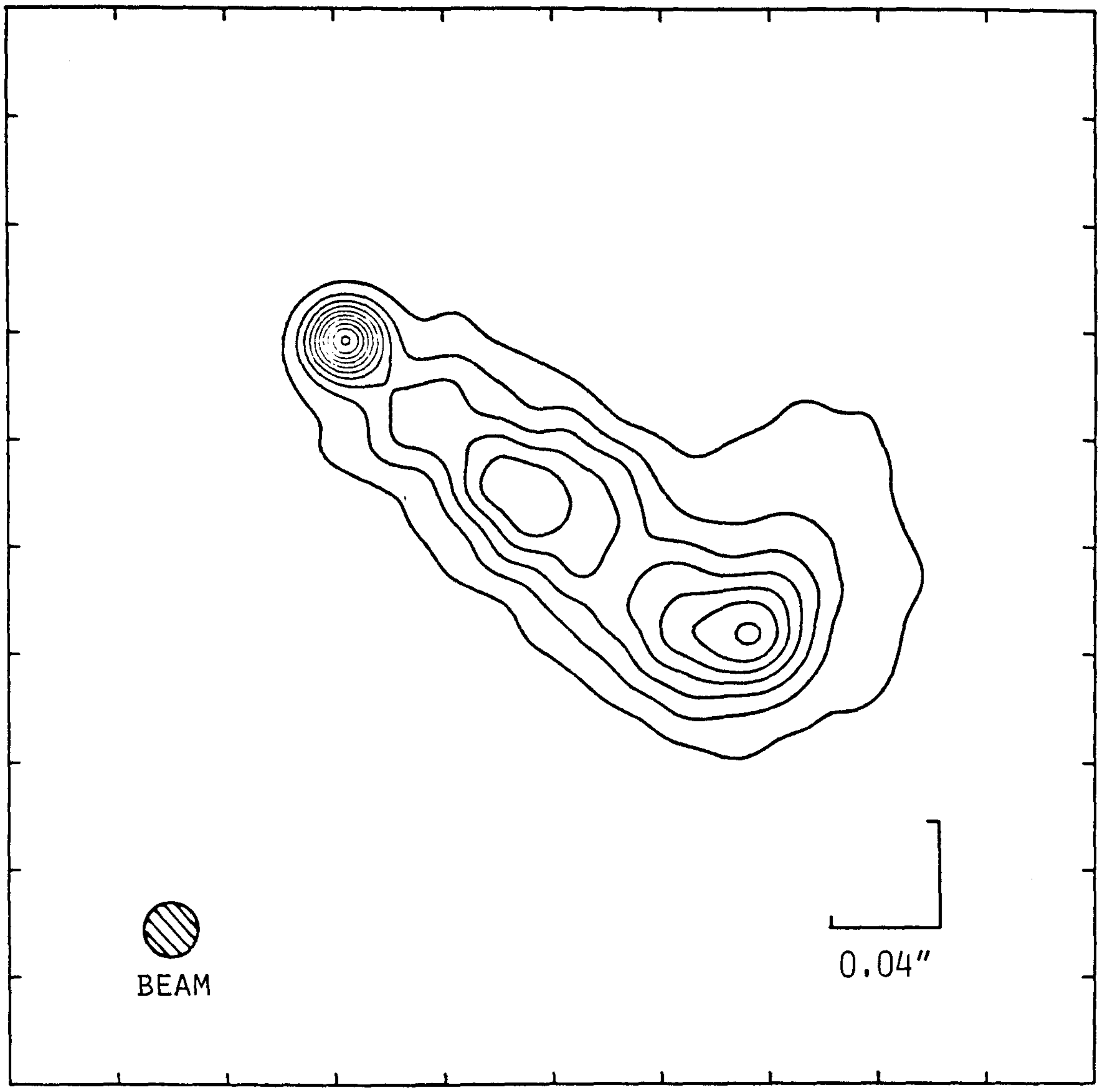

Figure 1 b

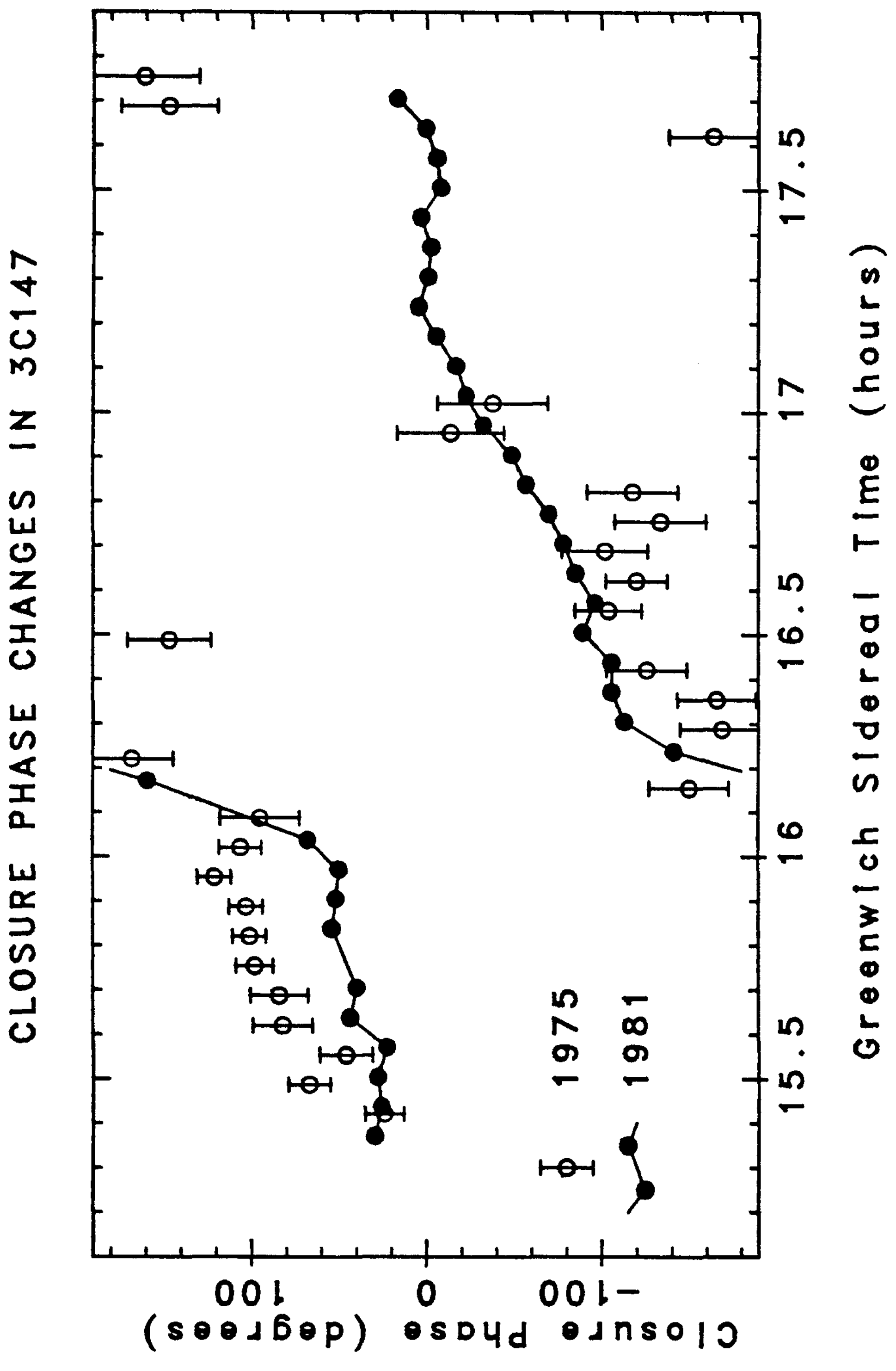
CLOSURE PHASE CHANGES IN 3C147
Greenwich Sidereal Time (hours)
15.5
16
16.5
17
17.5
Closure Phase (degrees)
100
0
-100
1975
1981

Figure 2

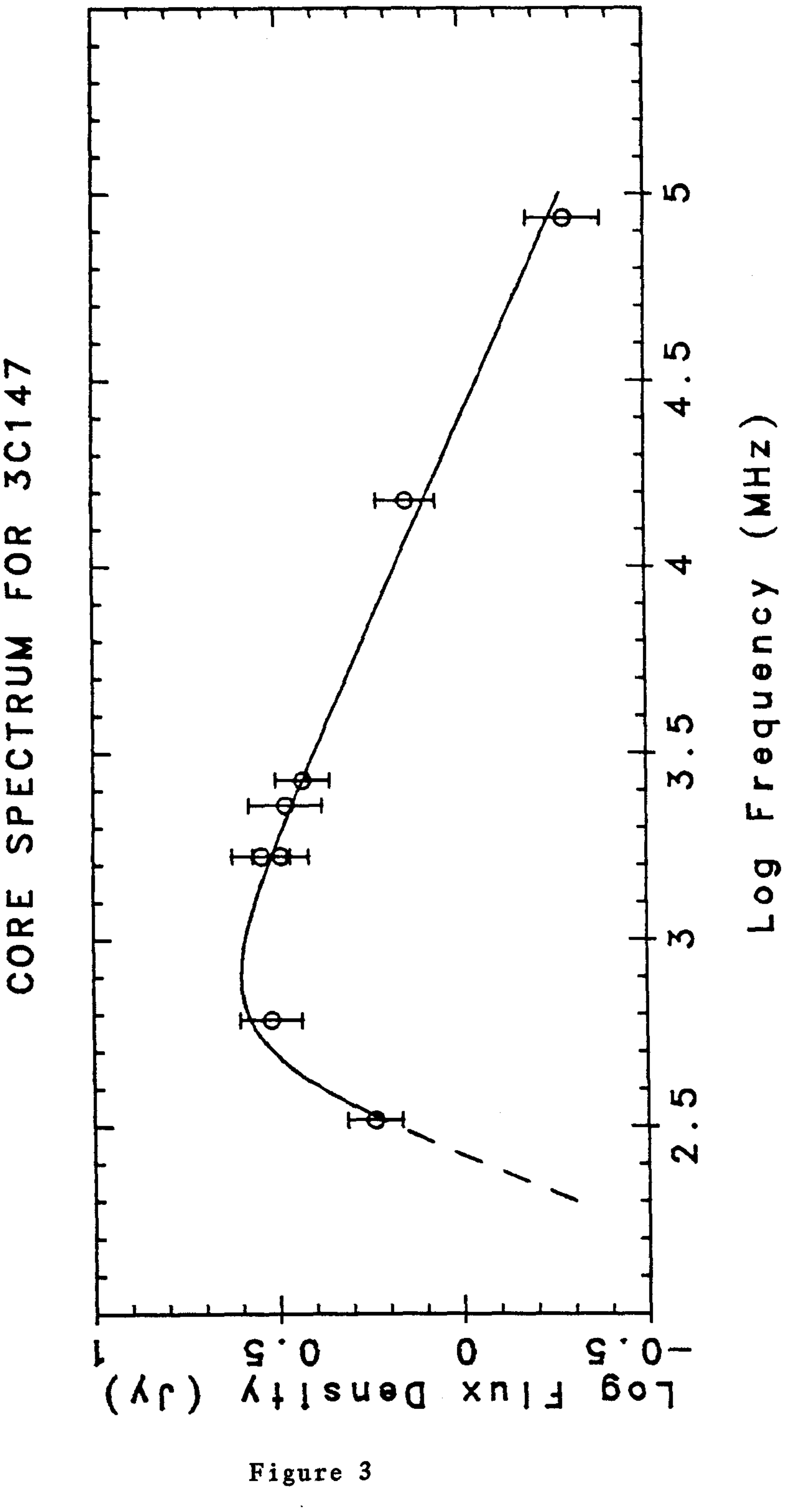
CORE SPECTRUM FOR 3C147
Log Frequency (MHz)
2.5
3
3.5
4
4.5
5
Log Flux Density (Jy)
-0.5
0
0.5
1

Figure 3

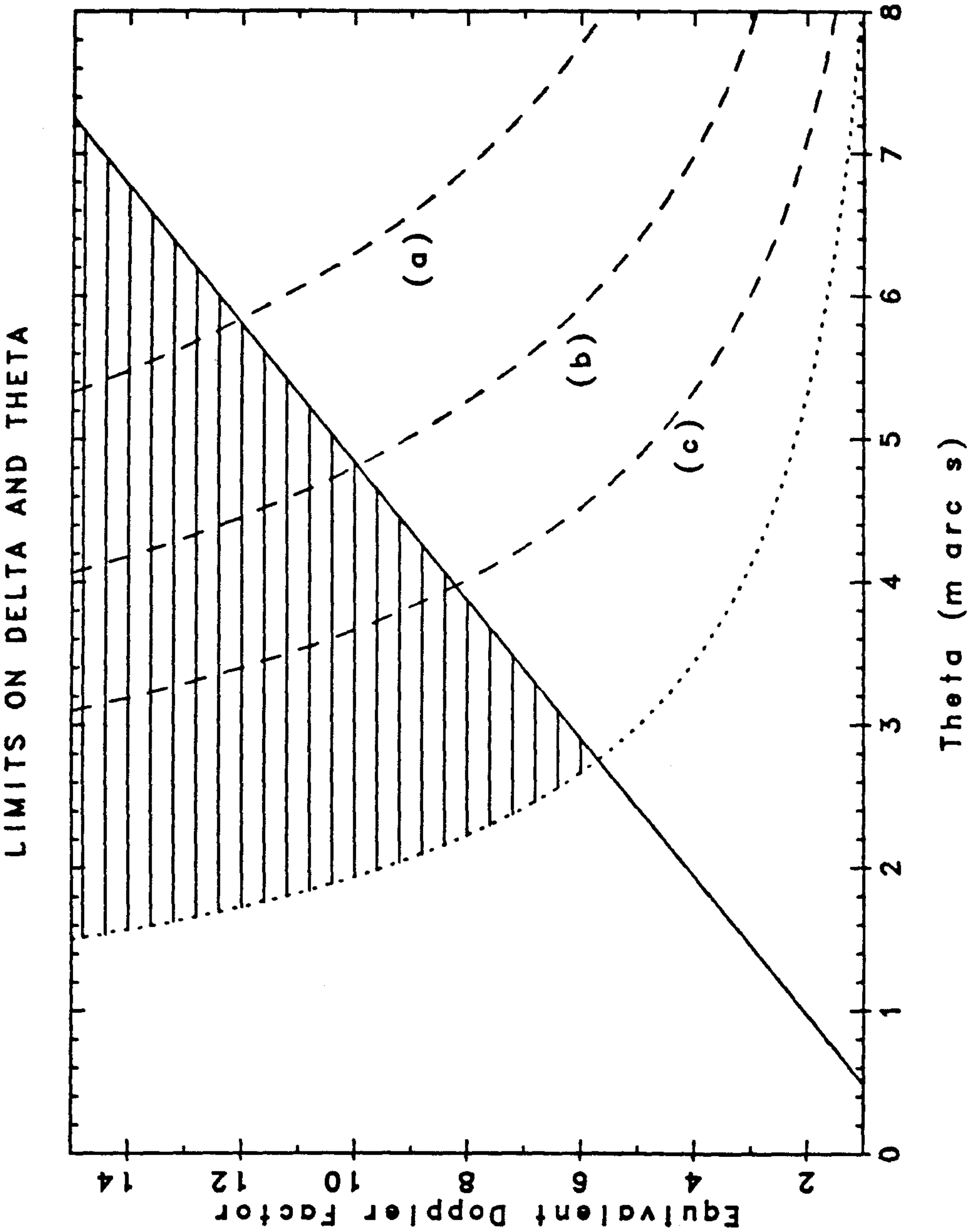
LIMITS ON DELTA AND THETA
Equivalent Doppler Factor
2
4
6
8
10
12
14
Theta (m arc s)
0
1
2
3
4
5
6
7
8
(a)
(b)
(c)

Figure 4

CHAPTER 4

Physical Implications of Compact Structure in Quasars from Low-Frequency VLBI Observations

Summary

Observations of 5 quasars (3C48, 3C147, 3C309.1, 3C380, and 3C454.3) are analyzed using standard synchrotron emission theory in order to discover the physical conditions occurring in these objects. For 3C48, the suggestion in chapter 2 of this source as a "core-jet" source is seen to be reasonable, with fields, energy density, and pressure all decreasing with increasing distance from the supposed core. The pressure in the jet in 3C48 is extremely large, implying that the jet cannot be confined by external gas pressure, unless the surrounding medium has extreme values of the temperature and density. In the case of 3C147 (which was analyzed extensively in chapter 3), the halfwidth of the observed jet implies that collimation of the jet is occurring; the jet in 3C147 is definitely not a "free" jet. For 3C309.1, the 329 MHz observations give an upper limit to the turnover frequency for synchrotron self-absorption significantly lower than that available up to now; this limit, in combination with *Einstein* X-ray observations of 3C309.1, implies that bulk relativistic motion is occurring within the core of 3C309.1. Thus, the core of 3C309.1 may be very similar to the core of 3C147, and is a candidate for being both a superluminal source and a low-frequency variable. For 3C380 and 3C454.3, the limited spectral information available allows broad limits to be put on their properties.

Subject Headings: quasars - radio sources: general - X-rays: sources

Introduction

Using the observations presented in chapter 2, it is possible to derive physical parameters for the five sources observed. Questions of interest include the physical conditions (field strengths, energy densities, overall motion) in the emission region, characteristics of the observed jets, and constraints on the collimation and confinement mechanisms which operate in the jets observed in 3C48 and 3C147.

In the analysis which follows, several assumptions have been made. The key assumption is that it is electron-synchrotron radiation which is responsible for the observed radio emission from each quasar. A related assumption is that the electron velocity vectors are distributed randomly relative to the magnetic field in the rest frame of the field so that, assuming a tangled magnetic field, the synchrotron radiation is isotropic in the rest frame of the fields and particles.

Due to differences in the available information for each source, it is convenient to discuss each separately.

I. 3C48

A. Observational Parameters

The structure of this source is extremely complex (chapter 2), but seems to afford a relatively simple interpretation: 3C48 is a core-jet source (Readhead et al., 1978) which has a strongly self-absorbed core at 329 MHz. The core is sufficently weak that it is not seen in the 329 MHz map in chapter 2, although it is relatively bright in the unpublished 22 GHz VLA map of R. A. Perley (see chapter 2). Because the core was not detected, only inferred, little more can be said about it.

In chapter 2, the compact structure in 3C48 was divided into 4 regions. This analysis will be looking at a single component in each region, as follows:

Region 1: The bright, southern-most component in the compact structure is relatively distinct from the lower-brightness jet that extends to the northeast in this region. From here on this component shall be referred to as component 1. While this component obviously does not include all the emission from region 1, it is the dominant component in that region.

Region 2: Even though the low level structure in this region is complicated, with emission extending in three directions, the dominant component is well defined; "component 2" will be used the refer to this dominant component. Again, as for component 1, the obviously related low-brightness emission in this region is not included in component 2.

Region 3: As seen in chapter 2, the emission in this region occurs in several components blended together to form an s-shaped structure. For the purposes of this paper, the overall emission shall be considered as coming from a single component ("component 3") whose size and shape approximates the observed emission.

Region 4: This region contains relatively low-brightness emission spread over about 0.1 arcseconds. Component 4 will be taken to include virtually all the emission in region 4, to about the 5% level on the map.

Each of the components selected is dominant in its region, and reasonably well defined. Each component is also at least partially resolved, so it is possible to derive a reliable estimate of their angular sizes. In Table 1 are listed the parameters which describe each component. These parameters were derived by measuring the full-width-half-maximum (FWHM) for each component both parallel and perpendicular to the long axis of the component, and assuming that the observed component shape was elliptical. It was then straightforward to derive an estimate of the actual shape of each component by de-convolution of the measured shape with the restoring beam. This simple-minded procedure was justified because all the components are significantly resolved in all directions, except perhaps for component 1, where the halfwidth of the observed shape is only ~ 20% wider than the beam.

In the cases of components 1 and 2, the underlying components were sufficently small that it was possible to assume that the long axes of those components were parallel to the beam. In region 3, the emission is extended enough so that the actual position angle could be estimated. For region 4, the emission is so extended that the broadening due to the convolution with the beam is insignificant, and could be neglected. Because of the ill-defined shape of component 4, only an estimate of the diameter was derived. The derived major and minor axes for each component after deconvolution are listed in Table 1. Also listed in Table 1 are the observed peak brightnesses and flux densities of the (assumed) elliptical-shaped, gaussian-tapered blob which describes each component.

It should be emphasized that the angular sizes derived in this way are reliable, since the observed structure was unmistakably resolved. In order to deal with these components in a convenient form, an equivalent gaussian diameter θ_g equal to the geometric mean of the axes was assigned to each component (see Table 1). Finally, since the formulae involving the angular sizes that will be used all involve the equivalent diameter of the emitting component, a final correction factor of 1.8, appropriate for a partially-resolved, optically thin component (see Marscher, 1983), was applied to convert the equivalent gaussian diameter θ_g into the equivalent angular size, θ. θ, also tabulated in Table 1, is what will be meant by the angular diameter of a given component. This angular diameter is the diameter of the optically-thin sphere which represents each component; it is also a reasonable estimate of the overall angular diameter observed on the map for each component. The angular sizes derived in this way are estimated to have no more than a 20% error. A more formal procedure to derive angular sizes was not justified in view of the complexity of the source. Any additional precision in the measured sizes would require more assumptions concerning the underlying source structure, but would not significantly change the sizes listed in Table 1.

Individual spectra are not available for the components described above. In order to proceed, it shall therefore be assumed that the spectral index for each component is $\alpha = 0.8$ ($S \propto f^{-\alpha}$), the observed spectral index for the entire source (Veron _et_ _al_., 1974; Scott and Readhead, 1977). It will further be assumed that each of these components is optically thin at 329 MHz. The first assumption is justified by the relative constancy in the relative flux densities observed for these components between 329 MHz and 22 GHz (see chapter 2), and the smoothness of the overall spectrum. The second assumption will be seen to be justified in the calculations below.

B. Physical Conditions in the Components

Each of the components is assumed to be an optically-thin sphere radiating by means of incoherent electron-synchrotron radiation. Then, from standard synchrotron theory (Jones, O'Dell, and Stein, 1974; Burbidge, Jones, and O'Dell, 1974; Gould 1979) the following relationship can be derived between the energy density in relativistic electrons u_e, the energy density in the magnetic fields u_m, the redshift z, the co-moving coordinate distance r, an equivalent doppler factor δ, the frequency in the spectrum at which the emission is a maximum f_m, the angular diameter θ, the spectral index α ($S \propto f^{-\alpha}$), the extrapolated peak flux density S_m [following Marscher _et al_. (1979), S_m is defined as the flux density at f_m extrapolated from the optically thin (high-frequency) spectrum], and the cutoff frequency in the electron spectrum f_2:

$$\frac{u_e}{u_m} = A(\alpha) \frac{(1+z)}{r} \left[\frac{1+z}{\delta}\right]^7 S_m^8 \; \theta^{-17} \; f_m^{-17}$$

$$\times \left[1 - B(\alpha)(f_m/f_2)^{(2\alpha-1)/2}\right] . \qquad (1)$$

In the above, it is assumed that the lower cutoff to the electron spectrum corresponds to f_m, to minimize the required total energy. $A(\alpha)$ is a function that depends only upon α. For $\alpha = 0.8$, as is appropriate for the integrated spectrum of 3C48, and with r in GPc, S_m in Jy, θ in milliarcseconds, and f_m in GHz, $A(\alpha) = 3.0\text{x}10^9$. $B(\alpha)$ is the ratio of the frequency f_n at the intersection of the extrapolated optically thick and thin spectra to f_m, to the $(\alpha - 1/2)$ power. For alpha = 0.8, $B(\alpha) = 0.94$. Equation 1 depends only weakly on f_2 (in the $\alpha = 0.8$ case), so it is acceptable to assume $f_2 \approx 100$ GHz, roughly the highest observed radio frequency for this quasar (Kellermann and Pauliny-Toth, 1971). If the upper and lower limits to the electron spectrum were increased or decreased by an order of magnitude, respectively, the value of u_e/u_m would increase by less than a factor of 2. In order to apply equation 1 to the individual components in 3C48, it is useful to assume that 329 MHz is well above the individual self-absorbtion frequencies for each component, so that S_m may be expressed in terms of S_0, the observed flux density at the observing frequency f_0 (329 MHz), f_m, and α as

$$S_m = S_0 \left[\frac{f_m}{f_0} \right]^{-\alpha} . \tag{2}$$

The redshift to 3C48 is 0.367 (Smith et al., 1976). Making the assumption that $H_0 = 60$ km s^{-1} Mpc $^{-1}$ and $q_0 = 0.5$ (values to be used throughout this paper) then implies that $r = 1.4$ Gpc. Equation (1) may now be expressed in a form that is valid specifically for 3C48:

$$\frac{u_e}{u_m} = 1.9\text{x}10^7 \; S_0{}^8 \; \theta^{-17} \; f_m{}^{-23.4} \; \delta^{-7} . \tag{3}$$

It is obvious that little can be learned about u_e/u_m from the above, in the absence of more spectral information, due to the large exponents on the right-hand side of the equation. For example, if the measured angular sizes of the components are used, and the observed spectral turnover for the entire source of 70 MHz (Scott and Readhead, 1977) is assumed to be a lower bound to f_m, then un-interesting upper limits of ~10^6 for u_e/u_m are derived, with a large uncertainty.

An alternative approach that is much more useful is to assume equipartition between u_e and u_m, and examine the field strengths and energy density under those conditions. Since this is approximately the minimum energy condition, the limits which can be derived are of interest. Given that S_0 and θ are observed quantities, it is convenient to define f_{equi} as the "equipartition turnover frequency". For a component in equipartition, $f_{equi} \equiv f_m$. In terms of the observed quantities for 3C48 (and assuming $\delta = 1$),

$$f_{\text{equi}} = 2.0 \quad S_0^{0.34} \quad \theta^{-0.73} \quad . \tag{4}$$

From the above, it is clear that f_{equi} is a good observable, in that it depends only on small powers of the observed angular size and observed flux density. f_{equi} is the converse of the equipartition angular size discussed by Scott and Readhead (1977); in their case, they were dealing with radio sources whose angular size was poorly known, but whose overall spectrum was well measured. Table 2 lists f_{equi} for each of the four components under consideration.

To summarize the assumptions which have gone into equation (4): (a) $f_m/f_2 \approx .07/100$. The dependence on this assumption is weak; the value of f_m/f_2 used is appropriate for the integrated spectrum. (b) $u_e/u_m = 1$. Note that changing u_e/u_m by a a factor of 10 only changes f_{equi} by 10%. (c) $f_{\text{equi}} \ll f_0$. This assumption is reasonable (see Table 2); for all the components, $f_{\text{equi}} < f_0/2$. (d) $\delta = 1$. This was assumed in the lack of information to the contrary; in any case, f_{equi} does not depend strongly on δ.

It is now possible to evaluate the magnetic field strength B in each of the components. Again, from standard synchrotron theory, it is possible to derive a relationship for B in gauss. From Burbidge, Jones, and O'Dell (1974), or Marscher et al. (1979),

$$B = K(\alpha) \quad \theta^4 \quad f_m^{\ 5} \quad S_m^{\ -2} \quad \left[\frac{1+z}{\delta}\right]^{-1} \quad . \tag{5}$$

For 3C48, $\alpha = 0.8$, so that $K(\alpha) = 3.8\text{x}10^{-5}$; using $z = 0.367$, assuming

$\delta = 1$ (as above), and using equation (4) yields the following expression for B (in gauss) valid for 3C48:

$$B = 1.9\text{x}10^{-2} \ S_0^{\,0.26} \ \theta^{-0.79} \ . \qquad (6)$$

This expression for B uses the same assumptions which allowed the derivation of equation (4), the key assumption being that $u_e/u_m = 1$. As others have pointed out (see, for example, Burbidge, Jones, and O'Dell 1974), this expression for the equipartition magnetic field depends only on small powers of the observables, so that the equipartition field strength is well determined.

The total energy density in particles and fields is $u_{tot} = u_e + u_m$. The pressure in the components can then be determined from

$$P = \left[\frac{u_e}{3} + u_m \right] \ . \qquad (7)$$

The lifetimes for synchrotron losses can be compared to the overall source dimensions, to see if reacceleration of the electrons is required for the observed emission. From Burbidge, Jones, and O'Dell (1974), the limit to the radius in the absence of particle reacceleration r_L is given by

$$r_L \approx 10^5 \ B^{-3/2} \ f^{\,-1/2} \ , \qquad (8)$$

where f is the frequency of observation in GHz, B is in milligauss, and r_L is in parsecs. r_L is simply the maximum possible size of the source if the radiating electrons were to move away from the core with a velocity of c for a synchrotron lifetime. Finally, it is possible to estimate the total energies in particles and fields U_{tot}, using the redshift to the source to estimate the distance.

The results from these calculations for f_{equi}, B, u_{tot}, U_{tot}, P, and r_L for each of the components selected in 3C48 are presented in Table 2. For comparison, d_c, the approximate distance of the component from the core is also tabulated.

C. Discussion

It is clear from inspection of Table 2 that the properties of the components in the jet vary monotonically along the jet, if component 4 is assumed to lie further along the jet than component 3. There are several inferences that can be drawn from the pressure and magnetic fields.

First, the jet cannot be confined by external gas pressure from moderate temperature galactic gas alone. Boroson and Oke (1982) have shown that the optical nebulosity near 3C48 consists of stars, so that 3C48 is clearly located within a galaxy. Even assuming the extreme values for the number density of particles and the gas temperature of $n \approx 10$ and $T \approx 10^4$ still gives a gas pressure some 3 to 4 orders of magnitude less than that derived for the observed jet. The inequality is even greater if the radio emitting region is very far from equipartition.

It is possible, however, that the jet could be confined by extremely hot, dense gas. Tananbaum _et al_. (1983) report that the corrected _Einstein_ X-ray flux density of 3C48 is 3.4×10^{-7} Jy, which corresponds to an X-ray luminosity of 1.7×10^{45} ergs s^{-1}. Assuming that this gas radiates via free-free emission, and that the pressure in the gas is sufficient to confine the radio jet in 3C48, allows the gas density and temperature to be estimated. This analysis gives $n_e \sim 10^2$ and $T \sim 10^7$ °K.

The oscillating structure in the jet suggests that the binary black hole models of Begelman, Blandford, and Rees (1980) may be relevant to this source. An interesting point about such a model is that with "reasonable" values of the parameters (masses ~ 10^7 solar masses, separation ~ 0.01 pc), the model can reproduce the observed bending scale of ~ 100 pc, if enough assumptions about jet velocity and inclination angles are made. Furthermore, Begelman, Blandford, and Rees predicted that their model would cause the forbidden lines in the QSO emission spectrum to be displaced from the permitted lines in the galaxy spectrum. Boroson and Oke (1982) observed such an effect in the spectrum, with the difference amounting to 300–500 km s^{-1}.

The limits to r_L are all much greater than the projected source size, so that only mildly relativistic flow in the jet (~ 0.1 c) may be required to supply the observed components. If ϕ, the angle to the line of sight of the jet axis, is small, highly relativistic flow in the jet, or _in situ_ particle acceleration could be required. The r_L's in Table 2 become comparable to the deprojected distances in the jet when $\phi \lesssim 5^{\circ}$.

II. 3C147

The physics of the core of 3C147 was discussed extensively in chapter 3. Given that the source exhibits core-jet morphology, one question which may be asked is whether or not the jet is a free jet.

The map of 3C147 presented in chapter 2 allows the halfwidth of the jet to be determined in detail. In Figure 1 is presented a plot of the observed full width to half-maximum (FWHM) of the first 0.14 arcseconds of the jet in 3C147. The jet begins to curve strongly beyond this point, so that the half-width is not well defined further out. Also shown in Figure 1 is the estimated (deconvolved) FWHM of the underlying structure, assuming that the profile across the jet has a gaussian shape. It is clear from Figure 1 that the jet is not a free jet, since its half-width does not vary as the expected (Blandford and Rees, 1974) r^{-1}. Also on Figure 1 is plotted the peak brightness on the jet as a function of distance from the core. There is no obvious correlation of the halfwidth with the peak brightness.

III. 3C309.1

A. Observational Parameters

Kus et al. (1981) present a spectrum of 3C309.1 in which they separate the contribution of the compact core from the total spectrum. Using the observations in chapter 2 it is now possible to extend the spectrum of the core to 329 MHz. Figure 2 reproduces their spectrum, but with the 329 MHz core flux from chapter 2 included.

Using the data in Figure 2, it is possible to determine the parameters of the core spectrum in 3C309.1. With the simplifying assumption that the core may be described by a single component, $\alpha = 0.4 \pm 0.1$; $S_m = 6.4 \pm 0.5$ Jy; and $f_m = 0.35 \pm 0.05$ GHz. This spectrum is plotted as a dashed line in Figure 2. Note that this f_m is significantly below the peak frequency of 0.55 GHz suggested by Kus et al., due to the availability of the lower frequency observations.

From the map in chapter 2, the equivalent angular size of the core in 3C309.1 is $\theta \approx 17 \pm 3$ milliarcseconds. This agrees well with the estimate of Kus et al., who found $\theta \approx 15$ milliarcseconds. It is clear from the map in chapter 2 that the structure in the core could be modeled by several components very much smaller than this size, so 17 milliarcseconds is a good estimate of the maximum equivalent size of the core.

Finally, the other useful observational parameter is the X-ray flux. Zamorani et al. (1981) observed 3C309.1 with Einstein and measured a flux of 2.4×10^{-12} ergs s^{-1} in the 0.28 to 3.09 keV energy band. This corresponds to an estimated flux density of 1.0×10^{-7} Jy at 1.05 keV after correction for galactic absorption. 3C309.1 is thus a luminous X-ray source, with an X-ray luminosity of 3.3×10^{27} ergs s^{-1} Hz^{-1} at 2 keV in its rest frame.

B. Evidence for Bulk Relativistic Motion

Assuming that the core of 3C309.1 may be modeled as a spherical, homogeneous source radiating via incoherent electron-synchrotron emission, the following relationship for the expected inverse-Compton X-ray emission S_x applies (Burbidge, Jones, O'Dell, 1974; Jones, O'Dell, Stein, 1974; Marscher et al., 1979; Marscher, 1983):

$$S_x = C(\alpha)\ S_m^{4+2\alpha}\ f_m^{-(3\alpha+5)}\ \theta^{-(6+4\alpha)}\ \left[\frac{1+z}{\delta}\right]^{4+2\alpha}\ E_x^{-\alpha}\ \ln(f_2/f_m)\ ,\quad(9)$$

where E_x is the X-ray observing energy in keV and S_x is in Jy. For $\alpha = 0.4$, $C(\alpha) = 5.72\times10^{-5}$. Using the observed values for the parameters in equation (8) yields the following relationship between δ and θ, applicable to the core of 3C309.1:

$$\delta \gtrsim 230\ \theta^{-1.58}\quad . \qquad (10)$$

The inequality comes from the assumption that the observed X-ray flux is an upper limit to the inverse-Compton flux. Equation (10) is analogous to equation 2 in chapter 3, which was applicable to the core in 3C147. The above has used the redshift for 3C309.1 of $z = 0.904$

(Smith et al., 1976) and assumed than $f_2 \gtrsim 10$ GHz, so that $f_2/f_m \approx 30$. For the estimated angular size of 17 milliarcseconds, this implies that $\delta \gtrsim 2.6$, which implies that bulk relativistic motion is occurring in the core of 3C309.1, with a bulk velocity of $\beta \gtrsim 0.74c$. The actual velocity could be much higher if the angular size has been overestimated.

C. Magnetic Fields and Energy Densities

The magnetic field B may be calculated using equation (5) above. For $\alpha = 0.4$, $K(\alpha) = 2.0\text{x}10^{-5}$, so that $B \approx 4\text{x}10^{-4}$ gauss. From equation (1), with $A(\alpha) = 1.7\text{x}10^{10}$ for $\alpha = 0.4$, the ratio of the energy density in relativistic electrons to that in magnetic fields becomes $u_e/u_m \sim 130$. Thus the core may not be too far from equipartition, in view of the usual 1–2 orders of magnitude of uncertainty in u_e/u_m due to the large exponents in equation (1). The energy density in the core of 3C309.1 is then $u_{tot} \sim 10^{-6}$ ergs cm^{-3} and the pressure in the core is $P \sim 3\text{x}10^{-7}$ ergs cm^{-3}. Note that these calculations have assumed $\delta = 2.6$. Otherwise, u_e/u_m would be more than three orders of magnitude greater. Conversely, assuming equipartion would imply that $\delta \approx 5.1$ if the other parameters were unchanged. The limit to the radius r_L is $r_L \sim 60$ kpc, far larger than the core size of ~ 300 pc, so that reacceleration of the electrons is apparently not required anywhere in the core of 3C309.1.

The total energy of the core, with the above parameters, is $U_{tot} \sim 2.5\times10^{55}$ ergs, a number comparable with both the total energy in the core of 3C147 (chapter 3) or the individual knots in 3C48. If delta were unity (that is, no bulk relativistic motion), the total energy would be increased to $\sim4\times10^{57}$ ergs, and the source would be completely dominated by relativistic electrons. It appears, however, that the core of 3C309.1 is near equipartition in the relativistically moving frame of the fields and particles.

D. Discussion

Taken together, these calculations imply that 3C309.1 has bulk relativistic motion occurring within its core. There are several similarities between the core of 3C309.1 and the core of 3C147 (chapter 3), suggesting that not only may 3C309.1 be a superluminal source, but also that it may be a low frequency variable. If the latter is true, the variations in the total flux density in 3C309.1 should be easier to detect than they are for 3C147, since the core brightness in 3C309.1 is such a large fraction of the total source flux density at meter wavelengths. Using the peak on the map in chapter 2, the smallest, completely unresolved portion of the core has a flux density of about 2.7 Jy at 329 MHz (note that the calculations above included the entire core of 6.1 Jy). If the core in 3C309.1 were varying with the same fractional amplitude as the core in 3C147, the expected amplitude of variation in total flux density might be ~ 1-2 Jy, or about 5-10% of the total source flux density. For comparison, the variations observed in 3C147 amount to ~ 2% of the total flux. Such large variations in 3C309.1 would be detectable by several of the current programs to monitor low-frequency variables (see, for example, Condon et al., 1979; Fanti, et al., 1981; Fisher and Erickson, 1980; Spangler and Cotton, 1981). Unfortunately, 3C309.1 has not been included in any of these monitoring programs to date.

Finally, Kus et al. (1981) pointed out that the large bends in the structure of 3C309.1 might be due to a small angle between the line of sight and the axis of the jet. With the above value of δ, the limit on the inclination of the jet to the line of sight is $\phi \lesssim 20^\circ$. If equipartition were assumed, the required value of δ would be $\delta \gtrsim 5$, implying that $\phi \lesssim 10^\circ$. In either case, this tends to confirm the idea of Kus et al.; the core of 3C309.1 is extended nearly along the line of sight.

IV. 3C380

A. Observational Parameters

The structure in this source is dominated by two widely separated components (chapter 2). To the SE is the bright core of 3C380 (see chapter 2) and to the NW is a weaker, partially resolved component. Since a detailed radio spectrum is not yet available, the analysis of this source will similar to that for 3C48.

It is possible to model this source with a two-component model. While such a model is an over simplification, it does yield the following angular diameters and flux densities for the two brightest components in the source: $\theta_1 \approx 14$, $S_1 \approx 3.0$, $\theta_2 \approx 75$, and $S_2 \approx 1.3$, where the subscripts 1 and 2 refer to the core and to the weaker, 0.72-arcsecond distant component, respectively. The model used assumes that the core is optically thick at the observing frequency, since (see below) 329 MHz is below f_{equi} for the core.

B. Physical Conditions

It is possible to derive an equation similar to equation (4) and valid for 3C380:

$$f_{\mathrm{equi}} = 2.2 \quad S_0^{\,0.35} \quad \theta^{-0.74} \quad . \tag{11}$$

Equation (11) is not valid, however for the core of 3C380, since the equipartition frequency calculated is larger than the observing frequency, violating one of the assumptions going into equations (4) or (11). For the core, a similar formula can be derived, but the observed flux density is used as an upper limit to the maximum observable flux density, S_{peak}. From standard synchrotron formulae, $S_{\mathrm{peak}}/S_m = 0.78$ for a uniform sphere with $\alpha = 0.75$. Assuming equipartition, equation (1) then implies that for 3C380 ($z = 0.691$, $r = 2.3$ Gpc)

$$f_{\mathrm{equi}} \lesssim 4.4 \quad S_0^{\,0.41} \quad \theta^{-1} \quad . \tag{12}$$

From the above two equations, $f_{equi} \approx 0.098$ GHz for the weaker NW component, and $f_{equi} \lesssim 0.45$ GHz for the core. Both of these values have assumed that there is no relativistic motion occurring in either component.

Using appropriate versions of equations (6), (7), and (8) then allows B, P, and r_L to be estimated for the two components in 3C380. The results are $B \lesssim 1.8\text{x}10^{-3}$ G, $u_m \lesssim 1.2\text{x}10^{-7}$ ergs cm^{-3}, $P \lesssim 1.7\text{x}10^{-7}$, and $r_L \gtrsim 60$ kpc for the core, while for the NW compoent, $B \approx 4.5\text{x}10^{-3}$ G, $u_m \approx 8\text{x}10^{-7}$ ergs cm^{-3}, $P \approx 10^{-6}$, and $r_L \approx 8$ kpc. If the total energies are added up, for the core $U_{tot} \sim 3\text{x}10^{54}$ ergs, and for th NW component, $U_{tot} \sim 2\text{x}10^{57}$ ergs. The core is seen to be roughly similar to the cores in both 3C147 and 3C309.1 in terms of total energy.

V. 3C454.3

The analysis by Jones, O'Dell, and Stein (1974) of this source is still valid, since the angular size at 329 MHz reported in chapter 2 is consistent with the diameter reported by Clarke et al. (1969) at 408 MHz.

The difficulties noted by Jones, O'Dell, and Stein regarding the large energy required for relativistic expansion into an ambient medium strongly suggests that the simplest interpretation of both the asymmetric structure and the rapid variability times is that there is bulk relativistic motion occurring in the core. The asymmetry in this quasar is also seen in the larger-scale structure by Browne et al. (1982). Future low-frequency observations could put firmer limits on δ for the core (as compared to those in Jones, O'Dell and Stein) by determining what fraction of the core is actually varying, and by possibly determining a size limit to the variable component.

Burbidge, Jones and O'Dell (1974) calculate a first-order inverse-Compton X-ray flux for the compact, high-frequency (6 GHz) component in 3C454.3 that is $\sim 3\mathrm{x}10^{-3}$ Jy at 10^{18} Hz. The Einstein observations by Tananbaum et al. (1983) show that the observed X-ray flux is more than 5 orders of magnitude less, with $S_x \approx 1.2\mathrm{x}10^{-8}$ Jy at that frequency. This large discrepency implies that $\delta \gtrsim 10$ in the most compact structure of 3C454.3, thus implying that bulk relativistic motion is occurring in 3C454.3. This result is in agreement with the calculations of Jones, O'Dell, and Stein (1974), who showed that assuming 3C454.3 to be a canonical synchrotron source at the distance implied by its redshift implied highly relativistic effects were required to explain the rapid variability observed in the source. Browne et al.'s (1982) inclusion of this quasar with known superluminal quasars is clearly justified.

Conclusions

Both 3C48 and 3C147 are seen to have kiloparsec-scale jets. In the case of 3C48, the jet is not confined by external gas pressure, unless the gas is extremely hot and dense. The X-ray data for 3C48 is consistent with such gas. For 3C147, the variation of the half-width with distance from the core rules out simple free expansion of the jet and suggests that collimation is occurring. In the core of 3C309.1, bulk relativistic motion is occurring close to the line of sight, thus making 3C309.1 both a likely candidate for superluminal motion and a possible low-frequency variable. Relativistic motion is also seen to be extremely likely in 3C454.3.

This work was supported by the National Science Foundation via grant AST 79-13249 to the Owens Valley Radio Observatory.

TABLE 1

Parameters for Components in 3C48

	Component 1	Component 2	Component 3	Component 4
Region:	1	2	3	4
Measured axes				
Major axis:	60 mas	57	~ 98	–
Minor axis:	21 mas	30	~ 39	–
Pos'n angle:	-31°	-31°	-10°	–
Deconvolved Axes				
Major axis:	45 mas	42	91	~ 54
Minor axis:	11 mas	31	33	–
Peak Brightness:	2.73 Jy/bm	2.70	2.13	0.71
Flux density:	1.7 Jy	2.2	4.1	~ 1.4
θ_g:	22 mas	24	55	54
Angular size θ:	40 mas	56	99	97
Physical size:	0.2 (kpc)	0.3	0.5	0.5

TABLE 2

Derived Physical Parameters for Components in 3C48

	Component 1	Component 2	Component 3	Component 4
Region:	1	2	3	4
θ (mas)	40	56	99	97
f_{equi} (MHz)	167	144	118	82
B (mG)	1.1	0.9	0.7	0.5
u_{tot} (erg cm^{-3})	10^{-7}	$7x10^{-8}$	$4x10^{-8}$	$2x10^{-8}$
U_{tot} (10^{55} ergs)	1.3	2.6	7.9	4.3
P (erg cm^{-3})	$7x10^{-8}$	$5x10^{-8}$	$3x10^{-8}$	$1.5x10^{-8}$
r_L (kpc)	18	24	37	55
d_c (kpc)	0.3	1.2	1.7	2.5

References

Begelman, M.C., Blandford, R.D., and Rees, M.J. 1980, Nature, 287, 307.

Blandford, R.D., and Rees, M.H. 1974, M.N.R.A.S, 169, 443.

Boroson, T.A., and Oke, J.B. 1982, Nature, 296, 397.

Browne, I.W.A., Clark, R.R., Moore, P.K., Muxlow, T.W.B., Wilkinson, P.N., Cohen, M.H., and Porcas, R.W. 1982, Nature (in press).

Burbidge, G.R., Jones, T.W., and O'Dell, S.L. 1974, Ap.J. 193, 43.

Clarke, R.W., Broten, N.W., Legg, T.H., Locke, J.L., Galt, J.A., Yen, J.L., and Chisholm, R.M. 1969, M.N.R.A.S., 146, 313.

Condon, J.J., Ledden, J.E., O'Dell, S.L., and Dennison, B. 1979, A.J., 84, 1.

Fanti, C., Fanti, R., Ficarra, A., Mantovani, F., Padrielli, L., and Weiler, K.W. 1981, A.A. Suppl., 45, 61.

Fisher, J.R., and Erickson, W.C. 1980, Ap.J., 242, 884.

Gould, R.J. 1979, A. and A., 76, 306.

Jones, T.W., O'Dell, S.L., and Stein, W.A. 1974, Ap.J., 192, 261.

Kellermann, K.I., and Pauliny-Toth, I.I.K. 1971, Ap. Lett., 8, 153.

Kus, A.J., Wilkinson, P.N., and Booth, R.S. 1981, M.N.R.A.S., 194, 527.

Marscher, A.P., Marshall, F.E., Mushotsky, R.F., Dent, W.A., Balonek, T.J., and Hartman, M.F. 1979, Ap.J., 233, 498.

Marscher, A.P., Ap.J. 1983, 264 (in press).

Readhead, A.C.S., Cohen, M.H.C., Pearson, T.J., and Wilkinson, P.N.W. 1978, Nature, <u>276</u>, 768.

Scott, M.A. and Readhead, A.C.S. 1977, M.N.R.A.S., <u>180</u>, 539.

Simon, R.S., Readhead, A.C.S., Moffet, A.T., Wilkinson, P.N., and Anderson, B. 1980, Ap.J., <u>236</u>, 707.

Smith, H.E., Spinrad, H., and Smith, Eileen O. 1976, P.A.S.P., <u>88</u>, 621.

Spangler, Steven R., and Cotton, William D. 1981, A.J., <u>86</u>, 730.

Tananbaum, H., Wardle, J.F.C, Zamorani, G., and Avni, Y. 1983, Ap.J., <u>268</u> (in press).

Veron, M.P., Veron, P., and Witzel, A. 1974, A. and A. Suppl., <u>13</u>, 1.

Zamorani, G. <u>et al.</u> 1981, Ap.J., <u>245</u>, 357.

Figure Captions

Figure 1: Two measurements of the FWHM of the jet in 3C147 are presented, along with measurements of the peak brightness along the jet. The dashed curve is from measurements of the FWHM of the jet, directly from the map of this source in chapter 2. The dotted curve is the de-convolved FWHM, assuming a gaussian shaped profile for the underlying jet. The error bars on this curve include the effects that deconvolution introduced into the original measuring errors. The solid line is the peak brightness along the jet as a function of distance from the core.

Figure 2: The spectrum of 3C309.1, reproduced from Kus *et al.* (1981). The solid dots represent measurements of the total flux; the open circles are observations of the core flux from various sources (see Kus *et al.* and references therein). The flux density of the extended structure is plotted as x's. The single point on the core spectrum from chapter 2 is plotted as an open square. Kus *et al.* included curves of the estimated spectra for both the core and the extended structure, shown as solid lines. My estimated core spectrum appears as a dotted line.

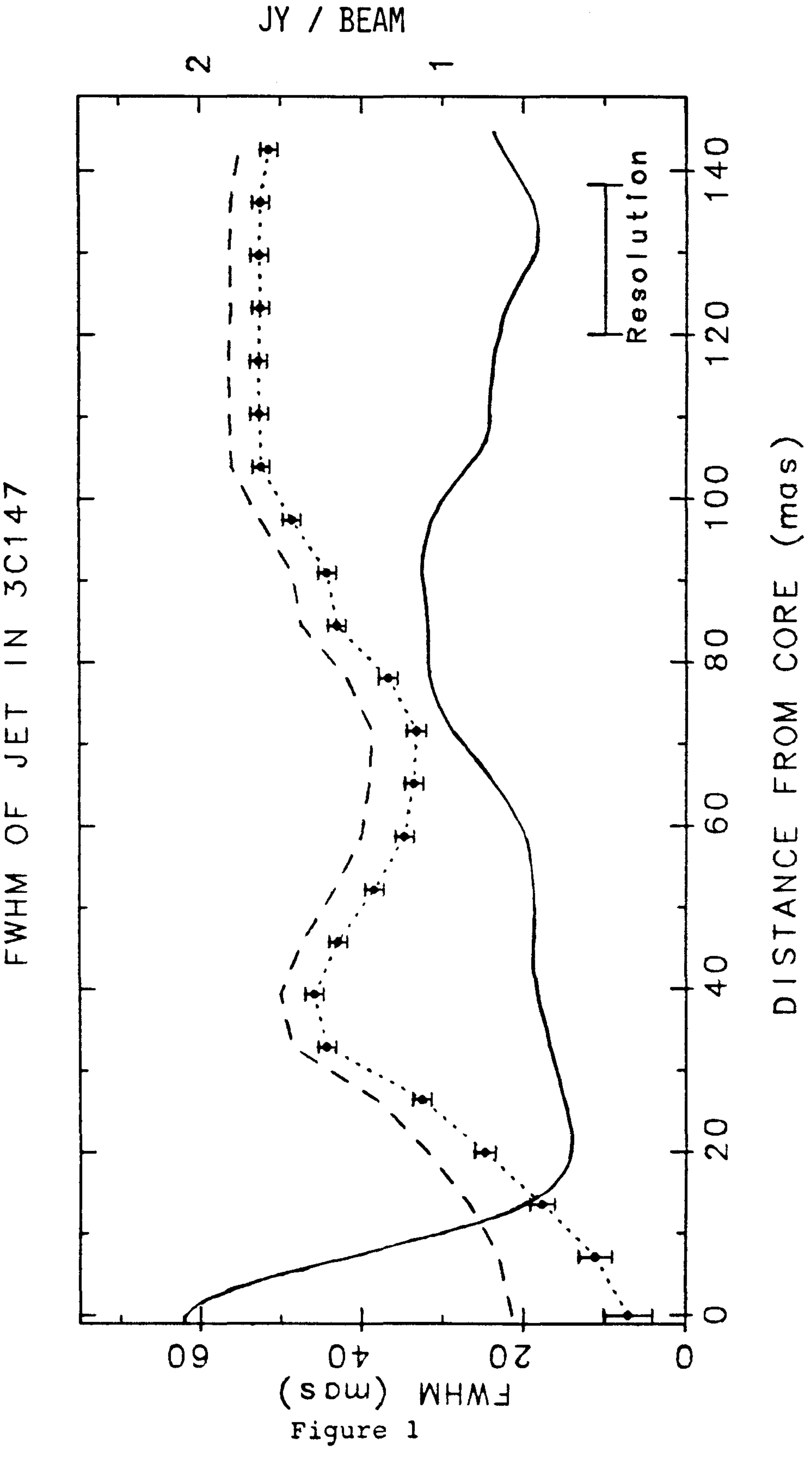
FWHM OF JET IN 3C147
JY / BEAM
2
1
Resolution
DISTANCE FROM CORE (mas)
0
20
40
60
80
100
120
140
FWHM (mas)
0
20
40
60

Figure 1

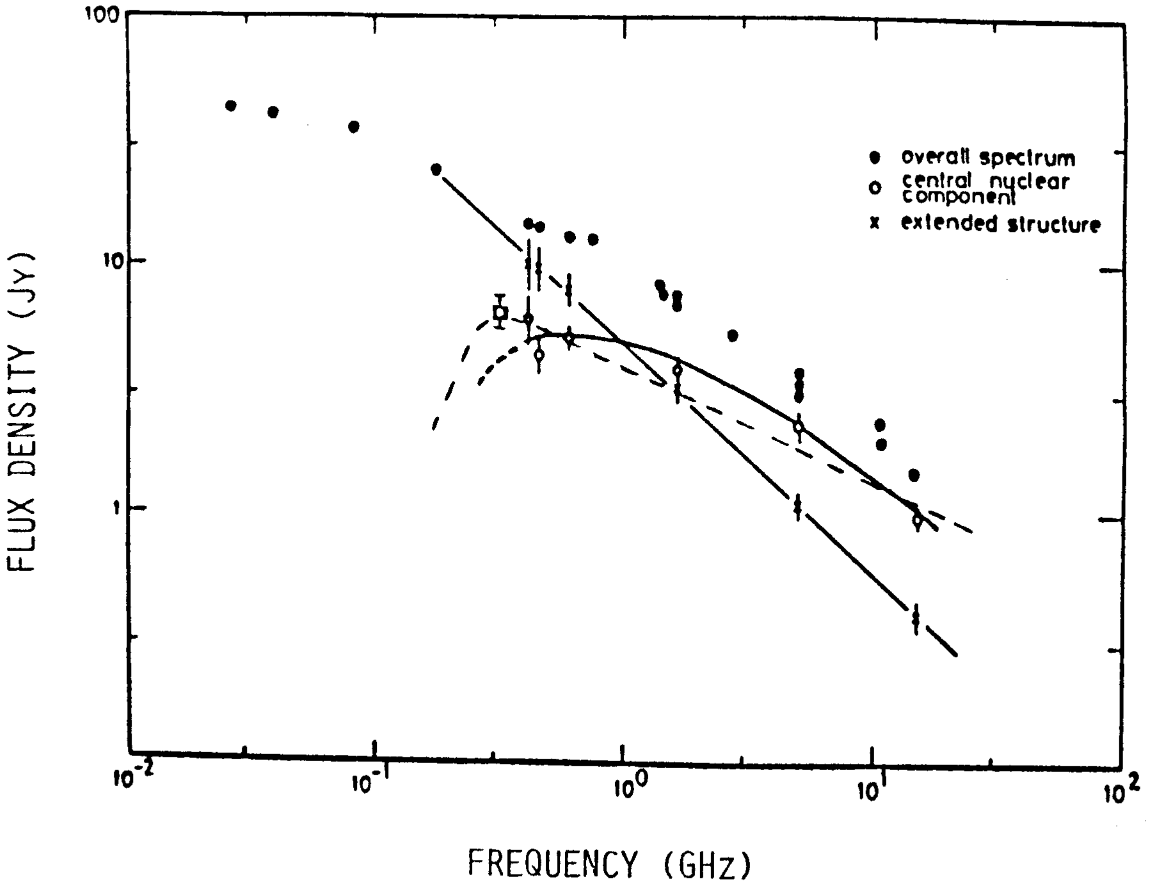
FLUX DENSITY (JY)
100
10
1
FREQUENCY (GHz)
10^{-2}
10^{-1}
10^{0}
10^{1}
10^{2}
● overall spectrum
○ central nuclear component
x extended structure

Figure 2

APPENDICES

A. The Modelfitting Program and

How to Use It

B. Calibration of Weak Fringes

Appendix A

The Modelfitting Program and How to Use It

Introduction

The program MODELFIT fits a model to Merge-format (Caltech-format) VLBI data. The purpose of this appendix is to help users of this program take full advantage of the features of the program, without going into great detail on the inner workings of the program.

The program operates by trying to minimze the agreement factor AF, which measures the goodness-of-fit of the model to the data. The agreement factor is defined as

$$AF = \left[\sum_i \left[\frac{(m_i - o_i^2)}{e_i^2} \right] / N \right]^{1/2} , \qquad (1)$$

where the sum is done over the amplitudes and closure phases. The m_i are the predictions of the model; o_i are the observations; e_i are the 1σ error limits; and N is the total number of independent data points. Note that the closure phase measurements are not all independent, so each closure phase is downweighted by a factor equal to the ratio of the number of closure phases available at a given UT over the number of those closure phases which are independent. In addition, N is adjusted so that it is equal to the number of independent data points, rather than simply the sum of the number of amplitudes plus the number of closure phases. With that definition, the agreement factor is the reduced Chi-square measurement of the fit to the data.

To improve the fit, the program searches for the minimum AF that it can find by varying some or all of the parameters of the model, as selected by the user. The actual FORTRAN code for this search for the minmum is based on routines devised by Bevington (1969), with some improvements to prevent divergence. The user of the program has a choice of two search strategies:

1. Gradient Search: For each of the variable parameters selected, the program numerically calculates the derivative of the agreement factor with respect to variations in that parameter. These derivatives are then used to determine the gradient in the agreement factor with respect to all of the variable parameters. All of the parameters are the changed at the same time, to move down the gradient. The step size for each parameter is adjusted so that for each individual variable parameter a single step has the same effect on the overall AF.

2. Brute Force: The program steps through the parameters one by one, finding the minimum of the AF with respect to each variable parameter in turn before going to the next. Only one parameter is varied at a time.

A question which arises is which search method to use at what time. The gradient search is fairly good in moving towards a minimum if the model is not yet close. By its nature, however, once it is close to the minimum in the AF the speed of convergence will drop. The brute-force search, however, is fair if a model has some resemblance to the final model. The brute-force search will almost always improve the results from an initial gradient search.

The gradient search is especially useful when a small number of inter-dependent parameters are being adjusted. For example, the radius and position angle of a component both describe its location. Therefore, using a gradient search and varying those two parameters together is equivalent to varying the location of a component. The gradient search is less useful when a large number of component parameters are being varied, as the step sizes are very small, and many local minima can be found. As a result, the gradient search will only rarely improve the fit significantly if many parameters are being varied simultaneously. On the other hand, it makes no difference with the brute-force search if all of the parameters are varied at one time. If a model is close to some sort of overall minimum in the AF, and is well constrained (see below), varying all of the parameters at once with the brute-force search selected is useful as a final tweaking up of the model.

There is a useful analogy to the fitting procedure, and that is to think of the AF as the altitude measurement in some mountainous terrain, so that the search for the minimum in the AF is the analogue of moving downhill as far as possible. If only two model parameters are being varied, the analogy is exact; if more than two are being varied, you will have to think in more dimensions! If your model has little to do with the brightness distribution in the source, you may spend considerable time wandering around in the high plains with little overall improvement in the model. On the other hand, if you have a model which is reasonable, this program will always make it better, until it has reached a local minimum in the agreement factor.

A. Component Parameters

Each component in the model is described by six parameters in the program. These are the flux of the component F, the distance from the origin r, the position angle of the displacement from the origin θ, the angular size a, the axial ratio of the component e (defined as the minor axis over the major axis, so that $e \leq 1$), and the position angle of the long axis of the component ϕ. In addition, each component has a specified model type. While the most popular type is gaussian (that is, the profile of the component has a gaussian shape, with the angular size refering to the FWHM of the component), it is also possible to specify components consisting of a uniform disk, a tapered disk (which is _exactly_ equivalent to an optically thin sphere), a ring, and a line. For these non-gaussian components, the angular size refers to either the diameter or, in the case of the line, the length.

The selection of model type can significantly influence the results. In most situations, where an approximate model is desired, guassian-shaped components are as good as any. However, if the user is trying to measure the angular diameter of a component to use in a theoretical calculation, he is well advised to use a model component of the appropriate type. For example, calculations of inverse-Compton X-ray emission often assume that the component under consideration is a sphere (see chapter 3, and references therein), so that the tapered disk (TYPE=3) should be used. If the sphere is optically thick, the uniform disk should probably be used. The situation in which model type can make a big difference is when trying to fit large-scale structure (that is, structure in the map which is still partially resolved, even on the shortest baselines). A gaussian-shaped component has no limiting angular size, and as a result can spread itself over a large area, with a large flux density to match. It is possible, as a result, to greatly over-estimate the flux and angular FWHM of the extended component. The tapered disks do not suffer from those problems, and as a result will tend to have less flux in smaller areas than gaussian-shaped components fit to the same data.

B. Failures of the Program

There are certain situations in which the program will give poor results. This occurs primarily for two reasons. First, a poor starting model was chosen, so that making a bad model better still gives a bad model. Second, some of the parameters for some of the components are unconstrained, producing exaggerated model characteristics.

The first situation can be remedied by guessing at a better starting model, or going to mapping. It is not usually a good idea to simply begin model fitting with a random model (for example, a very close double) and wait for it to get better; it is much more efficient to guess the separation distance and position angle based on the occurrences of the maxima and minima in the UV-plane, and then let MODELFIT loose on the data. Even if the source is barely resolved, it is usually possible to get a position angle before starting MODELFIT.

The second failure occurs because some of the model parameters are unconstrained. The most common example is probably the tendency of the program to produce components with axial ratios $<< 0.1$. This is an indication that there is a barely resolved component, with a shape that is not constrained by the data. It is often possible to replace these components with small circular components, and vary the size alone. Another example of this situation is the tendency of the program to effectively remove components from the model. Users should watch for, and perhaps remove, components with tiny fluxes and extremely large angular sizes. Such components may have almost no effect on the visibilities from the model, or the agreement factor.

C. Methods of Use

There are three basic ways of using the program, only one of which seems to be common knowledge.

1. Basic Modelfitting

In this mode of operation, the program is used to fit a model to the data set. This is the most common method of using the program, and has as its goal finding one or more components which represent the structure of the source.

2. Improving a Map

There is a mode of the program which can be used to improve a source map. It is especially useful when the source being mapped has extended structure which is only just detected on the shortest few baselines. To use this feature of the program, the user answers 'yes' when the program asks if there will be an underlying constant model. This implies that the program, after being told the appropriate file names, will calculate the model visibilities from the underlying map first. Then, when calculating the agreement factor of the overall model, the program will add the model visibilities of the underlying map to the visibilities of the variable components to find the overall model visibilities. The procedure is exactly equivalent to subtracting a map from the data set, and then fitting to the residuals. It is a reliable method for locating extended structure, but convergence may be slow, and care must be taken that pathological, unconstrained components are not introduced. The maps of both 3C147 and 3C380 in this thesis were significantly improved with this method (see chapter 2).

This technique can also be used to speed convergence of a map towards the final map as mapping iterations are proceeding. The basic technique is to fit extra components and the CLEAN output map to the data set before starting the next iteration through the mapping procedure. Trial and error effort suggests that it is not a good idea to modify the clean map before trying to find the extra components; rather, simply use the clean map as the underlying model, and fit one or two components on top of it to the data. If the data set is well calibrated, the flow diagram in Figure A1 is a useful guide to this technique. It tends to produce a map which fits the original calibrated data set as closely as possible, but which also represents the most extended structure. There is probably no point in using MODELFIT in this way until efforts at finding an ordinary CLEAN map have reached an unsatisfactory conclusion. If the main problem with the map is missing structure on the shortest baselines, only one fitting step might be needed; in the case of 3C48 (see chapter 2), several iterations through Figure A1 were required.

3. Modeling a Map Component:

A final capability of the program is to model components in a complicated source. Using the final clean map of a source, the user subtracts all the delta functions from the region of interest, then uses the leftover map as the input for the underlying model in MODELFIT. It is then possible, for example, to find the parameters which describe the core on a complicated map, and yet still have a model which fits the data as well as, or better than, the final clean map. The parameters of such repacement components are usually tightly constrained; the main difficulty is defining the area in which the delta functions of the map are to be deleted.

C. Estimating Errors

It is possible to estimate the errors in the fit components. From Bevington, a 1σ change in the AF corresponds to a change in the AF of $1\sigma \approx \mathrm{AF}\ N^{-1/2}$. The factor AF on the right side comes from assuming that, for a perfect model, the difference between the AF and 1 is caused by incorrect estimation of the errors. This is usually the situation with VLBI data, since it is convenient to neglect the systematic errors from calibration in the final errors on the data. This is a statistically correct estimation of a 1σ change, but is difficult to apply in practice: for each component parameter for which an error estimate is needed, it is necessary to first find the best model possible, then find how far in each direction the parameter of interest must be changed to produce a 1σ error, when the other variable parameters of the model are allowed to change. Alternatively, bounds on the 1σ error limits can be found by finding the magnitude of change in the parameter of interest which causes a 1σ change in the AF while the other parameters are held constant.

D. Tricks

There are some tricks which can be used to improve the output model, or speed the program on its way. They are recommended to experienced (or frustrated) users.

1. Averaging the data. Unless the user is trying to produce an exact fit, averaging the data by a factor of two or three will speed the program up by almost exactly the same factor.

2. Alternating component types. Once a model seems to have reached a local minimum, you are stuck, unless you can "kick" it on its way. One method for doing this is to change the component types from gaussian to tapered disk, fit once varying only flux and axis, fit again varying all the parameters, then change the component back to the original type and do another 2-step fit (axis and flux, then all parameters). This will often significantly improve the model, and is a way of getting out of local minima on your way to a global minimum.

Reference

Bevington, P.R., "Data Reduction and Error Analysis for the Physical Sciences", McGraw-Hill, Inc., New York, 1969.

Caption for Figure A1

Flow diagram guiding the use of MODELFIT as an aid in mapping.

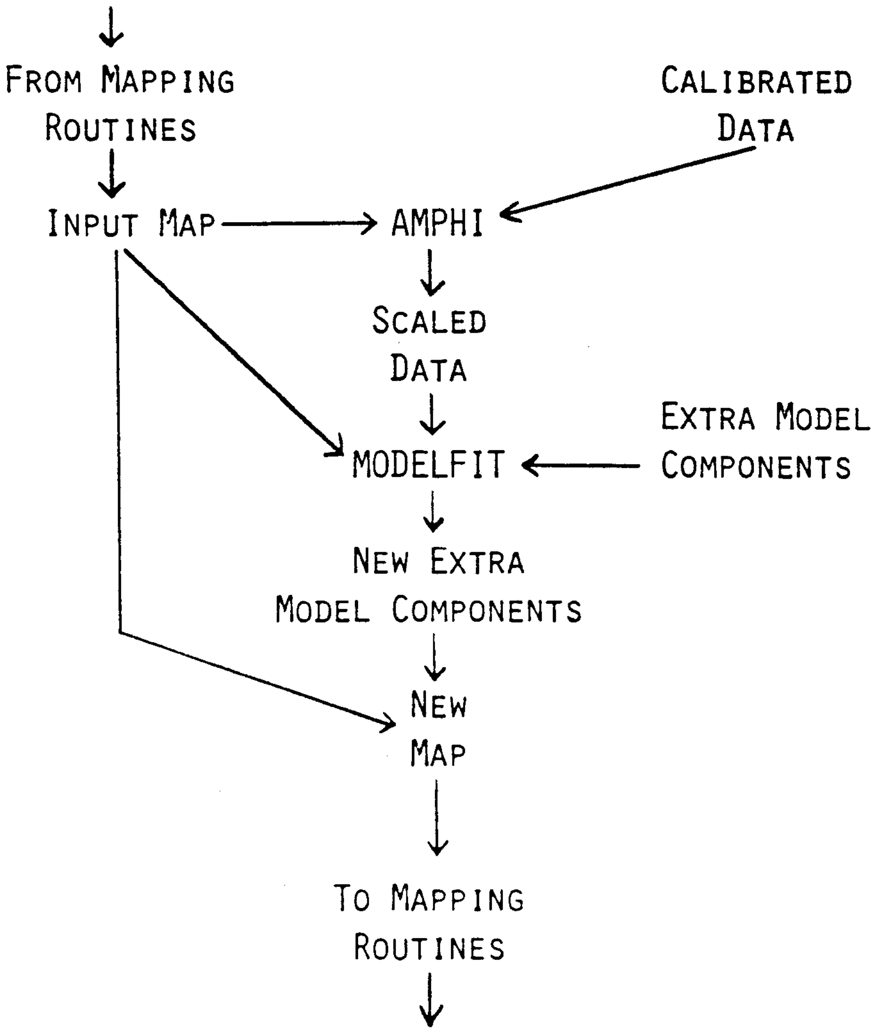
FROM MAPPING ROUTINES
CALIBRATED DATA
INPUT MAP
AMPHI
SCALED DATA
EXTRA MODEL COMPONENTS
MODELFIT
NEW EXTRA MODEL COMPONENTS
NEW MAP
TO MAPPING ROUTINES

Figure A1

Appendix B

Calibration of Weak Fringes

Linfield (1981) discusses a method for correcting for the bias in the visibility amplitudes introduced by noise (Moran, 1976; Purcell, 1973). A difficulty with the procedure he describes for eliminating the bias in very weak data is that it requires an estimate of the fraction of data which failed to converge due to a limit on the signal-to-noise ratio (SNR). I have changed my original empirical method of correcting the data (described by Linfield) so that this estimate is no longer required, and incorporated the new method into the program UNBIAS.

In UNBIAS, an estimate of the average SNR for a given time interval is determined from the data, and then a polynomial P(SNR) is calculated to find the multiplicative correction factor. The effect on data is shown in Figures B1 and B2. In Figure B1, the relative fringe amplitude is plotted as a function of SNR (the SNR was varied by varying the coherent integration time). The curve through the data points in Figure B1 is the empirical correction curve applied to the data to produce Figure B2. Note that the correction is applied only to the amplitudes, and not to the errors, so that the lowest SNR data have their SNR reduced even further.

References

Linfield, R.P. 1981, Ap.J., 244, 436.

Moran, J.M. 1976, Methods of experimental Physics, 12, Part C, ed. M.L. Meeks (New York:Academic Press), 174-197.

Purcell, G.H. 1973, Ph.D. thesis, California Institute of Technology.

Figure Captions

Figure B1: The relative amplitude as a function of SNR. The curve through the data is the empirically derived correction function.

Figure B2: Amplitude data as a function of SNR after correction by UNBIAS.

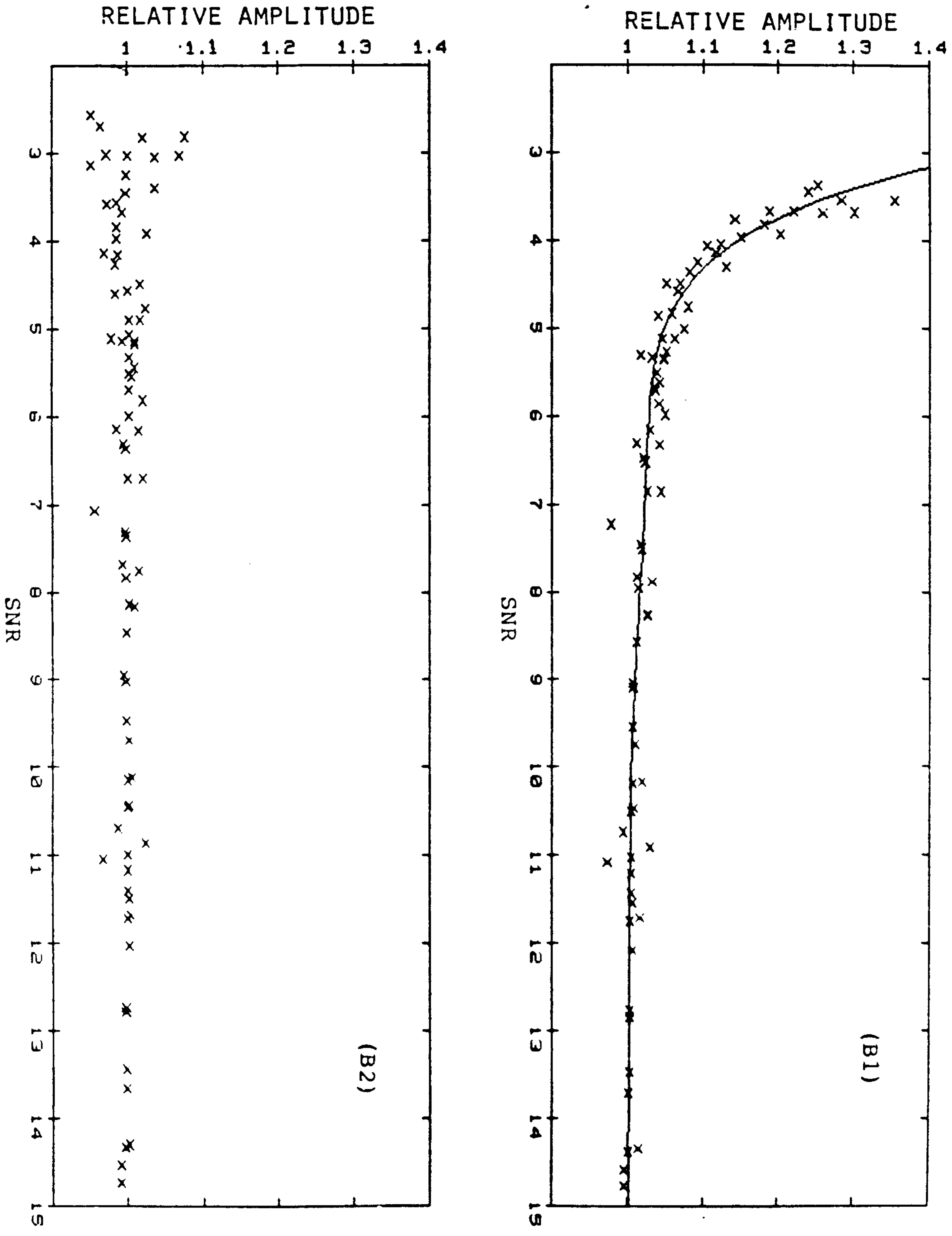

Figures B1 and B2